2008

Thin film metal-insulator-metal tunnel junctions for millimeter wave detection

Subramanian Krishnan
University of South Florida

Thin Film Metal-Insulator-Metal Tunnel Junctions For Millimeter Wave Detection

by

Subramanian Krishnan

A dissertation submitted in partial fulfillment
of the requirements for the degree of
Doctor of Philosophy
Department of Electrical Engineering
College of Engineering
University of South Florida

Co-Major Professor: Elias K. Stefanakos, Ph.D.
Co-Major Professor: Shekhar Bhansali, Ph.D.
Yogi D. Goswami, Ph. D.
Kenneth A. Buckle, Ph. D.
Dennis K. Killinger, Ph. D.

Date of Approval:
October 29, 2008

Keywords: mim diode, rectenna, ni-nio-cr, thin film insulator,
millimeter wave detection

DEDICATION

To my parents, brother and my wife for their unconditional love and support.

ACKNOWLEDGEMENT

I would like to thank my major professors, Dr. Lee Stefanakos and Dr. Shekhar Bhansali for providing me the opportunity to work on my Masters and continue on for a Doctorate degree. Their ideas and feedback have kept me focused in my research. Dr. Shekhar Bhansali deserves special thanks for all the motivation and support he has provided. I have learnt a lot from him both professionally and personally. I would also like to thank Dr. Yogi Goswami for introducing me to the concept of alternate energy conversion, which has been the backbone for this research. I would like to thank Dr. Ken Buckle and Dr. Dennis Killinger for serving as my committee members. Thanks to Dr. Srinivas Katkoori for chairing the dissertation defense. I would also like to acknowledge Dr. Weller and Dr. Dunleavy for providing the W-band test set-up in the Noise lab.

Most of the fabrication process and all materials characterization and testing were carried out at the Nanomaterials and Nanomanufacturing Research Center. Thanks to Rob Tufts for maintaining such an excellent facility with his efficient team of engineers (Rich, Jay and Yusuf) and staffs. I am also grateful to Jay Bieber and Dr. Yusuf Emirov for training me in the facility equipments. I would like to thank Dr. Bert Lägel for showing me the nuances of e-beam lithography. I would also like to thank the department and CERC staffs (Becky, Norma, Gayla, Irene, Ginnie and Barbara) for helping with all the academic and administrative tasks.

I would like to acknowledge and thank Dr. Senthil Sambandam for introducing me to thin film depositions. I would also like to thank Kevin, Shyam and SP for teaching so much about thin film deposition, lithography and many other lab related equipments. Thanks to Carl and Johnny for keeping the Bio-MEMS lab organized and running. I would like to express my regard to Dr. Niranjan Ramgir for constantly encouraging me. I cannot forget his sense of humor and audacity. A special thanks to Praveen for helping me in different walks of my research at USF. I am extremely thankful to Henrry for taking his time out during the weekends to assist me with the RF measurements. I would like to thank Jeffy Jiminez for teaching me the polymer coating technique. A big thank you to Rudran, Joe Register, and Joe Johns for helping me with the diode measurement and characterization. I can never forget our brainstorming sessions about developing "radical" experiments. I thoroughly enjoyed mentoring as well as learning several things from them. Thank you Srinath for helping me unwind with our racquetball nights. I would also like to thank all other present and past members of ENB 152.

Special mention goes to my friends in Tampa - Kaushik, Mahesh, Francis, Tony, Vidya and Sandesh. We have bonded so much over the years that I cannot imagine my life in Tampa without them. I am grateful to my friends Shiva, Vasu, Ranjani, Priya, Hari, Vathsan, Srini, Suji and Rajesh for their support.

Words are not enough to express my appreciation and affection for my beloved wife Lavanya for standing by me patiently and motivating me throughout my research and my gratitude to my mother, father and brother. I am indebted to my family for their love, support and sacrifice. If not for them, I would not be for what I am today.

TABLE OF CONTENTS

LIST OF TABLES

LIST OF FIGURES

THIN FILM METAL INSULATOR METAL TUNNEL JUNCTIONS FOR MILLIMETER WAVE DETECTION

Subramanian Krishnan

ABSTRACT

Millimeter wave imaging systems are the next generation imaging systems being developed for security and surveillance purposes. In this work, thin film metal-insulator-metal (MIM) tunnel junction based detector using Ni-NiO-Cr has been developed for the first time for millimeter wave detection operating at 94 GHz. Extensive process development has been carried out to fabricate the MIM junctions. Arrays of MIM junctions with 1 μm^2 contact area and ultra-thin insulator layer of ~3 nm have been developed using e-beam lithography and reactive sputtering, respectively. MIM diodes were also fabricated in a bulk-micromachined diaphragm configuration to minimize surface wave loss.

DC and millimeter wave measurements were carried out on the fabricated diodes to determine the device characteristics and performance. The current-voltage (I-V) measurements yielded current in the range of few μA with significant non-linearity and asymmetry. A maximum sensitivity of 7 V^{-1} was also obtained from the fabricated diode.

These tunnel junctions showed a positive response to millimeter wave signal, with output current in the range of few μA. By controlling the input power of the millimeter wave signal, the output current from the device could be varied.

Additionally, MIM diodes with 100 μm^2 contact area were developed using optical lithography technique. The I-V characteristics of diode demonstrated a uniform behavior, with a sensitivity value of $15V^{-1}$. Furthermore, the diodes were utilized to observe the effects of post-deposition annealing on the diode I-V behavior. The I-V measurement provided evidence of diode operation up to 350°C, with optimal operation at 250°C.

Finally, the feasibility of using an organic insulator was also investigated. MIM junctions were fabricated with a thin layer of polyaniline using Langmuir-Blodgett deposition process. The electrical characteristics of the polyaniline based MIM junction was determined by evaluating its I-V response. The use of an alternate dielectric proved successful, yielding a significant non-linearity and asymmetry. However, the output current obtained from these junctions was in the order of nA. By optimizing the deposition process, the organic MIM junctions can be developed to yield better device characteristics.

CHAPTER 1

INTRODUCTION

1.1 Thin Film Metal-Insulator-Metal Junctions for Millimeter Wave Detection

Metal-Insulator-Metal (MIM) junctions are tunnel diodes, which operate on the basis of quantum tunneling phenomenon i.e., when a sufficiently thin barrier is sandwiched between two electrodes, current can flow between them by means of tunneling. MIM junctions consist of two metal electrodes separated by a very thin barrier and electrons can tunnel through the barrier when a bias is applied. On account of this behavior, MIM diodes were recommended for harmonic mixing and detection when integrated with an antenna [1],[2]. The integrated antenna concept was later extended to other applications such as millimeter (mm) wave and infrared (IR) detection [3] due to faster response of these diodes [4]. MIM diodes when coupled with an antenna can absorb the electromagnetic energy from the object emitting the mm-wave radiation and convert it to electrical energy. This rectified signal can then be transmitted to an electronic circuit to identify the detected object under observation.

Several mm-wave windows exist in the atmosphere; however the wavelength of interest for the development of mm-wave detector is ~3 mm (94 GHz). At this wavelength, the size of the diode is much smaller and is expected to have a faster response. In addition to its faster response, MIM based mm-wave detectors provide

asymmetric electrical characteristics, device scalability, and wavelength tunability when coupled with an antenna. Figure 1.1 illustrates the concept of mm-wave detection using an array of antenna-coupled MIM diodes.

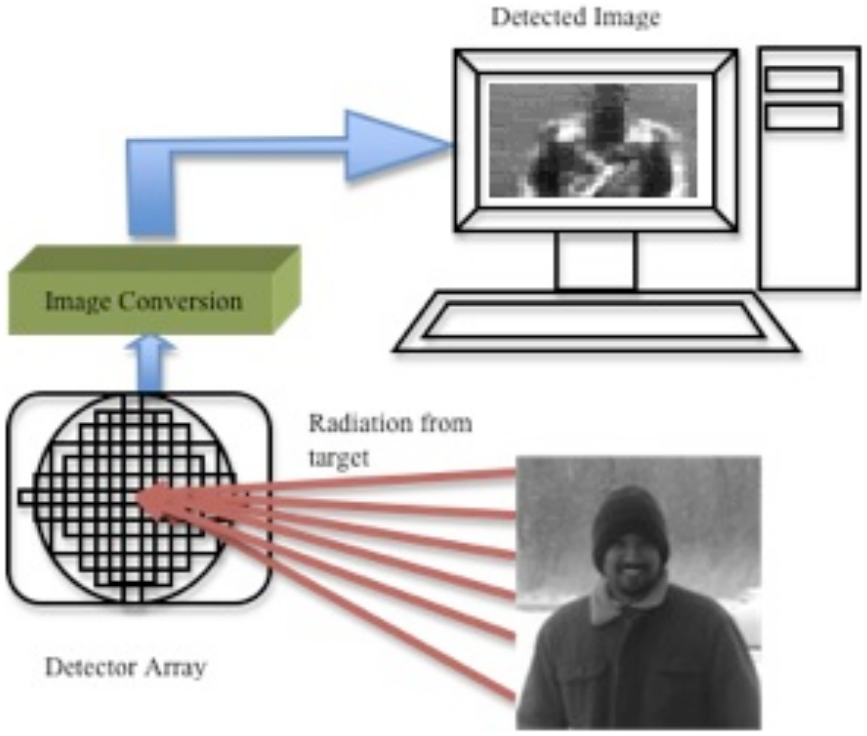

Figure 1.1: Schematic Illustration of the Concept of mm-wave Detection Using an Array of Antenna-Coupled MIM Diodes. Adapted From [5]

1.2 Overview of Millimeter Waves

Millimeter wave refers to the region of the electromagnetic spectrum between microwaves and the far infrared. Millimeter waves generally encompass frequencies between 30 and 300 GHz. At these frequencies, the mm-wave radiation is well suited for radar and telemetry applications due to its shorter wavelength than microwaves [6].

Figure 1.2 shows the electromagnetic spectrum illustrating the mm-wave regime between microwaves and IR.

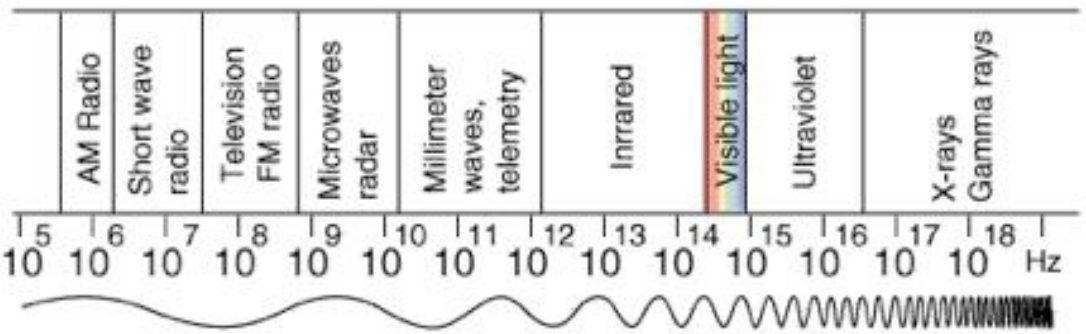

Figure 1.2: Electromagnetic Spectrum Illustrating the Millimeter Wave Regime. From [7]

Millimeter wave radiation is a form of radiated electromagnetic energy obeying the same laws as those for visible light, radio waves and X-rays [8]. All objects above 0K are expected to emit mm-wave radiation and the amount of radiation emitted by a body at a particular wavelength is given by Planck's energy distribution [8]. The boundary between different radiations such as visible, infrared and millimeter waves are not absolute and are segregated primarily based on the source and detectors that are available and used.

Millimeter wave imaging and detection make use of the atmospheric window occurring between 10 mm and 1 mm. In this window the radiation is not reflected or absorbed by the atmosphere and the atmospheric transmission is the highest. The

electromagnetic radiation windows occur, centered at 35, 94, 140, and 220 GHz and the bandwidths available at each of these windows are extremely large, and are approximately equal to 16, 23, 26, and 70 GHz, respectively [9]. These large bandwidths and shorter wavelengths allow for high information rate capability, high resolution for precision tracking, target identification in radars, and high sensitivity radiometers than the microwave radars. Figure 1.3 illustrates the main windows occurring in the millimeter wave range [9].

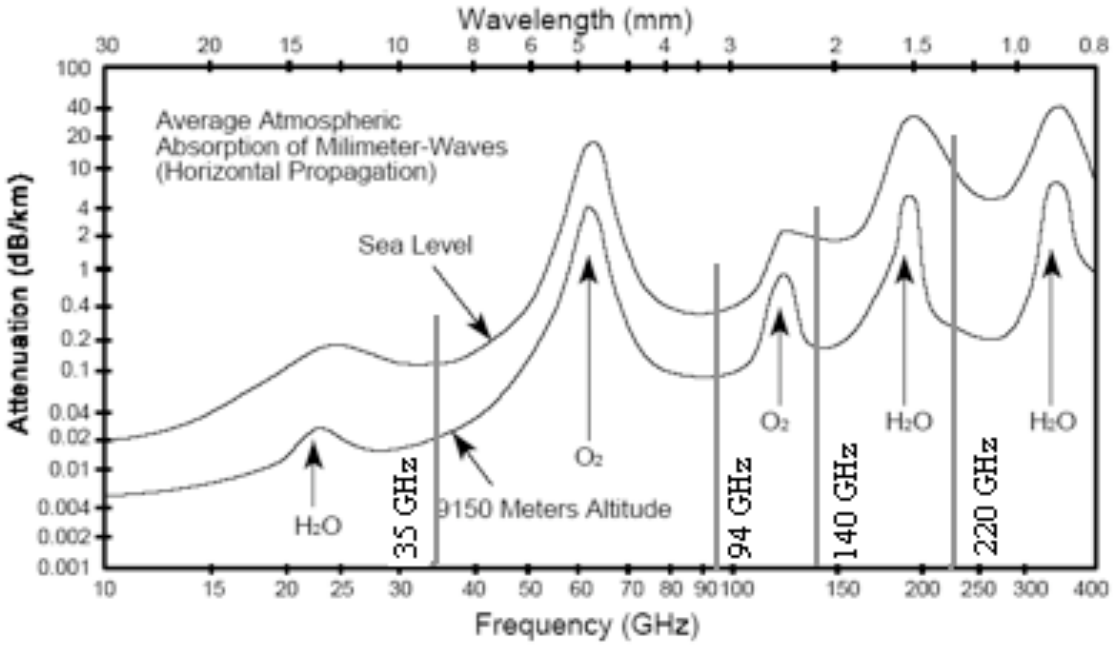

Figure 1.3: Millimeter Wave Atmospheric Absorption for Horizontal Propagation. From [9]

The main characteristic of millimeter wave that makes it suitable for a wide range of application is its ability to penetrate through objects. This noteworthy behavior of the millimeter wave can be used for object detection and imaging using a millimeter wave

detector. Additionally, at millimeter wavelengths the atmospheric attenuation due to environmental conditions such as aerosol, dust, smoke, and other contaminants are lesser, making millimeter wave systems ideal for many applications [9]. The short wavelength characteristic of millimeter waves in combination with its interaction with atmospheric constituents and wide operating bandwidths provide many advantages in developing a mm-wave detection system. A detailed overview on different techniques used for mm-wave detection is presented in the next chapter.

1.3 Goals and Objectives:

The primary objective of this research work is to develop thin film MIM tunnel junctions with two different electrodes for mm-wave detection. The following goals were identified as being pertinent to achieving the objective.

(a) To determine a suitable material combination for MIM diodes – Materials have to be selected based on its work function. To achieve asymmetrical and non-linear electrical characteristics, work function difference between two metals should be large.

(b) To determine the contact area and processing techniques for fabricating the tunnel junctions – In order to develop MIM diodes for utilization as mm-wave detectors with faster response, the size of the detector needs to be small. Also, the fabrication technique should be able to accommodate such a small size.

(c) To develop a methodology for depositing thin layers of insulators- For the electrons to tunnel, very thin insulator layer needs to be developed with uniformity and minimal roughness.

(d) To determine the effects of dielectric thickness and temperature on the electrical behavior of the diode – The electrical characteristics of the diodes depend on various factors. Understanding the diode behavior with respect to those factors will provide more information to develop a robust diode structure.

(e) To estimate the performance of the diodes at mm-wave frequency – The diode characteristics have to be verified for mm-wave detection by investigating the AC to DC energy conversion.

To accomplish the aforementioned goals, MIM tunnel junctions with Ni-NiO-Cr were fabricated with 100 μm^2 and 1 μm^2 contact area. Optical and e-beam lithography techniques were used to fabricate the devices. The electrical characteristics of the diodes were evaluated by subjecting the diodes to dc and mm-wave (94GHz) signal. Also, the effect of dielectric thickness on the diode characteristics was determined by varying deposition parameters. The temperature dependency of the diodes was determined by performing post-deposition annealing. Additionally, to determine the feasibility of using an organic insulator layer in MIM junctions, polyaniline monolayer was deposited as an alternate insulator and its effect on diodes behavior was studied.

1.4 Thesis Organization

A brief overview of mm-wave detection systems followed by theoretical background of MIM diodes, processing techniques and characterization of diodes for mm-wave detection is presented in detail.

In chapter 2 a detailed background study on millimeter wave detection, the types

of devices used for detecting mm radiation and the current state of the art is presented. In addition, the need for a better detection system and how antenna-coupled MIM diodes can be deployed for mm-wave detection is addressed.

In Chapter 3, the theory of MIM diode and its operation is presented. The various methods used in fabricating MIM diodes are discussed in Chapter 4, including an alternate MIM diode. Chapter 5 elaborately discusses the actual diode design and fabrication used in this research. The dielectric deposition technique is also described in this chapter. It also reports the fabrication issues faced during the various stages of diode development.

Chapter 6 describes the DC characteristics of different MIM diodes, including the polymer MIM diode. The temperature and thickness dependency of these diodes is also discussed. Chapter 7 covers the measurement section by concentrating on the low frequency and mm-wave response of MIM diode. Low frequency measurements yield rectification like behavior for the 100 μm^2 diode, whereas the 1 μm^2 diode operates well only at mm-wave frequency.

Chapter 8 concludes the research work by summarizing the development of MIM diode and provides suggestion for future directions of MIM junction based mm-wave detectors.

CHAPTER 2

BACKGROUND

2.1 Introduction

Thermal imaging can be done at various wavelengths, like millimeter and infrared (IR) wavelengths. At these wavelengths the primary source of mm and IR radiation is the heat radiation emitted by any object. However, the amount of IR power radiated by an object at a given temperature is much higher than power radiated at mm-wave as shown by the power radiation plot in Figure 2.1. Hence infrared has been the most commonly used wavelength for developing thermal imaging system. Moreover, many objects emits strong infrared radiation in the 10 μm wavelength [10], making IR systems suitable for thermal imaging.

Although infrared systems provide higher resolution (smaller wavelength), it suffers from many disadvantages such as (a) straight line of operation: the radiated or transmitted IR signal must be in line of sight to detect the object, (b) weather sensitivity: adverse conditions like dust, smoke, fog, etc., degrades the IR radiation, thereby reducing the system performance, and (c) blockage by common materials: wherein the radiation does not penetrate through many materials, hence provides a outline radiation map of the subject of interest [11]. Figure 2.2 shows the infrared image of a subject color coded to identify the hot and cold spots.

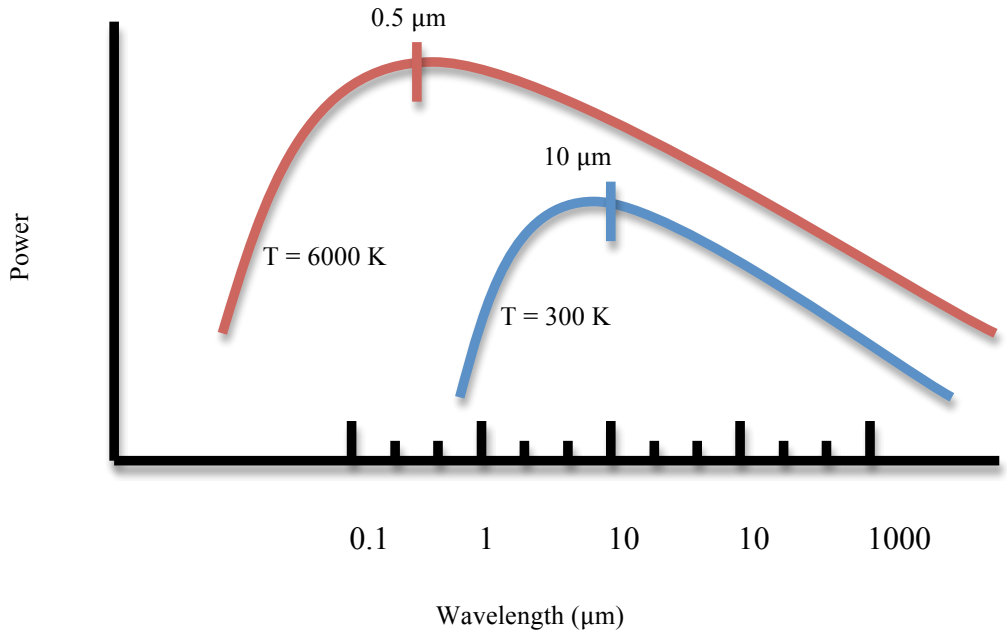

Figure 2.1: Power Radiated by an Object at Room Temperature. [8]

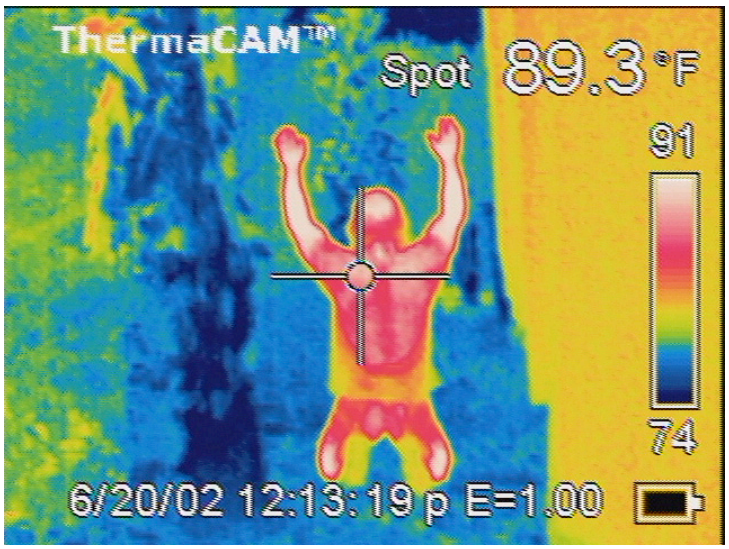

Figure 2.2: Thermal Radiation Map of a Subject As Seen From an Infrared Imaging System. From [12]

On the other hand, as mentioned in the previous chapter, mm-wave radiations are less affected in adverse conditions [9]. Although millimeter wave systems have lower resolution than IR systems, millimeter waves have better performance in poor weather conditions and can penetrate through many materials unlike infrared and optical waves. This has rekindled the interest in realizing mm-wave detectors for several commercial and military applications [9]. Figure 2.3 shows the millimeter wave image of a subject by penetrating through the clothing.

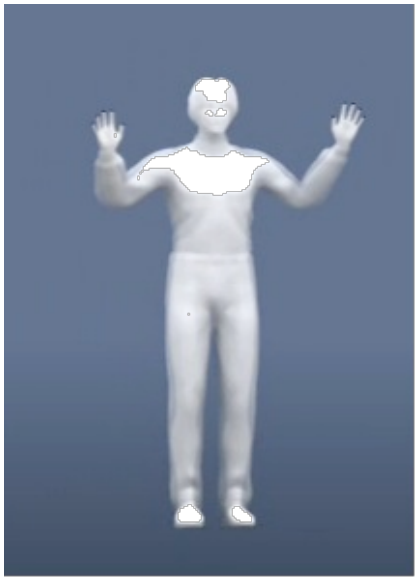

Figure 2.3: Millimeter Wave Image of a Subject by Penetrating Through the Clothing. From [13]

2.2 Millimeter Wave Detection

Millimeter wave detector operates as a transducer that converts the electromagnetic radiation to an electrical signal. Millimeter wave imaging/ detection has

been investigated and developed using various technologies. In general, mm-wave imaging is classified as (a) passive or (b) active imaging systems.

These systems can be operated as a point sensor or a remote sensor based on the device performance. In a point sensor, the object is located in close proximity to the sensor and a transmitter provides the mm-wave radiation. Because of the proximity, only little power is required to be transmitted. In a remote or a standoff sensor, the object and the sensor have a relatively larger separation; hence the object collects only a small fraction of the transmitted power. If this small fraction could be detected back at the receiver, the device is called *active* imaging system [14]. Devices operating without illuminating or transmitting an external radiation are called *passive* imaging system [14]. Some of the devices operating in passive and active mode are discussed in this section. In addition, the problems faced by these systems are also presented.

(a) *Passive mm-wave imaging:*

In a passive mm-wave imaging system, the image is obtained by natural electromagnetic radiation emitted from the object. All natural objects whose temperatures are above absolute zero emit passive millimeter-wave radiation [9]. As mentioned earlier mm-waves are much more effective (lower attenuation) than infrared in poor weather conditions [9]. Also, images produced by passive millimeter-waves have natural appearances [15]. In the mm-wave regime the atmospheric windows occur at 35 GHz, 94 GHz, 140 GHz, and 220 GHz and the choice of frequency depend on the specific application. Generally, in a passive imaging system, the image is affected when operated

indoors, due to lesser temperature differential between the objects radiation and background radiation. However, several companies such as Millivision, Trex Enterprises, Lockheed Martin and TRW, were working on producing passive mm-wave radiometric arrays.

Millivision initially developed mm-wave detectors using a standardized radiometric card with 8 x 8 channel array, but encountered several problems while attempting to form a larger array. The detector did not have enough sensitivity to detect objects under a cold sky. The gain and sensitivity could not be balanced. The system took a long time to produce enough independent pixels to form an image. Later by using an Indium Phosphide low noise amplifier (LNA) on a Monolithic Microwave Integrated Circuit (MMIC), the noise figures were minimized. Still, the detector suffers from not having enough pixels to form a clear representation of the object. Recently, Millivision has developed a gateway scanner to be used in airports and other public locations as a point source passive sensor operated by a Focal Plane Array (FPA) of LNA [16].

Trex Enterprises had initially developed a radiometric imager using opto-acoustic Bragg Cell. This system was large in size and was developed for battlefield imaging. Although this system could identify large metal objects under a cold sky, it could not detect concealed objects when operated indoors. The device performance proved poor when attempted to operate indoors. Later, a smaller lightweight antenna, LNA and an improved digital signal processor were employed to improve the device performance. The mm-wave radiations were detected directly using a MMIC. In spite of these improvements the sensitivity of the detector was lower when operated indoor [17].

Lockheed Martin developed a dual mode sensor with a sensitive infrared imager and mm-wave passive imager. A Cassegrain antenna with an IR camera was used in the system along with a direct detection LNA. The scan rate exhibited by this system was variable, which would increase the noise figure [17].

Millimeter wave imaging systems are also being developed using compound semiconductor materials like High Electron Mobility Transistors (HEMT), which makes the fabrication process very complex [18]. A research team at the Fraunhofer Institute for Applied Solid state Physics is developing InAlAs/InGaAs HEMTs for millimeter-wave imaging [18]. Also at the Chalmers University the detectors based on Heterojunction Barrier Varactors (HBVs) are being developed [19]. These are the current technologies that are being pursued for developing passive millimeter-wave imaging systems.

(b) *Active mm-wave imaging:*

Active imaging systems are those in which an illumination or radiation is transmitted by a source (radar) and the image is detected. Active systems work well indoors or outdoors unlike passive imaging systems. Active imaging systems were initially developed for through-the-wall detection system (using long wavelength). Later, it was developed for operating in shorter wavelengths. Since an active imaging system illuminates the target to collect information, a few health concerns are posed. However, the radiation transmitted from an active imaging system is less than most of the routinely used wireless systems. Figure 2.4 shows the schematic of an active millimeter wave detector.

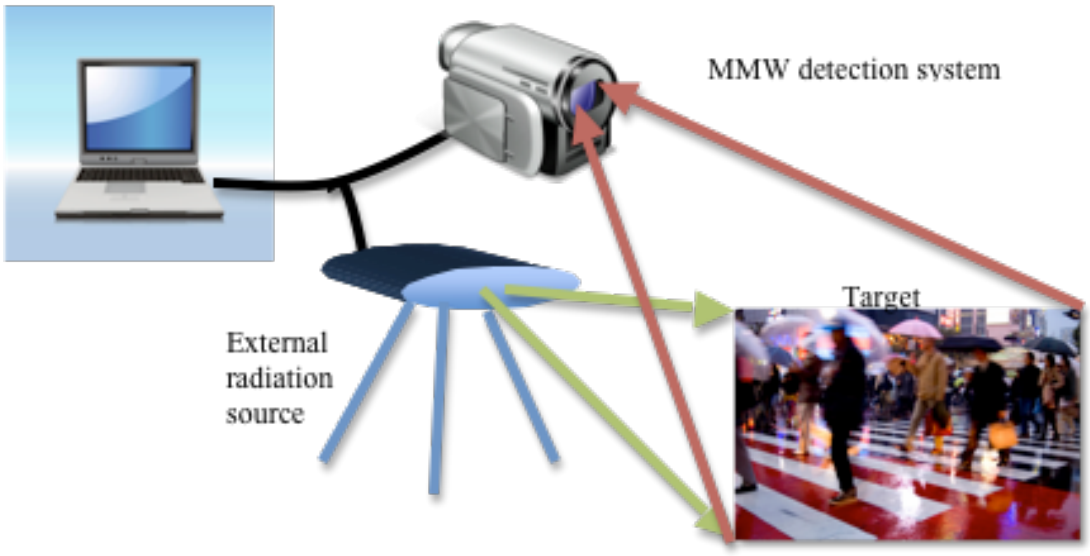

Figure 2.4: Schematic Representation of an Active Millimeter Wave Imaging System. From [20]

Some of the active imaging systems recently pursued are,

(a) Terahertz absorption spectroscopy by Intelligent Optical Systems [21]. The absorbance spectra via both transmission and reflection are obtained and matched with the selected signature wavelength to identify the concealed object. This method utilizes the absorption spectra of a chemical and matches with the target to identify the target. The detection of this system is limited only to chemical substances.

(b) Terahertz Standoff Imager with heterodyne detectors using Quantum Cascade lasers by Spire Corporation [22]. This approach uses a terahertz Fourier Transform Interferometer (FTIR) and a heterodyne detection system to increase the sensitivity. A horn antenna is used to transmit the radiation to illuminate the target and detected using

the FTIR. This technique was proposed as a remote active imaging system operating at 50 meters target distance.

(c) Electromagnetic Concealed Weapon Detection (CWD) by Pharad, LLC [23]. In this approach, a wideband mm-wave signal is transmitted to excite the natural resonance on a concealed weapon and an electromagnetic signature of the specific object is matched with the signature in the database. This approach has a potential to create false alarms since many materials have to be identified to match to the target.

(d) Non-linear acoustic concealed weapon detection (CWD) by Luna Innovations, Inc. [24]. This technique utilizes the audio sound to penetrate through clothing and identify the resonance of different material. However, the sound wave spread too quickly and also gets attenuated. Hence an advanced processing technique in needed to classify the sample signature to distinguish different objects.

(e) Active mm-wave radar for CWD by Personal Protection Technologies, Inc. [5]. This techniques proposed to use off-the-shelf collision avoidance radar operating at 77 GHz and use it to transmit and receive radiation to a camera, controlled by a computer. At 77 GHz, the attenuation will be more and the resolution will also be compromised.

(f) Magnetic signature analysis by Idaho National Laboratory [20]. This approach uses a magnetic signature procedure to identify targets. Advanced signal processing is required to discriminate targets.

(g) Focal plane array based mm-wave imaging system is developed by Lockheed Martin [17]. This utilizes Vanadium oxide based bolometer for detecting the resistance

change, which is calibrated to the temperature of the radiation. The bolometer is developed as a pixel when subjected to radiation. However, the devices suffer from slow response time [17].

In general, the mm-wave imaging systems developed so far suffer from various problems such as large size, weight, complex device development, poor sensitivity, long integration time and poor imaging capability. Hence, there exists a need for developing a high efficiency mm-wave detector with simpler fabrication technique in a compact configuration for varied applications. This may be possible by making a shift towards the antenna-coupled detectors. In an antenna-coupled detector, the antenna is used to couple the electromagnetic energy to a rectifying element with smaller dimensions than the wavelength of the incident radiation. By using a wide band antenna, an entire range of wavelengths can be captured efficiently and converted as a useful energy. In addition, due to the operating frequency, the device sizes are much smaller making the mm-wave device compact and portable.

2.2 Antenna-Coupled Detector

Antenna coupled detectors or Rectennas have been explored for the past two decades mainly for microwave applications, infrared detection, terahertz imaging [1], [4], [25], [26], [27], [28] and even energy harvesting [29]. Antenna-coupled detectors with bolometers, metal-insulator-metal (MIM) diodes [2], [3] and schottky diodes [30] have been used for detection in the sub-mm-wave and mm-wave regions with various antenna configurations. They are discussed hereunder.

A bolometer is a device used for measuring the energy of the incident electromagnetic radiation [31]. It consists of a resistive element constructed from a material with a very small thermal capacity and a large temperature co-efficient so that the absorbed radiation produces a large change in resistance [27]. Typically bolometers are fabricated using metals and metal oxides like Nickel, Bismuth, Niobium, Platinum, Antimony or Vanadium Oxide [27]. The devices are operated at room temperature, and have response time of 10^{-3} seconds with a low sensitivity [27]. Nevertheless, metal film bolometer arrays have been fabricated and employed in IR sensors coupled with antenna array due to ease of fabrication [32], [33], [34]. But the devices are generally fragile, thus limiting their use in certain applications [27]. Recently, research has been conducted to develop bolometers with semiconductors and other composite materials to increase the sensitivity [27].

On the other hand MIM diodes are more stable device that provides a much faster response (10^{-15} seconds) [27] and higher sensitivity than bolometers [27]. Higher sensitivity values lead to greater detectivity. Historically, antenna-coupled MIM diodes have been used for imaging and detection in long wave IR (LWIR) regime. By scaling the device area, the same concept can be utilized for mm-wave detection.

As mentioned in the previous chapter, MIM diodes consist of two metal electrodes separated by a thin insulator layer. Typically MIM junctions were fabricated using a base metal electrode, the native metal-oxide and another top metal electrode. Initially point contact MIM diodes also known as cat-whiskers combined with wire antennas were used for sub-millimeter wavelength detection and mixing [3]. A schematic

of point contact diode fabricated using a metal wire in contact with another metal plate is shown in Figure 2.5.

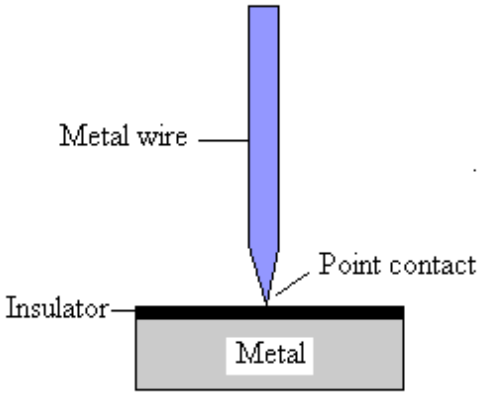

Figure 2.5: Schematic Illustration of a MIM Diode Fabricated Using Point-Contact Configuration

These types of diodes were difficult to fabricate since the barrier layer that was formed was due to dirt collected on the surface or a native oxide layer forming a barrier layer. In spite of the reproducibility issues, the point-contact diodes were fabricated and used in the communication field for over twenty years in high frequency rectification from a few GHz to 150 THz [29], [35]. But the drawback was the integration and stability of a point contact MIM configuration in the infrared and optical region. Due to the instability of point-contact diodes, thin film MIM diodes were utilized. Thin Film MIM diodes consist of an insulator layer sandwiched between two metal electrodes integrated on a substrate. With the advent of photolithography, stable and reproducible thin film MIM junctions could be fabricated. Although stable and reproducible thin film MIM

junctions can be manufactured, the development of a MIM array with smaller area is a challenge.

Various research groups have fabricated and investigated the concept of MIM tunneling with different thin film metals such as Al-Al_2O_3-Al [36], Cr-CrO-Au [29], [37], Al-Al_2O_3-Ag [38], Nb-NbOx-Au [29]. However, published reports state that only few research groups have investigated the development of MIM junctions for mm-wave detectors. Most research groups have fabricated MIM junctions for IR detection using same metal electrodes. Table 2.1 shows the thin film MIM junctions fabricated by different groups and its sensitivity values.

Table 2.1: Thin Film MIM Junctions Developed by Various Research Groups

Research Group	*Type of MIM*	*Junction Area*	*Sensitivity*
Heiblum et. al. [39]	Ni-NiO-Ni	3.8 μm^2	4.3 V^{-1}
Hoofring et. al. [4]	Ni-NiO-Au	0.64 μm^2	4.55 V^{-1}
UCF – CREOL [26]	Ni-NiO-Ni	0.075 μm^2	2.75 V^{-1}
ETH, Zurich [40]	Ni-NiO-Ni	0.056 μm^2	1.6 V^{-1}
UND [41]	Ni-NiO-Pt	0.0025 μm^2	-13 V^{-1}
UND [41]	Al-Al_2O_3-Pt	0.0025 μm^2	1.3 V^{-1}
UND [41]	Al-Al_2O_3-Ni	0.0025 μm^2	1 V^{-1}
UND [41]	Al-Al_2O_3-Al	0.0025 μm^2	-1.4 V^{-1}

As seen from the table most of these junctions yielded low sensitivity value. In order to achieve better device performance, MIM junctions need to be fabricated with two different metal electrodes. The need for using different metal electrodes is discussed in the next chapter.

In summary, the antenna coupled MIM detectors offer a new dimension in sensing with many advantages over other imaging techniques. MIM junctions offer more advantages than the existing bolometer in the areas of imaging parameters, like detectivity, sensitivity etc. Another benefit of the proposed technology is the ease of fabrication and the ability of the device to operate at room temperature. These sensors have no mechanical parts and are made of solid state devices which can be fabricated with the standard processing techniques making them CMOS compatible allowing them to integrate with external circuitry. Thus, when developed, these detectors would provide outstanding night vision capabilities and concealed weapon detection systems, yet come in compact, lightweight and powerful designs. That, in turn, would cut manufacturing costs considerably and would speed up the use of imaging sensors for an entire new category of applications, including medical equipment, robotics and micro-air vehicles.

CHAPTER 3

METAL INSULATOR METAL TUNNEL DIODES

A MIM tunnel junction is a thin film device, which consists of two metallic plates separated by a very thin insulating layer. It is a quantum device and rectification takes place when electrical charges flow from one side to another by overcoming the potential barrier. The tunneling mechanism causes the detection of an applied AC signal resulting in a dc output component. MIM tunnel junctions are typically developed with a small contact area governed by a relationship between operating frequency and the capacitance of the tunnel junction. Thus in this section, the tunneling current and frequency-area relationship of the junctions that explain the operation of MIM tunneling are presented. Figure 3.1 shows the schematic of electron tunneling through a barrier layer.

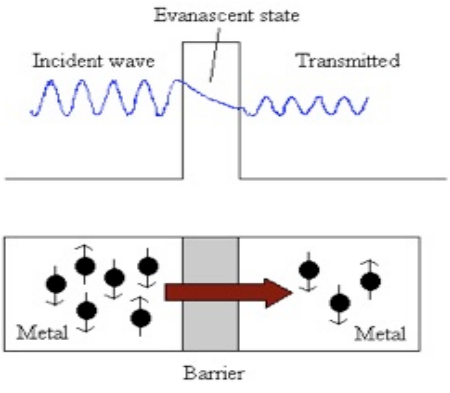

Figure 3.1: Schematic Illustration of an Electron Tunneling Through a Finite Barrier in a MIM Junction. From [42]

3.1 Theory of Operation

The operation of MIM diode can be better understood by observing the energy band diagram for an asymmetric MIM junction at equilibrium, shown in Figure 3.2. The figure shows an insulator layer with a thickness (s) between two dissimilar electrodes with different work function. Work function is the minimum voltage required to displace an electron from the Fermi level to the vacuum level. The work functions of metal 1 and metal 2 are denoted by ψ_1 and ψ_2, respectively. The barrier height is the minimum energy required to move an electron from the metal to the conduction band. The barrier heights of metal 1 and metal 2 are given by ϕ_1 and ϕ_2, respectively.

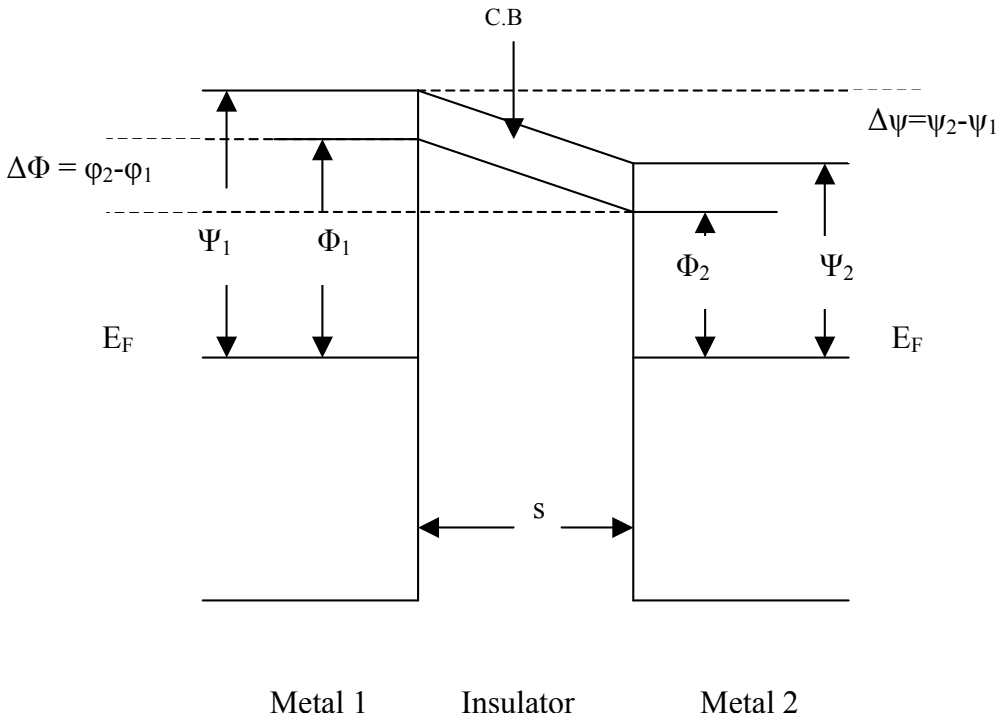

Figure 3.2: Energy Band Diagram of MIM Diode at Zero Bias

When the metal is brought into contact with an insulator layer, thermodynamic equilibrium requires a continuous Fermi level be established across the interface denoted by E_F. Here the electron in either metal meets a constant potential energy barrier ϕ_o at the interface of metal and insulator, given by,

$$\phi_o = \psi_m - \chi \qquad (3.1)$$

where, ψ_m is the work function of the metal and χ is the activation energy of the insulator [43].

The barrier height and work function of the metal are related by,

$$\phi_1 - \phi_2 = \Delta\phi = \psi_1 - \psi_2 = \Delta\psi \qquad (3.2)$$

Hence by determining the barrier height of one metal, the other barrier height can be determined using the above relation. But practically, the interface of metal-insulator cannot have a straight-cut trapezoidal potential barrier. Instead, the barrier interface will be a smooth transition due to image forces, which arise due to the coulomb interaction between an electron-induced charge in the nearby conductors (exertion of an attractive force on the electron) [43]. As the electron approaches the dielectric layer, it induces a positive charge on the interface, which acts like an image charge within the layer and reduces the barrier height by rounding off the corners and narrowing the barrier [44] as shown in Figure 3.3.

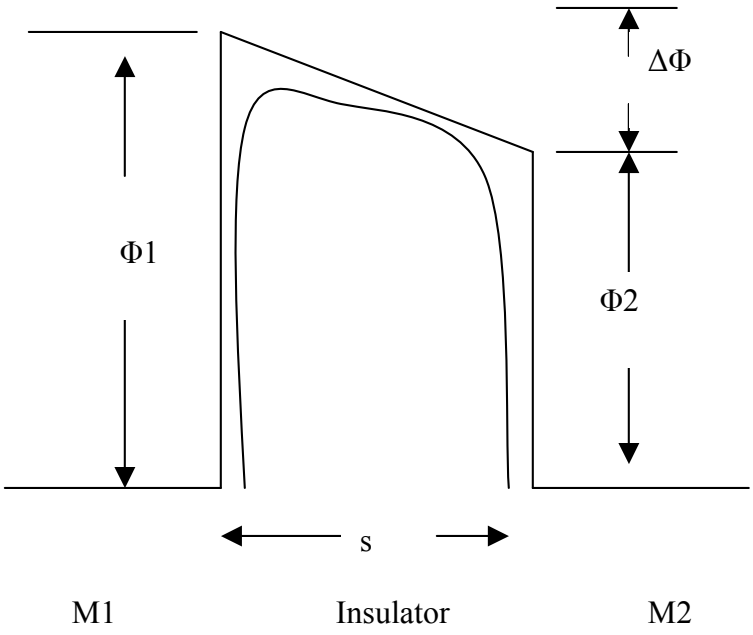

Figure 3.3: Energy Band Diagram of MIM Diode Showing Barrier Lowering due to Image Force

However, if the barrier height difference between the two metals is high enough, electrons can tunnel through the insulator without any dc bias. Based on the work function of the two electrodes, the energy band diagram will show more asymmetry and rectification. When a bias voltage is applied between the two metal electrodes, more current flows through the insulator. The current response by varying the bias voltage has been shown to be a non-linear behavior [39] and the rectifying characteristics of the MIM diode arise from the asymmetry in the current-voltage (I-V) characteristics.

The effect of bias voltage between the two electrodes displaces the Fermi levels of the two electrodes relative to each other. The Fermi level of the negatively biased electrode is moved upward on the energy scale. The electrical characteristic is taken to be

forward characteristics, when the metal with lower work function is positively biased and a reverse characteristic when it is negatively biased.

Applying a bias voltage consequently modulates the height of the potential barrier. When either of the Fermi level is raised, the height of the barrier is lowered. This is because the barrier potential is referenced to that Fermi level which is higher on the energy scale. When a bias of either polarity is applied, one of the two Fermi levels is elevated, thereby increasing the reference energy level. Thus the maximum barrier height for the MIM structure occurs at zero-bias.

Similarly, the barrier width is also affected by applying a bias voltage. The barrier width is defined as the distance between two metal-insulator points at zero-bias Fermi level. When a bias voltage is applied, the Fermi level is moved above the reference energy level. This facilitates the electrons to tunnel through a minimal thickness, due to barrier lowering. Thus, the electron can tunnel through the insulator with more probability of finding itself on the other side.

This behavior is mainly due to the difference in the work functions of the two metals. The limiting factor in the potential performance of a MIM diode is the difference in the work functions of the two metals. The work function of the metal can also affect the potential barrier the same way as the applied bias. In order to achieve a high degree of asymmetry in the I-V curve it is therefore desirable to use metals with highly different work functions.

3.2 Current-Voltage Characteristics

Typically the I-V characteristic of a MIM diode is measured under forward biased condition. As mentioned in the previous section, when the diode is forward biased, the average height of the barrier lowers thereby increasing the tunneling probability and hence the current flow. The tunneling probability is increased when the barrier width of the insulator is also extremely thin. The current obtained from the MIM structure was modeled by Simmons [43] using the Sommerfeld and Beth Model and WKB approximation. An approximate expression for the tunneling current in the MIM system can be written as,

$$J = \frac{Jo}{\Delta s^2}[\Phi \exp(-A\Delta s\sqrt{\Phi}) - (\Phi + eV)\exp(-A\Delta s(\sqrt{\Phi + eV})] \qquad (3.3)$$

where, J is the current density at every voltage instance in A/cm^2, Jo and A are constants, ΔS is the effective barrier thickness in Å units and Φ is the mean barrier height in V.

The tunneling current can also be determined according to the bias voltage (V_b) applied to the tunnel junction. At low voltages, when the mean barrier height $\Phi = \frac{(\phi_1 + \phi_2)}{2}$ >> V_b equation 3.3 can be simplified as,

$$J = \frac{\gamma\sqrt{\Phi}V}{\Delta s}\exp(-A\Delta s\sqrt{\Phi}) \qquad (3.4)$$

where $\gamma = \frac{e\sqrt{2m}}{4B\pi^2\hbar^2}$, and A is a constant. Since the mean barrier height $\Phi >> eV$, we

can consider that Φ does not depend on V. Thus in the case of small voltage, the tunneling current in proportional to the applied bias. Figure 3.4 shows the effect of potential barrier at low voltages exhibiting minimal change in the band diagram.

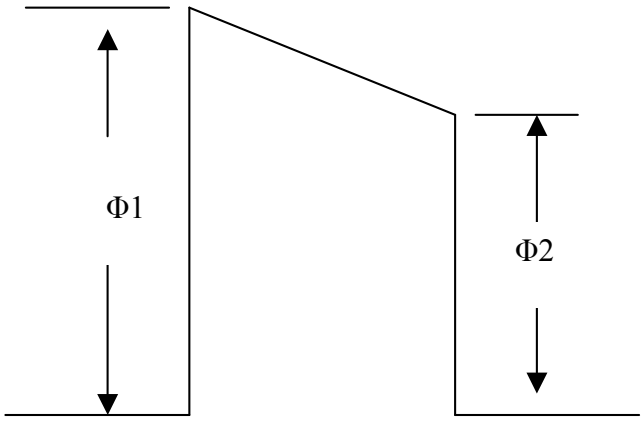

Figure 3.4: Effect of Applying Low Voltages to the Potential Barrier

When the bias voltage is increased such that $\Phi_2 > V_b$, the tunneling is governed by another equation for intermediate voltages given by,

$$J = \frac{\gamma\sqrt{\Phi}}{\Delta s}\exp(-A\Delta s\sqrt{\Phi})(V + \sigma V^3) \tag{3.5}$$

where, $\sigma = \frac{(Ae)^2}{96\Phi\Delta s^2} - \frac{(Ae^2)}{32\Delta s\Phi^{3/2}}$, $\Delta s = s$ and $\Phi = \frac{(\phi_1 + \phi_2 - V)}{2}$. Figure 3.5 shows the effect of potential barrier at intermediate voltage range.

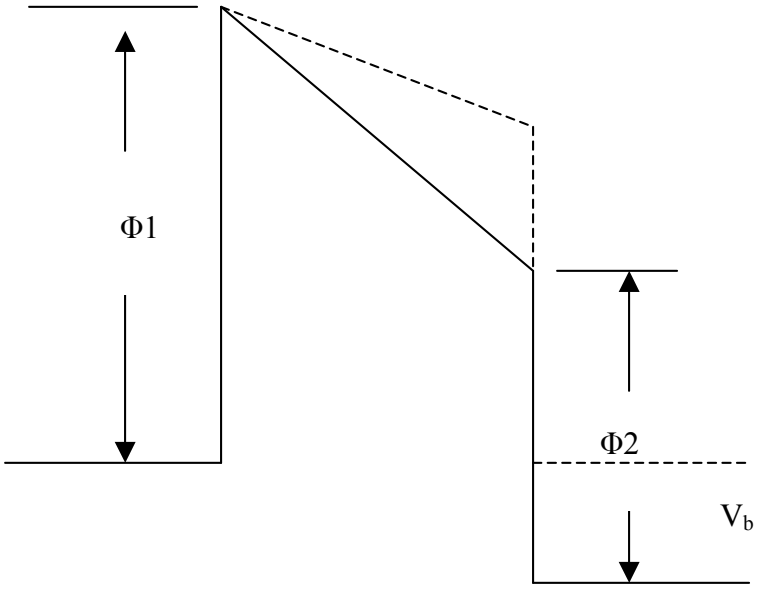

Figure 3.5: Effect of Potential Barrier at Intermediate Voltage Ranges

When the bias voltage is increased over the barrier height, i.e., $V_b >> \phi 2$ the tunneling current is best explained by Fowler-Nordheim equation [45], given as,

$$J = \frac{q^2 E^2}{4\pi h \phi_0} [\exp(\frac{-E_o}{E})] \qquad (3.6)$$

where q is the charge of the electron, E is the electric field across the junction, h is the Planck's constant, ϕ_o is the barrier height and $E_o = (8/3)(\pi q)^{1/2}(\phi_o)^{3/2}$. Figure 3.6 shows the potential barrier in the MIM system at large voltage. At very high bias voltages the electrons instantaneously tunnels from metal 1 to metal 2 due to lowering of barrier height and width exhibiting a sudden increase in current. Thus, from the electrical

behavior it can be observed that the diode characteristic is highly correlated with its dielectric thickness and hence significantly depends on the fabrication methodologies adopted to develop the device. A typical forward current-voltage characteristic of a MIM junction is shown in Figure 3.7.

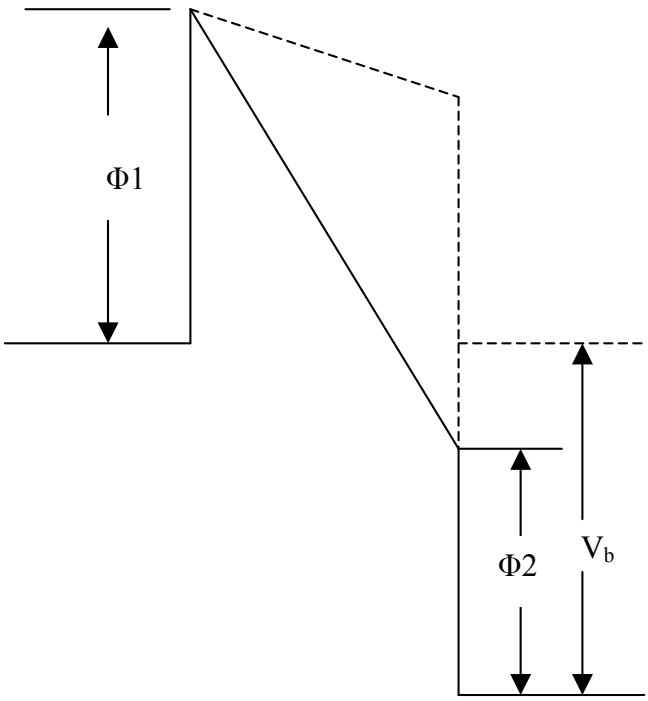

Figure 3.6: Effect of Potential Barrier at Very High Voltages

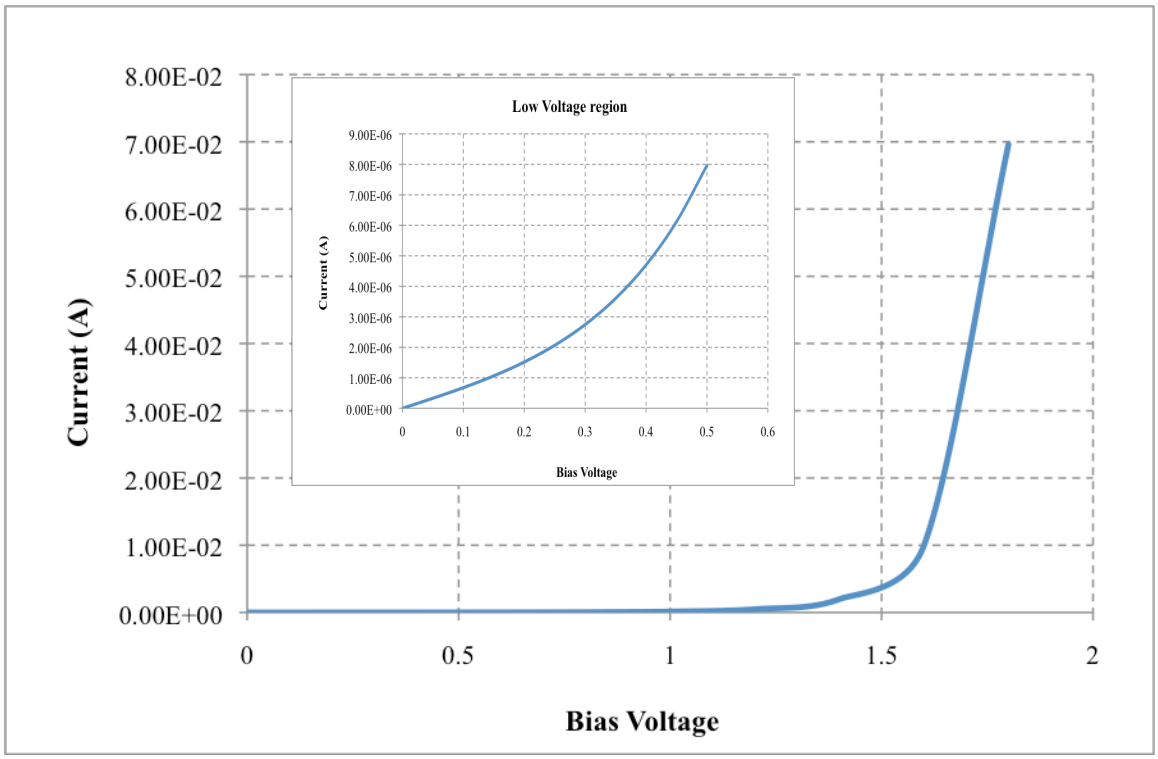

Figure 3.7: Theoretical I-V Plot of MIM Junctions Operated in the Intermediate Voltage Ranges. Inset Shows the I-V Plot at Low Voltage Range.

3.3 Frequency and Area Relationship

MIM tunnel junctions can be considered as a parallel plate capacitor with a thin dielectric layer sandwiched between two electrodes. Hence, the operational frequency of the tunnel junctions is determined using the capacitance of the tunnel junction. According to Sanchez et al., [46] the cut-off frequency of the device is defined as,

$$f_c = \frac{1}{2\pi R_a C_d} \qquad (3.7)$$

where,

f_c is the cut-off frequency of the device,

R_a is the antenna resistance, and

C_d is the capacitance of the diode

Detection is still possible beyond this cut-off frequency, but the detectivity of the MIM diode decreases by $(f_c)^{-3}$. Thus as R_a is determined by the fabrication process it can be treated as a constant for a given process. The estimated frequency of operation of a MIM diode can be calculated by determining the capacitance of the device. The capacitance of the MIM junction is given by the parallel-plate capacitor equation as,

$$C = \frac{\varepsilon_o \varepsilon_r A_d}{s} \qquad (3.8)$$

where, ε_r is dielectric permittivity of the insulator, A_d is the active area of the diode and s is the thickness of the insulator.

From (3.7) and (3.8) it can be noted that the operation frequency of the tunnel junctions is increased by reducing the capacitance of the device. In order to reduce the capacitance, the contact area A_d or the dielectric constant has to be reduced or the insulator thickness s has to be increased.

For operating the device at 3mm, a diode with cut-off frequency over 94 GHz is needed. By decreasing the contact area or increasing the insulator thickness a smaller capacitance value can be obtained. However, from the current vs. voltage equations it can be seen that the current density of the tunnel junction is exponentially dependant on the insulator thickness. Hence to reduce the capacitance of the tunnel junctions it is preferred

to maintain the thickness of the insulator at a nominal value for electron tunneling (< 4 nm), while reducing the contact area of the diode.

Based on the aforementioned equations MIM junctions have been fabricated by various research groups with same as well as different metals. From the energy band diagram of MIM junctions it is understood that by using metals with different work functions, an asymmetric behavior can be achieved. Furthermore, the asymmetry can be increased when the work function between the two metal electrodes is large enough. Table 3.1 shows the work function of different metals commonly used in developing MIM junctions. Various materials used for fabricating a MIM junction with different electrodes is discussed in Chapter 5.

Table 3.1: Work Function of Various Metals Used for Fabricating MIM Diodes. From [47].

Element	*Work function (eV)*
Cr	4.5
Ni	5.15
Al	4.3
Au	5.1
Pd	5.1
Pt	5.65
Nb	4.3
Ag	4.26

CHAPTER 4

PROCESSING TECHNIQUES

4.1 Microfabrication

The fabrication of MIM diodes mainly involves optical lithography as well as SEM based electron-beam lithography to pattern diodes with different dimensions. In this section a detailed description of photolithography and e-beam lithography process used to define the diode structure is presented.

4.1.1 Optical Lithography

Lithography is a process of transferring geometric shapes on a master pattern to the surface of a substrate. Optical lithography is used for producing integrated circuits with high-density small-scale features on to a substrate. Typically, optical lithography is performed using an ultraviolet lamp with a strong UV signal at the “g-line” (436 nm) or “i-line” (365 nm). For achieving feature sizes in the nm range deep-UV lithography is used. For developing the MIM diode we used a “g-line” lithography tool from EV Group (EVG 620) and Quintel (QC-6000). The mask aligners used for fabricating the MIM diodes are shown in Figure 4.1(a) and 4.1(b). This tool also has the capability to do backside alignment, which was utilized to develop the millimeter wave MIM diode.

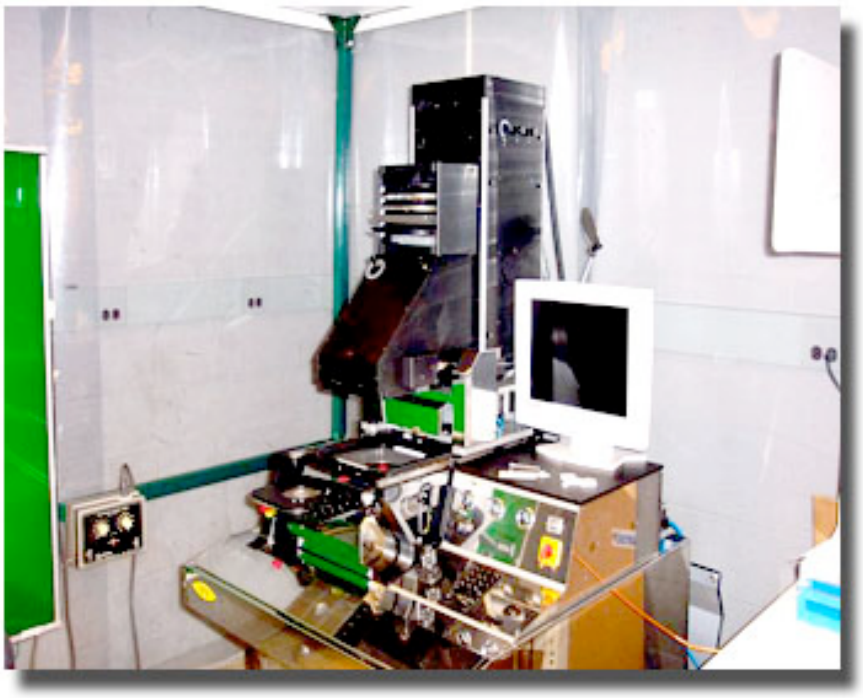

(a)

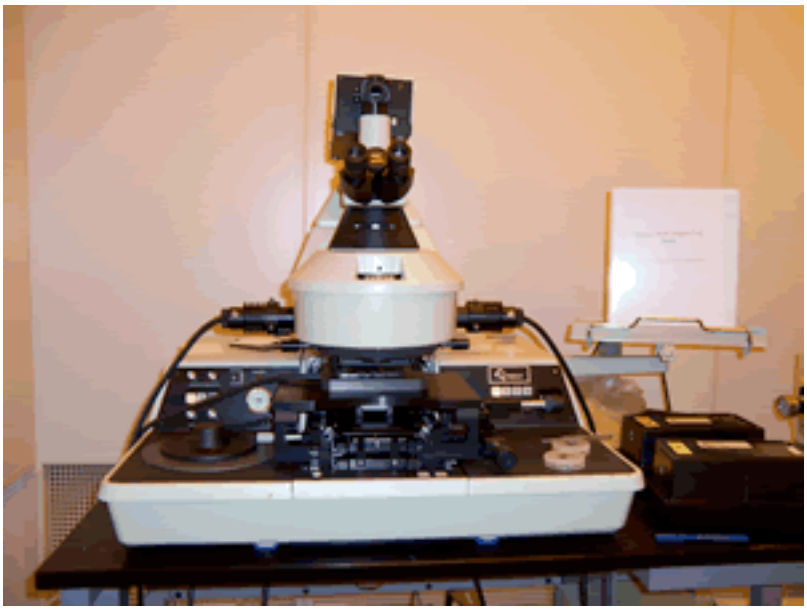

(b)

Figure 4.1: Visual of (a) EVG 620 and (b) Quintel Mask Aligners

Generally, the photolithography process involves several steps before the substrate can be used for metallization or thin film deposition. The steps involved in the photolithographic process are wafer cleaning, photoresist application, soft baking, mask alignment, exposure and development, and hard baking. A brief overview of each process is presented.

(a) *Wafer Cleaning and Photoresist Application:* This is the initial procedure in the lithography process. The wafers are thoroughly cleaned to remove any particulate matters from the surface. Then photoresist is applied to wafer surface by spin coating to form a thin layer.

(b) *Soft Baking:* Soft-baking done after coating the wafer with the photoresist. Soft baking removes the solvents from the resist coating. The photoresist coatings become photosensitive only after soft baking.

(c) *Mask Alignment and Exposure:* The wafer coated with photoresist is loaded in the mask aligner and aligned with a mask, which has the master patterns. Each mask after the first one must be aligned to the previous pattern. After aligning the wafer to the patterns, the photoresist is exposed by a high intensity ultraviolet light.

(d) *Development:* After the wafer is exposed, the pattern is developed in the resist by immersing the wafer in a photoresist developer. The developer dissolves the un-polymerized resist regions and differentiates between the exposed and unexposed regions.

(e) *Hard Baking:* Hard baking is the final step in the photolithographic process. This step is necessary in order to harden the photoresist and improve adhesion of the photoresist to the wafer surface [48].

4.1.2 Electron-beam Lithography

E-beam lithography (EBL) is a lithographic process wherein a beam of focused electrons is scanned across an e-beam sensitive resists to produce very fine patterns. In an E-beam lithography system patterns as small as 10 nm can be produced. The pattern size is dependant on the electron accelerating voltage. Typically, EBL systems can operate at high accelerating voltage in the order of 10 – 50kV offering higher patterning capability than optical lithography due to its shorter wavelength.

As mentioned earlier, E-beam lithography is used to pattern devices beyond the optical lithography limit. In this work, although the devices dimensions were 1 μm^2, the e-beam lithography technique has been utilized to fabricate the devices due to the unavailability of a high-resolution optical lithography system. The E-beam lithography tool used for this research work is a scanning electron microscope (SEM) modified to be used as an e-beam litho writer. J.C. Nabity's Nano-Pattern Generation System (NPGS) was used with a JEOL JSM840 SEM to perform the e-beam lithography shown in Figure 4.2. A schematic of the SEM E-beam litho controlled by NPGS is shown in Figure 4.3.

Figure 4.2: JEOL JSM840 Controlled by Nabity's Nano-Pattern Generation System. Courtesy NNRC

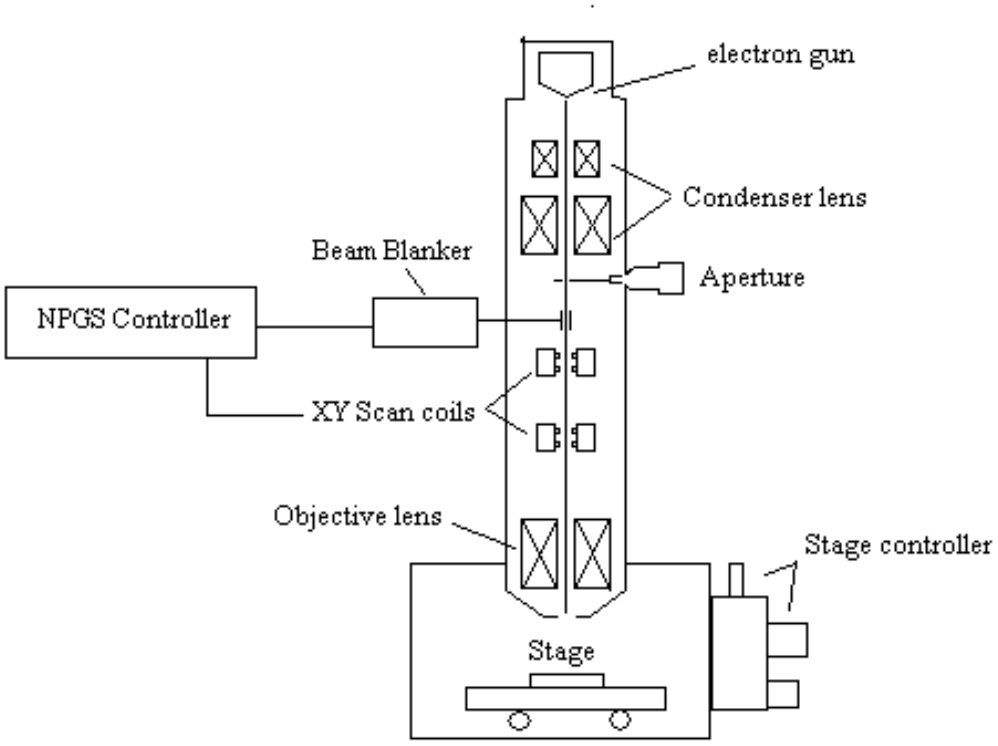

Figure 4.3: Schematic of JEOL JSM840 [49]

The JEOL JSM840 SEM has a tungsten filament operating by thermionic emission. The electrons emitted from the tungsten filament are accelerated towards an anode. The condenser lens does the primary focusing of the e-beam. The objective lens aperture serves to stop any stray electrons passing through the system i.e. clean the beam. We use a 75 μm objective lens aperture, which is the lowest setting on the system. Astigmatism present in the e-beam is corrected by special type of electron lens called the stigmators. Astigmatism arises due to the imperfections in the construction and alignment of the e-beam column. The objective lens does the final focusing of the beam onto the

substrate. The condenser and objective lenses are electron lenses that use magnetic fields to focus e-beams. The beam blanker is used to turn the beam on and off. It is a parallel plate with an applied potential that electrostatically deflects the beam. XY scan coils are used for beam deflection off of the optical axis and hence scanning the beam to desired locations across the substrate. Both the beam blanker and the XY scan coils are controlled by the NPGS system. The NPGS uses a 16 bit digital-to-analog (DAC) converter to control the SEM XY scan coils [50]. It also handles turning the beam on and off by taking over the beam blanker controls.

E-beam lithography Process

Polymethyl methacrylate (PMMA) is the e-beam sensitive resist used for lithography throughout this work. It is a positive high resolution resist that is widely used in e-beam lithography. However, it is a low sensitivity resist. The JEOL JSM 840 requires a dose of about 140 $\mu C/cm^2$ to etch the PMMA. PMMA is spin coated on the surface of a substrate and the thickness of the PMMA film is determined by the spinning speed. PMMA is then baked on a hot plate at 180°C for 2 minutes. When the PMMA is exposed to the e-beam, the polymer chains are broken leaving the exposed areas more soluble in the developer. Methyl-isobutyl-ketone (MIBK) is used as a developer to dissolve the exposed areas in the PMMA film. MIBK being a strong developer is usually mixed with isopropanol (IPA) in a ratio of 1:3 to prevent dissolving unexposed areas of the resist.

The patterns are defined on the substrate by an additive process as shown in Figure 4.4, wherein the resist is spun on the substrate. The resist is then exposed and developed resulting in the removal of the resist from the areas it was exposed. A thin film is then deposited covering the entire surface of the substrate. The substrate is then immersed into a solution that dissolves the resist. The resist dissolves and the thin material above it is lifted off leaving only the deposited material on the exposed areas.

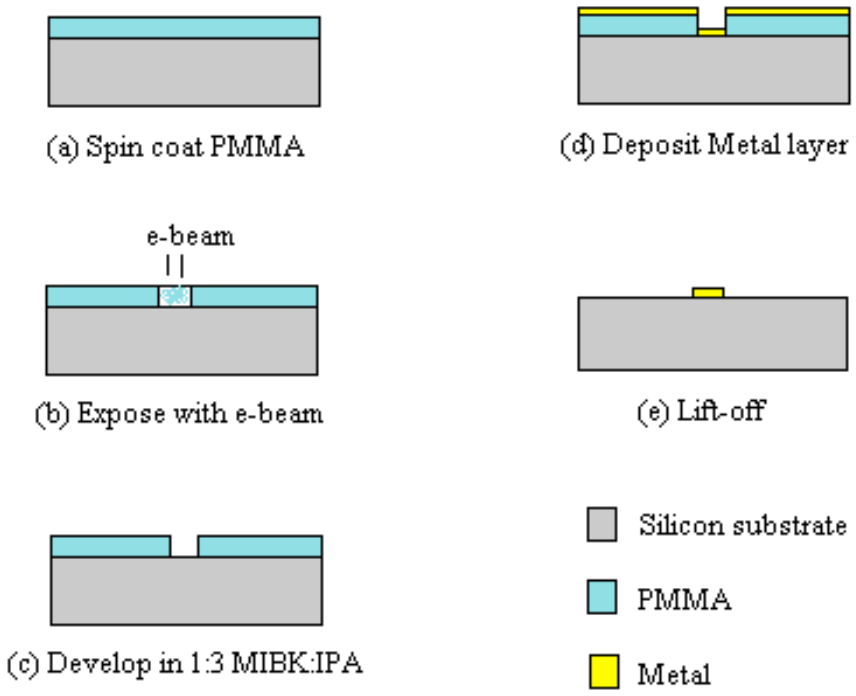

Figure 4.4: Process Sequence for E-beam Lithography

The optical lithography technique was used for developing a prototype diode and E-beam lithography was used for fabricating the high frequency diode. The metal and

dielectric deposition techniques followed were the same for developing both diodes. The design and fabrication process are discussed in the next chapter. The next section presents the deposition methods used for fabricating the MIM tunnel junctions.

4.2 Thin Film Deposition

The patterned MIM diodes are metalized using physical vapor deposition methods, namely DC sputtering and thermal evaporation. These are the thin film deposition techniques used to fabricate the devices in this research. Sputtering is a high-energy process making the metal deposition fairly homogeneous, while evaporation yields thin films that are well suited for lift-off techniques. Moreover, the choice of using evaporation or sputtering as a deposition technique was due to the availability of materials.

4.2.1 Sputtering

The main application of sputtering is for the deposition of thin films. Sputtering is a physical vapor deposition (PVD) technique used for precision coatings of thin films in vacuum. In sputter deposition unlike other vacuum deposition processes, the material usually arrives in atomic or molecular form. The atom diffuses around the substrate with a motion determined by its binding energy to the substrate. Usually the atoms migrate and then re-evaporate and combine with other atoms to form nucleation sites. This in turn grows into an island. Eventually the islands grow large enough to touch; this is the agglomeration or coalescence stage. The coalescence proceeds until the film reaches

continuity, this may not occur in some cases until the film is several hundred Angstroms in average thickness [51].

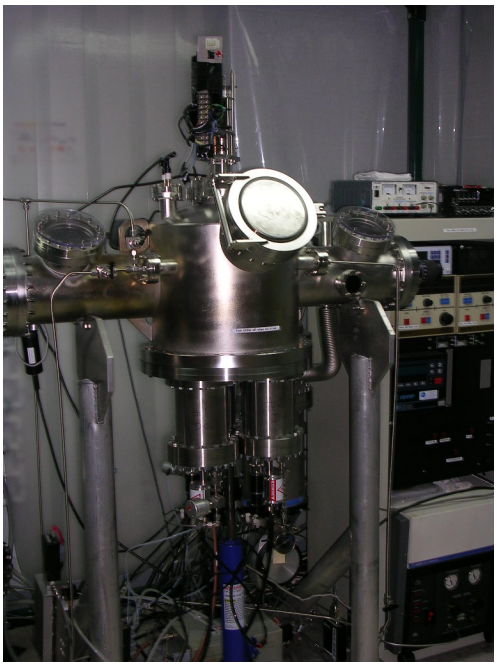

Figure 4.5: Sputtering Chamber Used for Depositing MIM Layers

The sputtering chamber used for this project is shown in Figure 4.5. The substrate is placed in a vacuum chamber with a target of the material to be deposited. Plasma is generated in a passive source gas like Argon in the chamber, and the ion bombardment is directed towards the target, causing material to be sputtered off the target and condense on the chamber walls and the substrate. Sputtering can either be RF or DC. A strong magnetic field (magnetron) can be used to concentrate the plasma near the target to increase the deposition rate. The deposition rate depends on the pressure, gas flow rate,

RF power, substrate temperature and target-substrate spacing. The sputtering system used for this project was a home built system with two DC guns and one RF gun. For this project DC power source was utilized to deposit the metals. The thickness of the deposited material is measured using a quartz crystal monitor. The substrate is kept at a distance of 10cm from the target and a DC motor constantly rotates it in order to get a uniform metal deposition. Thus the metal deposition is done using the sputtering system.

4.2.2 Reactive Sputtering

Reactive sputtering is a process wherein a conducting elemental target is DC sputtered, and the sputtered material is combined chemically with a component such as oxygen in the gas phase with an inert working gas (Argon). Typically, RF sputtering is used for depositing insulators such as silicon dioxide or metal oxides. However, using the plasma oxidation or reactive sputtering technique can also activate a compound formation. The chemical reaction for sputtering may take place at the cathode, during transport of ejected atoms, at the film surface or a combination of these possibilities [51]. Also, the role of each process depends much on the pressure and the chemical activity of the reacting species. A schematic of the reactive sputtering process is shown in Figure 4.6.

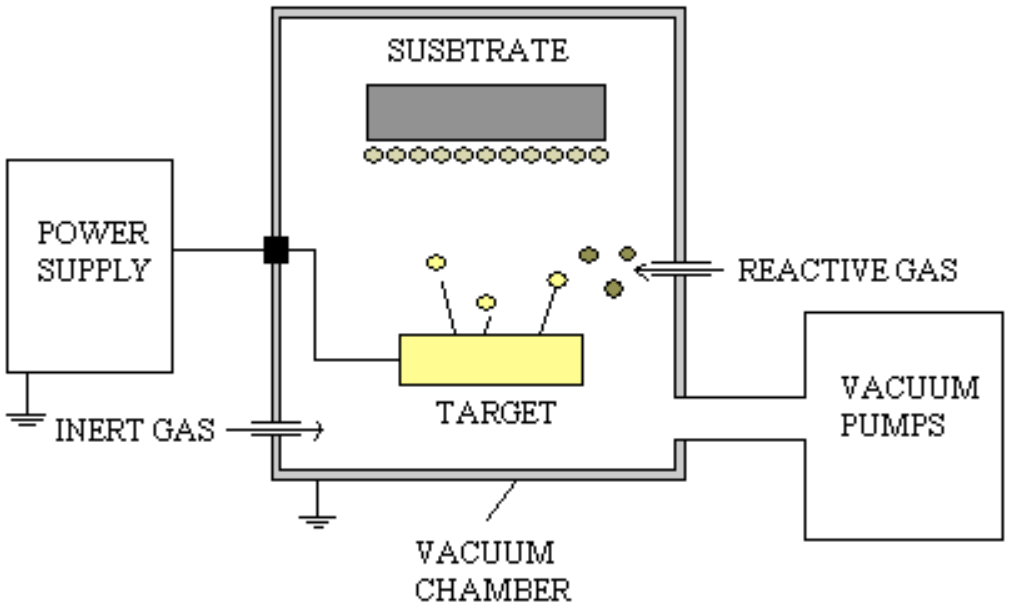

Figure 4.6: Schematic Illustration of a Reactive Sputtering System

4.2.3 Evaporation

Metal evaporation can be done by utilizing E-beam and thermal techniques. In an e-beam evaporation electrons are focused on a graphite crucible containing the metal of interest, which melts the materials which are evaporated on to the substrate. In the case of thermal evaporation, a resistively heated filament or boat consisting of the metal is used. The boat is typically made of a refractory metal such as W, Mo and Ta with or without a ceramic coating. In this project we have used thermal evaporation for depositing the top electrode (Cr/Au). Similar to e-beam evaporation, thermal evaporation also takes place inside an evacuated chamber. Figure 4.7 the actual instrument used for depositing metals.

Figure 4.7: Thermal Evaporator Used for Fabricating MIM Diodes

In this evaporation technique, the material is heated until melted by means of passing an electrical current through the boat. The evaporated material condenses in the form of a thin film on the substrate surface. Evaporation is a line of sight process, wherein the materials will be deposited only in a straight line; hence the regions that are not accessible from the evaporation source will not be coated. Hence the substrate holder is rotated at a constant speed to get a uniform deposition.

3.3 Alternate Dielectric Deposition Process

The dielectric layer in a solid state MIM diode is typically deposited through sputtering, evaporation, atomic layer deposition, oxidation etc. These techniques require high vacuum conditions and/or high temperature operation to achieve a highly oriented homogenous thin dielectric layer. Recently, another technique used in the polymer industry using an immersion technique is exhibiting great prospects in depositing

monolayers of organic molecule over any solid surface with extreme accuracy. This process of depositing thin films is known as the Langmuir-Blodgett (L-B) technique.

In a L-B process, thin films of organic molecules are built up by a process of successive deposition of individual Langmuir monolayers onto a solid substrate. The monolayer is formed by spreading the organic molecules on the water subphase in a clean L-B trough. The molecules usually have hydrophilic (head) and hydrophobic (tail) parts, so when the film is formed the molecules stand on their heads. Figure 4.8 shows the schematic of L-B deposition process.

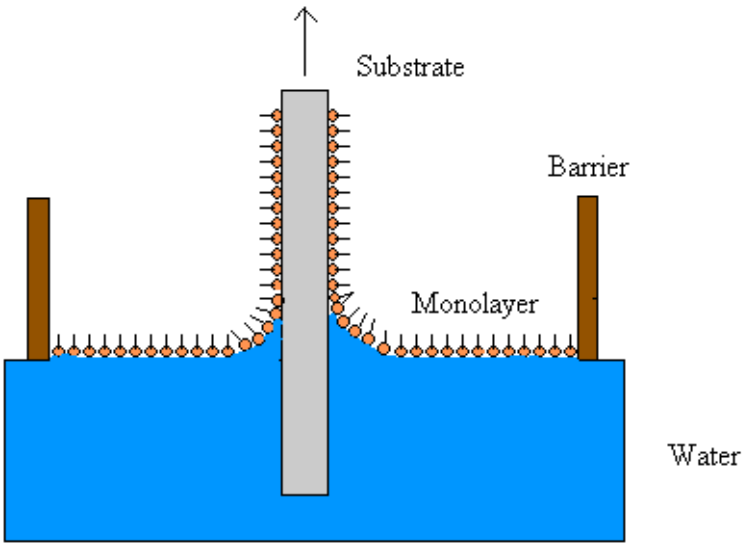

Figure 4.8: Schematic Illustration of L-B Deposition Technique [52]

The solid substrate is raised from the water subphase and the molecules start to adhere to the substrate, which is monitored by recording the change in surface pressure. The surface pressure is usually measured using a Wilhelmy plate [31] and a precision scale. When the molecules first are spread on the water they are very loosely packed and

form a so-called gas phase. This means that the area on the water available for each molecule is rather large and the surface pressure is low. At a certain point the surface pressure starts to rise more rapidly indicating a transition to the liquid phase. As the barrier is moved even further the onset of the solid phase can be noted by an even steeper rise in the surface pressure. One or more monolayers can be transferred to a substrate by dipping the substrate through the monolayer. The monolayer is kept uniform by controlling the surface pressure with the barriers throughout the process. Typical surface area-pressure isotherm showing the different phase is shown in Figure 4.9.

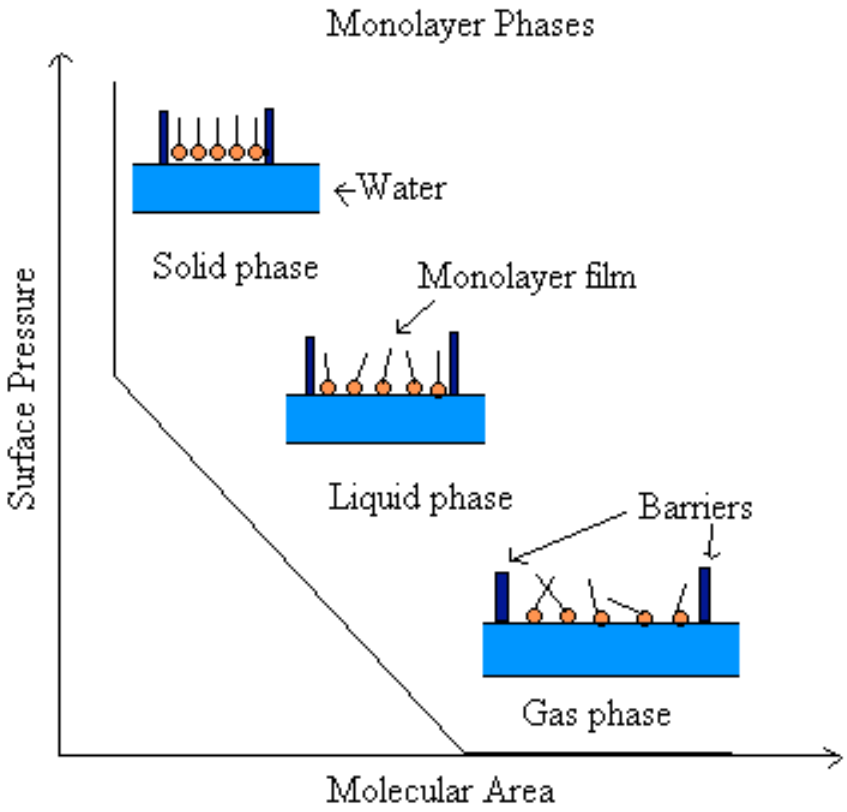

Figure 4.9: Typical Surface Area-Pressure Isotherm Plot of a L-B film [53]

Thus LB-technique is one of the most promising techniques for preparing such thin films as it enables (a) the precise control of the monolayer thickness, (b) homogeneous deposition of the monolayer over large areas and (c) the possibility to make multilayer structures with varying layer composition. An additional advantage of the LB technique is that monolayers can be deposited on almost any kind of solid substrate.

The above-mentioned processing techniques were utilized to fabricate the actual MIM tunnel junctions, described in the next chapter.

CHAPTER 5

DESIGN AND FABRICATION OF MIM DIODES

5.1 Design of MIM Diodes

In this research work, two types of MIM diodes were used. The initial design was a planar, stacked structure, which was designed to prove the concept of the MIM diode. The second design was a stepped layout, which had external bond pads to connect to the probes. Also the diode size was scaled down to accommodate the calibration standards. The diode was designed to be much smaller to operate at high frequencies. Thus, in this section two different designs utilized to fabricate and characterize the MIM diode are presented.

As mentioned earlier, the most important factor to be considered in the design of the MIM diode is the size of the contact area between the metal layers and the insulator layers. The reason for keeping a smaller contact area and the need for a thin layer of insulator were discussed earlier. A MIM device has inherent impedance in its device structure. By lowering the size of the active area, the impedance can be reduced [29].

To validate the concept of the MIM diode, a device operating at a very low frequency was designed. The low frequency operation required the area of the MIM diode to be large (100 μm^2). Upon further verification, with a goal of achieving a reproducible and uniform diode fill factor, a scaled down version with a contact area of

1μm^2 centered around a target frequency of 94 GHz was designed and fabricated. The design of 100 μm^2 (diode A) was a simple planar structure, wherein the layers were stacked upon each other on a silicon substrate. In the case of 1 μm^2 (diode B) a stepped structure with extended contact pads was designed thereby allowing the devices to be probed without damaging the active area. Both diode structure consisted of a thick layer of Ni (100 nm), a thin layer of NiO (~1 -3 nm), and a layer of Cr (30 nm) topped with a thick layer of Au (100 nm).

5.1.1 Stacked MIM Design

As mentioned earlier, a large area diode design was made use of to validate the device concept and for experimenting with different diode parameters. This diode design was developed by Krishnan [54] and the same was utilized for this research work. Figure 5.1 (a) shows the schematic of the initial diode design. The stacked MIM structure design consists of two mask layers. The first level of masking defines the base electrode, which has a very large area (1 mm^2). Over the base electrode, a smaller square structure was defined, which serves as the top electrode or the active area of the MIM diode. The area of the top electrode was defined to be 100 μm^2. This mask was generated from a photo plot sheet, which was transferred to a mask plate using a mask generator. The actual design in the photo sheet was reduced 25X to a glass plate. These plates were then used to generate the final masks by exposing the 4" plate in a step and repeat camera. Figure 5.1 (b) shows the array of diode designs generated in the mask plate.

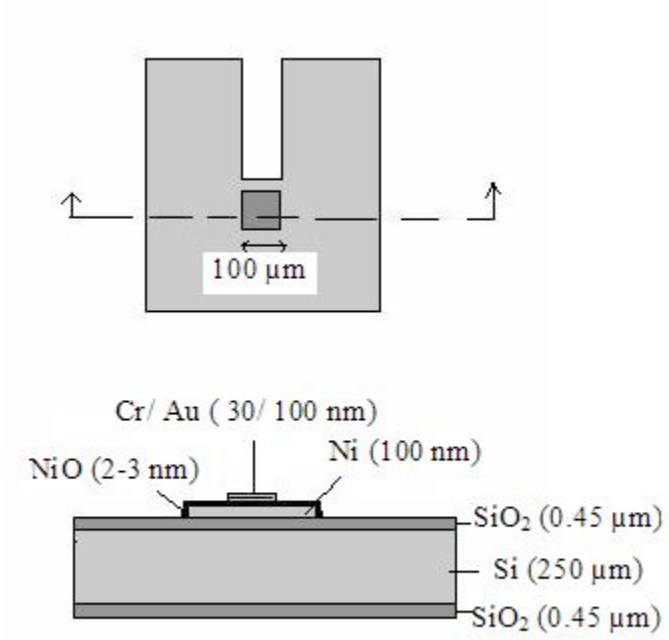

(a)

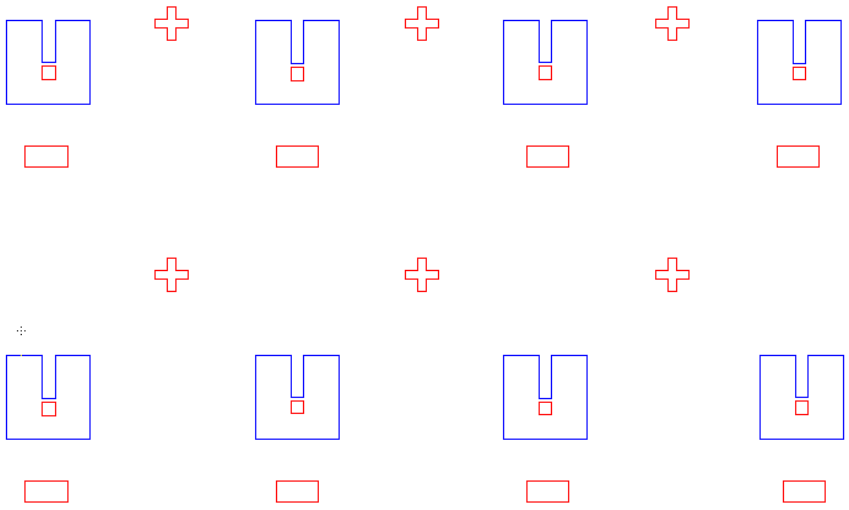

(b)

Figure 5.1: Schematic Representation of (a) Individual MIM Diode Design and (b) Array of Diodes Generated in the Mask Layout.

5.1.2 Stepped MIM Design

The second MIM design was developed with the objective to create a diode suitable for high frequency operation able to detect millimeter wave radiation in the 3mm range. The frequency of interest was 94 GHz for diode operation. For high frequency operation, a co-planar waveguide configuration was chosen. In this design, the antenna-diode detector as well as individual elements were designed to check the device performance. A slot antenna was chosen for this operational frequency with a tunable stub to increase bandwidth. The design of the slot antenna was presented by La Rosa [55] and the same design was used with a diode integrated in its feed line. A schematic of the antenna, diode, and the integrated device is shown in Figure 5.2.

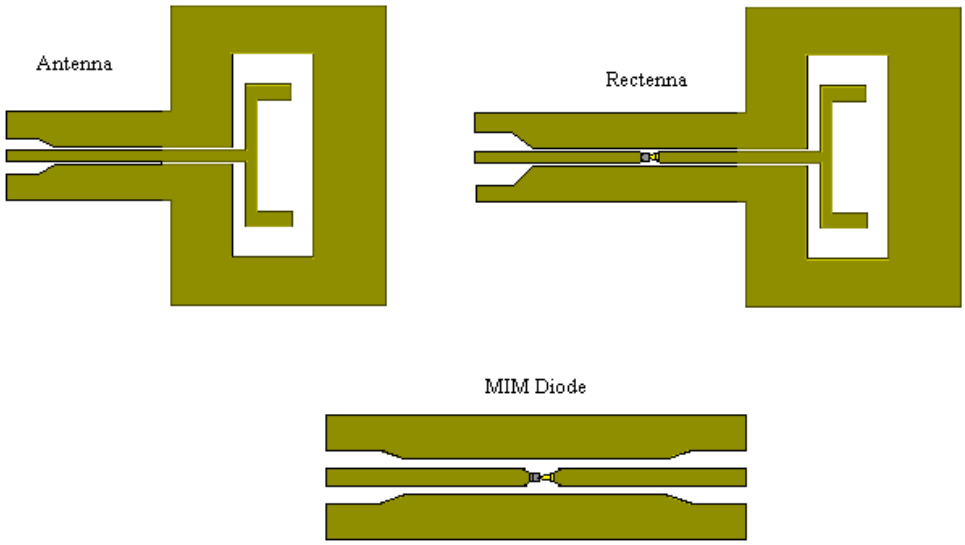

Figure 5.2: Design of Antenna, Diode and Antenna-Coupled Diode

The line-width required for the 94 GHz design was optimized by performing simulations in Agilent's Advanced Design Simulator (ADS) system by La Rosa [55]. Since the junction area of the MIM diode should be as small as possible for good detector performance (small junction capacitance, high cutoff frequency), the overlap between the two metal layers of the diode was designed to be around 1 μm x 1 μm.

Due to high frequency operation, several design consideration have to be taken into account. One of the factors that need to be kept in mind is the substrate thickness. At high frequencies, the likelihood of surface waves propagating through the silicon substrate increases with increased dielectric constant and thickness. Hence, to minimize the power lost as surface waves, the thickness of the substrate has to be kept lower than the wavelength in dielectric (λ_d).

At 94 GHz the dielectric wavelength of silicon is approximately 100μm, which is smaller than the thickness than of commercially available silicon wafers (400 μm and 250 μm). According to Gauthier et. al., [30] the surface wave loss can be minimized by using thin substrates, typically $\lambda_d/10$. For this reason, the mm-wave devices were developed on a 10 μm substrate.

Since the whole substrate will be too fragile if a 10 μm thick silicon substrate was used, a cavity was etched in the bulk silicon under the actual device. The technique used to form a thin silicon membrane is discussed in the next section. In that way, the devices can be connected to the test set-up from the thicker part of the substrate. Due to this criterion, the device design had to be modified to accommodate a thicker as well as thin substrate layout. However, such a modification can cause a mismatch in the input impedance. Hence to maintain a constant input impedance a transition method was

devised [55]. Figure 5.3 shows the typical Co-Planar Waveguide (CPW) line with the transition from thick to thin substrate. The dotted line will be the edge of the membrane. This transition preserves an uniform impedance in the transmission line.

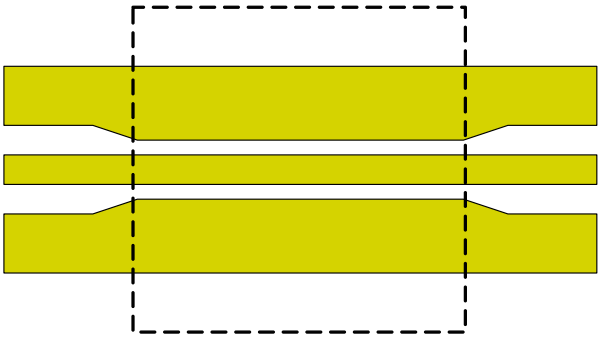

Figure 5.3: CPW Lines Illustrating the Transition from a Thick to Thin Substrate. From [55]

The diode was designed to fit in the CPW design as shown previously. For the diode design, initially the CPW lines, which also act as contact pads, were laid out as the first layer. Then, the bottom electrode of the MIM diode is laid overlapping the contact pad. The area of the bottom electrode was designed to be 25 μm x 25 μm. The next layer is the top electrode, which is designed as a conical structure with a square head connecting to the other end of the contact pad. The top electrode is designed as a conical head to minimize the inductance by a line. The head of the cone defines the active area of the diode, which has an area of 1 μm x 1 μm. A schematic cross section of the diode design is shown in Figure 5.4

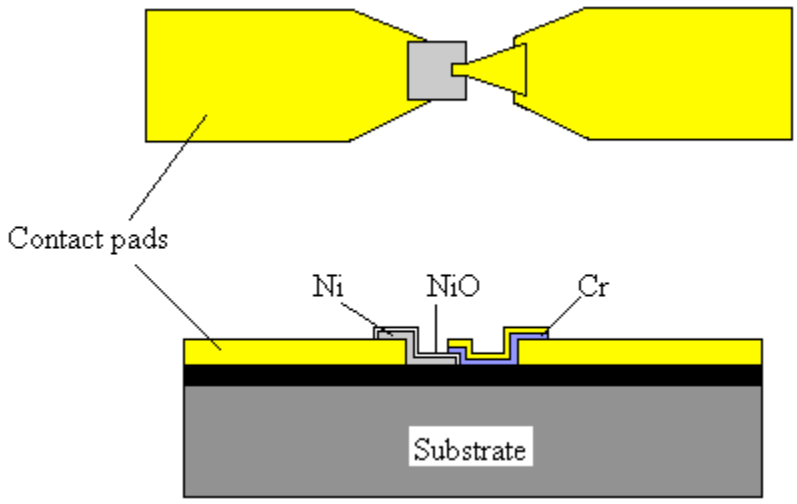

Figure 5.4: Schematic Illustration of the Cross-Section and Top-View of MIM Diode

5.2 Materials Selection

Parallel to the diode design, the materials to be used for fabricating the mm-wave diode had to be selected. Hence various material combinations were fabricated and evaluated. This section discusses the different materials used for developing the MIM diode and the final choice of material combination used for developing reproducible and robust mm-wave detectors is presented.

Material selection is one of most important criteria for manufacturing of a MIM diode. Materials were selected based on the work function of the metal, and dielectric constant of the insulator. By fabricating MIM junctions with different work functions, the asymmetry of the device was improved. And when the dielectric constant of the insulator is low, the capacitance can be lowered, which in turn increases the cut-off frequency. Thus, the MIM diode needs to be fabricated with dissimilar materials. An asymmetric

MIM diode developed with dissimilar metal has better sensitivity and low noise performance. Moreover, asymmetric MIM diodes exhibit nonlinear characteristics even in the unbiased state. Hence, various material combinations were tested for stability, reliability and robustness. The main concerns about selecting the materials were formation of a native oxide layer, adhesion to the substrate and homogenous deposition with minimal roughness. MIM diodes were fabricated with base metals of Aluminum and Nickel and top metals of Chromium, Palladium, and Platinum. The work functions of different metals used for fabricating MIM junctions were given in chapter 3.

Some of the material combinations tried for fabricating the MIM diodes are discussed in this section. Initially Aluminum was used as the base electrode with aluminum oxide as the insulator and Chromium as the top electrode. Although the work function difference was 0.2 eV, the diode exhibited I-V characteristics with slight asymmetry. The thin films were also adhering well to the substrate and the oxide roughness was also very low on the order of 0.5 nm, according to Krishnan [54]. However, the electrical behavior of these diodes was unstable over a period of time. Later using the same base electrode and its native oxide, a MIM diode was fabricated with Pd as the top electrode. Although the work function between Al and Pd is about 0.8 eV, the diodes were unstable and yielded a linear electrical characteristic.

Next, Pt was used as the top electrode, which increased the work function difference to 1.35 eV. However, no measurements could be done as the Pt layer peeled off from the oxide surface. Later, Ni replaced the Pt top electrode. The work function difference between Al and Ni is about 0.8 eV and the electrical behavior of these diodes

was non-linear and very slightly asymmetrical. But these diodes were not stable over a period of time.

Although the Ni and Pd provided a very high work function difference, the devices did not yield any satisfactory diode characteristics at room temperature. This suggests that the oxide formed over the base electrode is getting deteriorated causing device failure. Most likely, if the diodes fabricated with an Al base electrode are stored or packaged, stable diode behavior can be expected. But for this application a diode operating at room temperature is required.

Hence, the bottom electrode had to be replaced with a more stable material, which adheres well to the substrate and also forms a stable oxide layer. Nickel was the next choice because of it's higher work function than Aluminum and the ability to get a native oxide. Since Ni had a work function of 5.15 eV, a material with work function less than Ni was necessary to create an asymmetric barrier. Cr has a work function of 4.5 eV, providing ~0.65 eV different in work function. The dielectric constant of NiO is 11.9, which is comparable to the dielectric constant of Aluminum Oxide (10) [47]. Thus MIM diodes were fabricated with Ni and Cr as the base and top electrode, respectively. MIM diodes fabricated with Ni-NiO-Cr were found to be very stable and the diode characteristics were reproducible over a very long period of time. Hence for fabricating mm-wave detectors, MIM diodes with Ni-NiO-Cr were selected.

5.3 A Typical Fabrication of MIM diode

The fabrication process to manufacture the MIM diode is described in this section. In this section the materials that were used to fabricate MIM diodes, and the fabrication techniques used to attain the MIM diodes are discussed. The other noteworthy techniques involved in the diode development are (a) sputter deposition of the Nickel base electrode, (b) reactive sputtering or plasma oxidation of Nickel Oxide to achieve thin barrier layer with the use of lift-off technique and (c) incorporation of the top electrode or the active area of the MIM diode by e-beam lithography.

5.3.1 Substrate Preparation

The devices were typically fabricated on a 2" <100> silicon substrate. Before using the wafers for further processing, they were first cleaned in acetone and methanol at room temperature, followed by DI water rinse and dried using nitrogen. This is followed by standard wafer cleaning procedure which consist of ammonium hydroxide, hydrogen peroxide and DI water known as standard clean 1 for removing organic contaminants and Hydrochloric acid, hydrogen peroxide and DI water known as standard clean 2 for removing ionic contaminants, each followed by a DI water rinse. The detailed cleaning process describing the times, temperature and mixing ratio is described in Appendix A. Each solution was heated to 80°C and the wafers were immersed and cleaned for 20 mins. Next a layer of silicon dioxide was thermally grown on the substrate to provide an isolation layer for the devices. The oxidation process was performed at 1100°C in a dry-wet-dry oxygen atmosphere to grow an oxide layer approximately 500

nm and 1000 nm thick for the low and high frequency device fabrication, respectively. The thickness of the oxide was measured by an ellipsometer (Rudolph AutoEL III).

5.3.2. Fabrication of Stacked MIM Structure (100 μm^2 Contact Area)

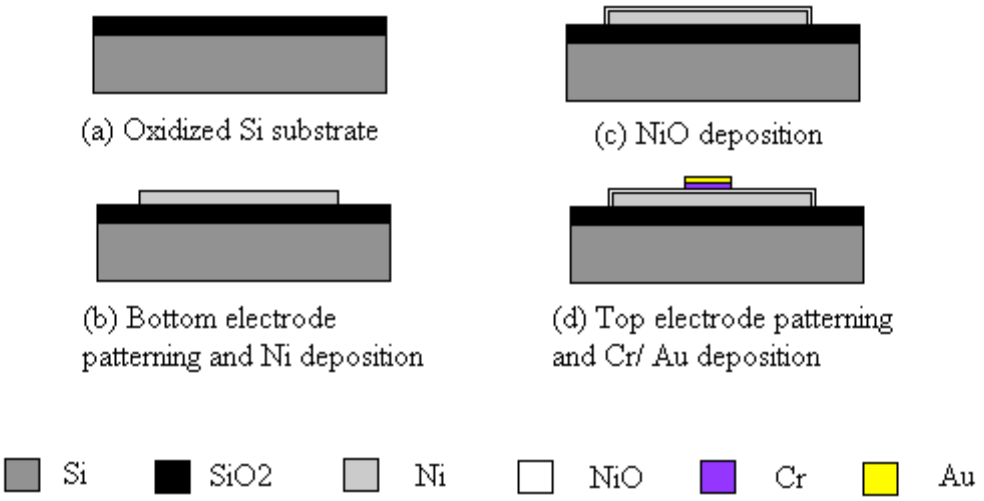

Figure 5.5: Process Flow of Stacked MIM Diode

Figure 5.5 schematically illustrates the fabricating sequence for developing the MIM diode with a 100 μm^2 contact area. Oxidized Si wafers were subjected to photolithography to define the Ni-NiO areas using the first mask. A direct current (DC) magnetron sputtering system, built in-house, was utilized to deposit the bottom electrode (Ni) and the insulator layer (NiO). The patterned substrate is loaded in the sputtering chamber and evacuated to bring it to high vacuum, typically in the 3 μtorr. Nickel was deposited using the DC magnetron sputtering system built in-house. A 3" diameter,

0.250” thick, 99.99% pure Ni target was used as the sputter target. The deposition was typically carried out at a power of 100 W and 10 mTorr Argon pressure. A 100 nm of Ni was deposited by maintaining the gas pressure and DC power. The thickness of the deposited film was determined using a quartz crystal monitor. Later oxygen was bled into the chamber and the deposition was continued. A thin layer (~3 nm) of NiO was deposited in-situ by a plasma oxidation process. Following the metal and oxide deposition, the substrate was immersed in acetone to remove the excess layer and define the bottom electrode and dielectric layer. Some of the resist sticking to edges of the patterns were carefully removed by ultrasonicating the sample for 30 secs.

Then, Ni and NiO coated samples were subjected to the final photolithography step to pattern the Cr layer. Chromium was deposited by using a evaporation technique. Similar to sputtering, the sample was loaded in the chamber and evacuated to a pressure of 2 μTorr. 30 nm of Cr was deposited by thermal evaporation followed by a Au deposition (100 nm) to protect the top electrode. The Cr deposition was made at a very low rate (< 0.1 nm/sec) to obtain a smooth surface. Then, the Au was evaporated at a rate of 0.3 nm/sec at a current varying between 180-200A. The substrate was then subjected to lift-off and the Cr/Au layer was defined to obtain the 100 μm^2 MIM structure.

5.3.3 Fabrication of Step MIM Structure (1 μm^2 Contact Area)

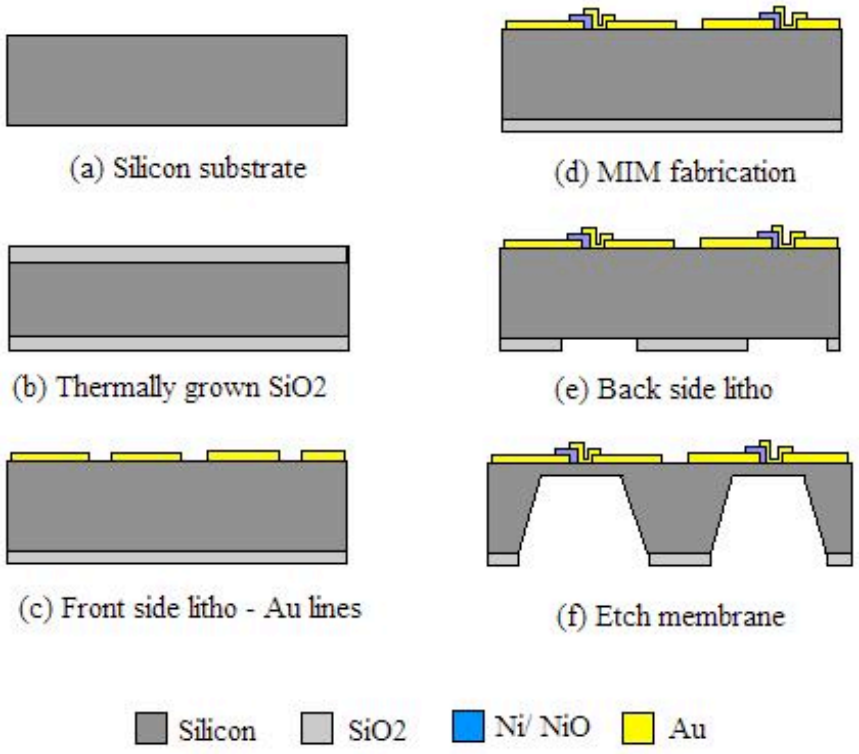

Figure 5.6: Process Flow for Step MIM Diode

Figure 5.6 schematically illustrates the steps involved in fabricating the 1 μm^2 MIM diode. Following the oxidation of the silicon substrate, a photolithography step was performed to pattern the CPW configuration pads along with the antenna and calibration standards. The contact pads were deposited with a thin layer of chromium (Cr) and gold (Au). The metal depositions were carried out using thermal evaporation. A Denton DV-502 thermal evaporator was used for this purpose. Cr was deposited for a thickness of ~ 30 nm which acts as an adhesion layer for the top Au (~200 nm) layer. The Cr deposition

was made at a very low rate (< 0.1 nm/sec) to obtain a smooth surface. Then, the Au was evaporated at a rate of 0.3 nm/sec at a current varying between 180-200A. The contact pads are deposited with higher thickness to minimize surface wave losses during high frequency measurement. For 94 GHz, the skin depth was determined to be ~ 250nm. However a much thicker conductor is preferred. But due to processing incompatibility, the minimal thickness was used. After the contact pads were made, the lithography for the bottom electrode of the MIM diode was done.

The Nickel layer was used as the bottom electrode for the MIM structure. Ni was deposited for a thickness of about ~100 nm. In the case of diode B, all the steps up to Ni and NiO deposition were similar to those for diode A. Only, the final step of e-beam lithography used to define the electrode was different. In particular, for e-beam lithography first a 150 nm thick polymethylmethacrylate (MicroChem 950-K with 3% Anisole) was spun on the sample and baked at 180°C for 2hrs. Later, the devices were patterned by a modified JEOL JSM-840 Scanning Electron Microscope (SEM).

Nabity`s Nanometer Pattern Generation System was used to control the e-beam and pattern the contact area. The patterns were exposed to e-beam for a set area dosage of 110 $\mu c/cm^2$ and a dwell time of 90 μsec to form 1 μm^2 windows. The patterns were developed in a 3:1 Isopropanol: methylisobutylketone solution. After that 30 nm of Cr and 100 nm of Au were deposited to fabricate the MIM diode with 1 μm^2 contact area. Later, photolithography was performed on the backside of the substrate using the EVG backside aligner and windows were opened underneath the devices. Following the lithography step, the top layer was coated with a protective layer of resist-ProtekB2-18

from Brewer Science. This resist can withstand etching against typical silicon etchants such as Potassium Hydroxide (KOH) and Tetramethyl Ammonium Hydroxide (TMAH) for prolonged hours (> 10hrs).

The resist-coated substrates were then placed in a special set-up to etch only the windows on the backside. The etch set-up used to etch the membrane is shown in Figure 5.7. The etch set-up was made using Teflon™ and viton seals. The silicon substrate was kept face down and sealed from underneath to prevent any etchant leak. Then the set-up was immersed in TMAH kept at 80°C. Since we do not have a etch stop layer, the process had to be stopped quite often to determine the etch rate. The etch rate can be determined by calculating the thickness of the substrate before immersing in the Si etchant and the thickness etched in the set time. The thickness etched was determined using a surface profilometer. . After the etching was completed, the substrate was initially rinsed in Isopropyl alcohol to remove the TMAH sticking to the membrane and then rinsed thoroughly with Acetone and methanol to remove the protective layer on the front side. Thus the silicon membrane was formed. Figure 5.8 and Figure 5.9 shows the SEM micrograph and the visual image of the membranes etched in silicon, respectively.

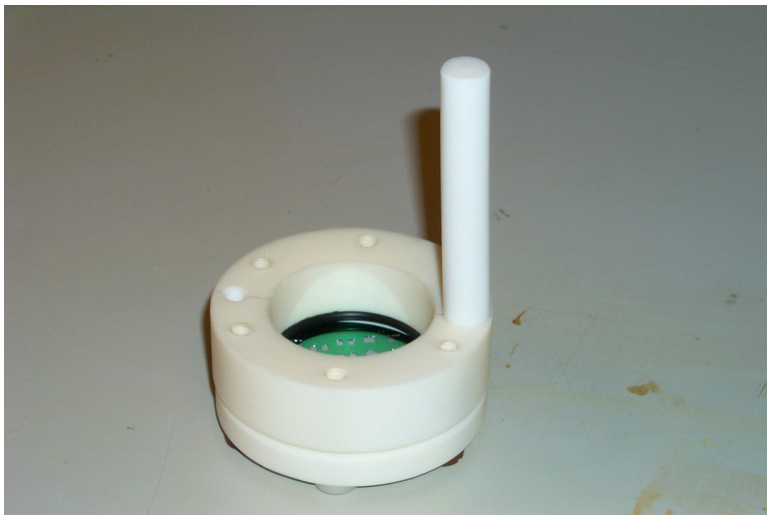

Figure 5.7: Etch Set-up Developed for Silicon Membrane Etching

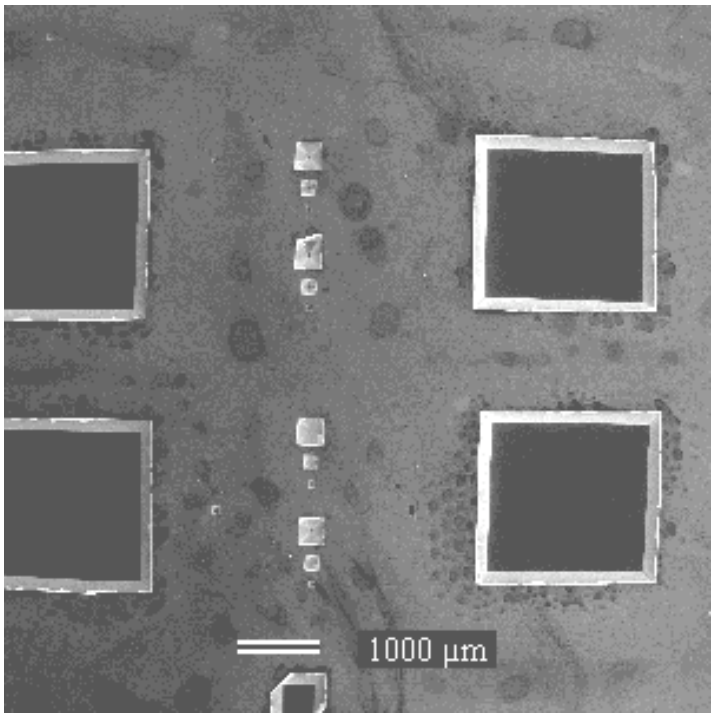

Figure 5.8: SEM Micrograph of Silicon Membranes Etched Using TMAH

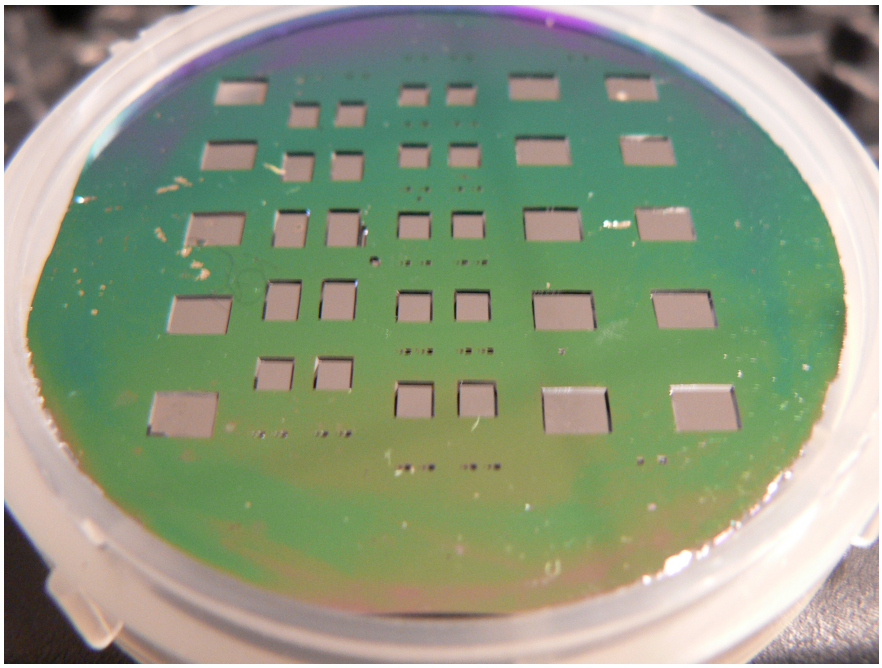

Figure 5.9: Visual Image Showing the Silicon Membranes Etched on a Full Wafer

Figures 5.10(a) and (b) show the corresponding micrograph images of the fabricated 100 μm^2 and 1 μm^2 diodes, respectively. As shown in Figure 5.10(a), the outer square region defines the Ni-NiO region and the smaller square region (Cr/ Au) defines the actual MIM contact area (100 μm^2). Similarly, shown in Figure 5.10(b) is the diode B with gold contact pads underneath the Ni-NiO-Cr/Au structure. The conical head defines the active area of the MIM diode. The area of this diode was observed to be 1.45 μm^2.

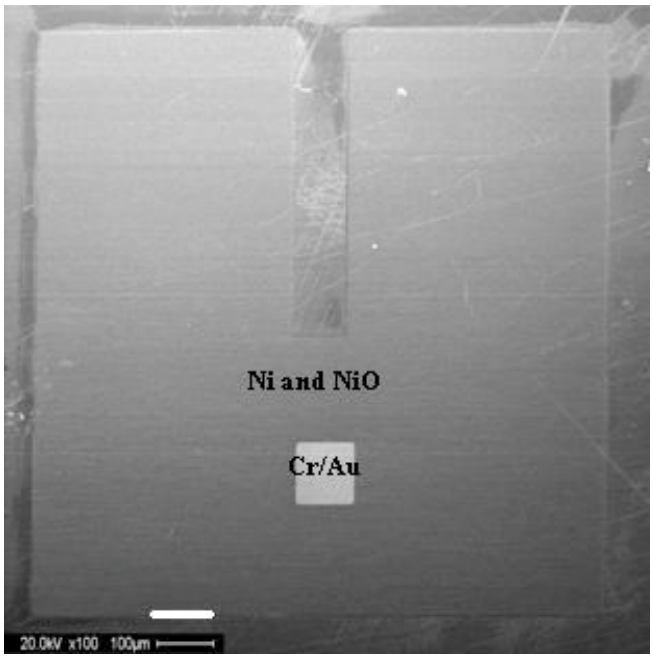

(a)

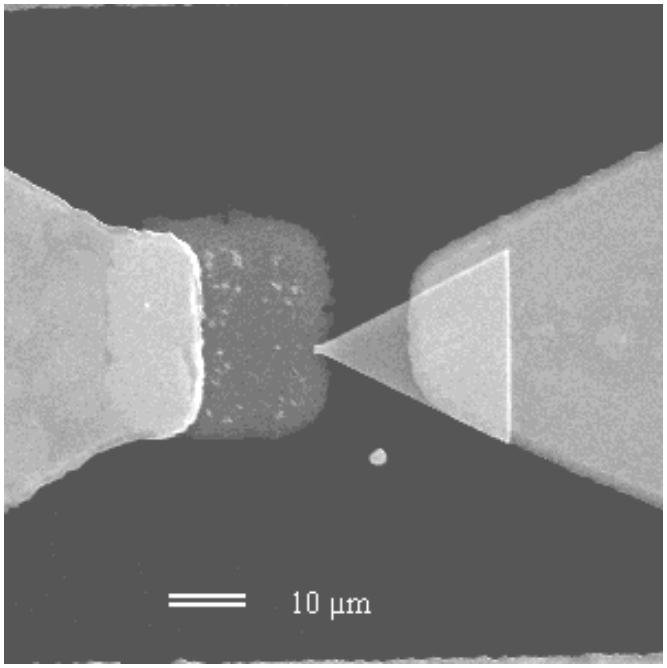

(b)

Figure 5.10: SEM Micrograph of a MIM Diode Fabricated with (a) 100 μm^2 and (b)1 μm^2 Contact Area

5.3.4 Fabrication of MIM with Polyaniline

The fabrication process of the thin film Ni-Polyaniline-Cr/Au MIM diode is schematically illustrated in Figure 5.11. MIM diodes have been fabricated on a 2" bulk silicon substrate with SiO_2 as the insulating layer. These oxidized silicon wafers were used as the substrates. For the fabrication of the polymer based diode 100 μm^2 design was used. The first mask was used to define the Ni and Polyaniline layers and the second mask was used to define the top metal layer (Cr/ Au). The oxidized Si wafers were subjected to photolithography to define the Ni areas. A direct current (DC) magnetron sputtering system, built in-house, was utilized to deposit a 120 nm of bottom electrode (Ni). The thickness of the deposited film was determined using a quartz crystal monitor. Later the P-Ani was deposited on the Ni surface by LB method. Then Ni and P-Ani coated samples were subjected to the final processing step to pattern the Cr layer. A 30 nm of Cr was deposited by thermal evaporation followed by Au deposition (100 nm) to obtain the 100 μm^2 MIM structure.

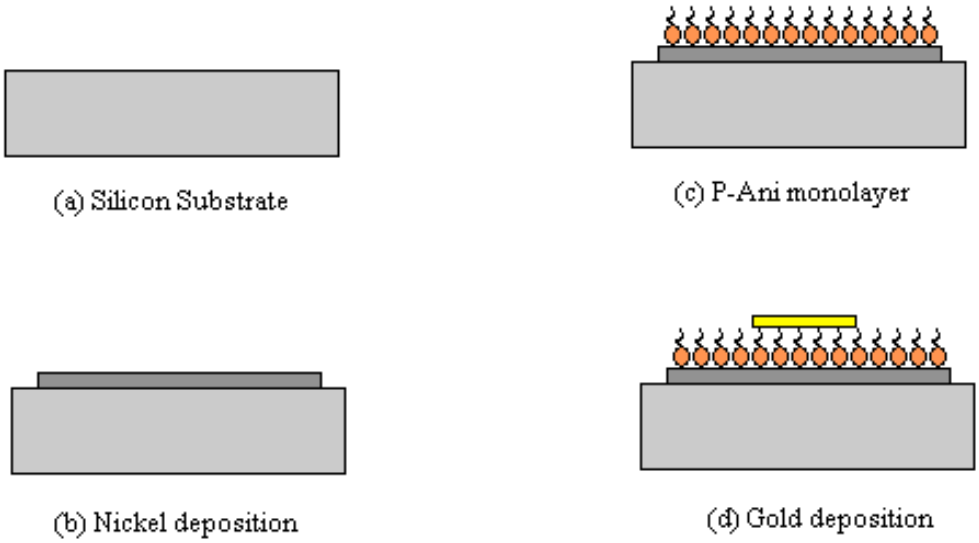

Figure 5.11 MIM-PANI Process Flow

5.4 Dielectric Deposition Technique

5.4.1 Nickel Oxide

As mentioned earlier, in order to achieve tunneling, the dielectric layer needs to be thin (< 5 nm) and homogeneous. Hence, a controlled process to obtain a thin layer of Nickel Oxide was developed. The dielectric layer was deposited through a controlled plasma oxidation process. The same DC magnetron sputtering system used for Ni deposition was also used for depositing the dielectric layer. For the NiO deposition process, O_2 was introduced along with Ar to create a reactive sputtering. NiO was deposited at a very low power of 25 Watts for 10 – 15 mins. During the NiO deposition some of the sputtering parameters were varied to study their effect on thickness and roughness of the film. Two sets of experiments were conducted, (a) by varying the argon

and oxygen gas flow rate and maintaining a constant deposition time and (b) by keeping the gas flow rate constant and varying the deposition time. Under these conditions, the thickness of the deposited film was measured and the optimal parameters were utilized in the actual fabrication of the MIM diode. The thickness was monitored using a quartz crystal monitor and also evaluated by ellipsometry and Atomic Force Microscopy (AFM). The thickness of the dielectric film was found to be in the range of ~ 3-5 nm, assuming the refractive index of NiO to be 2.33 [56]. The dielectric surface was studied and the roughness was estimated by performing tapping mode AFM. Figure 5.12 shows the AFM morphology of NiO. The thin film examined at a scan rate of 1 Hz over an area of 8 μm^2 indicated a surface a roughness of 0.4 -0.6 nm. From the AFM analysis it can be observed that some spikes are present on the film, which might affect the devices if the MIM junctions were fabricated on such regions. The feature sizes of the spike were determined to be varying from 0.5 nm to 3 nm. A possible explanation of these spike formations may be due to the presence of dirt in the underlying film/ substrate. Moreover, the AFM analysis was performed on a test sample, which was more susceptible to the normal environment. If the spikes were present in an actual diode, the junction would be short-circuited, but this scenario was not observed in the fabricated diodes, confirming the presence of a defect free barrier layer.

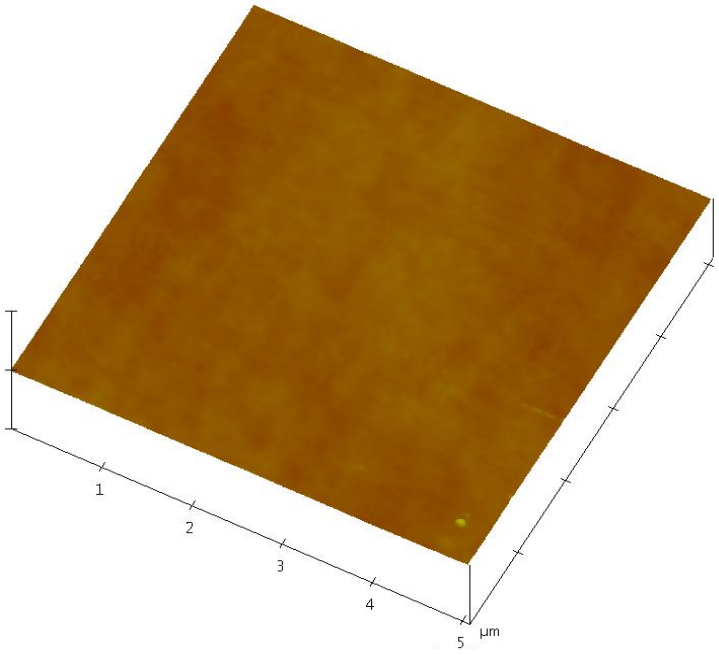

Figure 5.12 AFM Micrograph of a Silicon Substrate Deposited with NiO

Table 5.1 shows the thickness of the insulator layer deposited under various conditions. The insulator was deposited for 10 – 15 mins with varying gas flows of Ar and O_2 with 1:1 and 2:1 gas ratio. From Table 5.1 it is observed that for a 10 mins deposition time with 1:1 gas ratio, the thickness and the roughness of the insulator were very high. Similar results were observed with 2:1 gas ratio for the same time (10 mins). When the deposition time was increased to 15 mins, the thickness of the films was increased and the surface roughness was reduced. As suggested by Chapman [51], during the sputtering process, the material arriving at the substrate will be in atomic or molecular form. These atoms begin to nucleate forming islands of atoms, at which point the thickness and the roughness of the films will be comparable. But over a period of time, these atoms coalesce to form a thin layer of film with uniform thickness and less surface roughness.

For the fabrication of the MIM diode, NiO was deposited under 2:1 Ar – O_2 gas ratio for 15 mins.

Table 5.1: Gas Ratio vs. Roughness and Thickness Estimate of the Dielectric Layer

Gas Ratio Ar: O_2	*AFM roughness*	*Ellipsometry thickness*
1:1 (10 mins)	20.0Å	24 to 30Å
1:1 (15 mins)	8.0Å	28 to 30Å
2:1 (10 mins)	16.0Å	15 to 22Å
2:1 (15 mins)	4.0 to 6.0Å	20 to 24Å

The thickness of the NiO layer was also verified from a cross-sectional SEM analysis of the MIM diode. It was convenient and accurate to estimate the NiO thickness when Au was used as the top electrode instead of Cr. Figure 5.13 shows the cross-sectional SEM image of the MIM diode with a thin, homogenous layer (~5.5 nm) of Nickel Oxide.

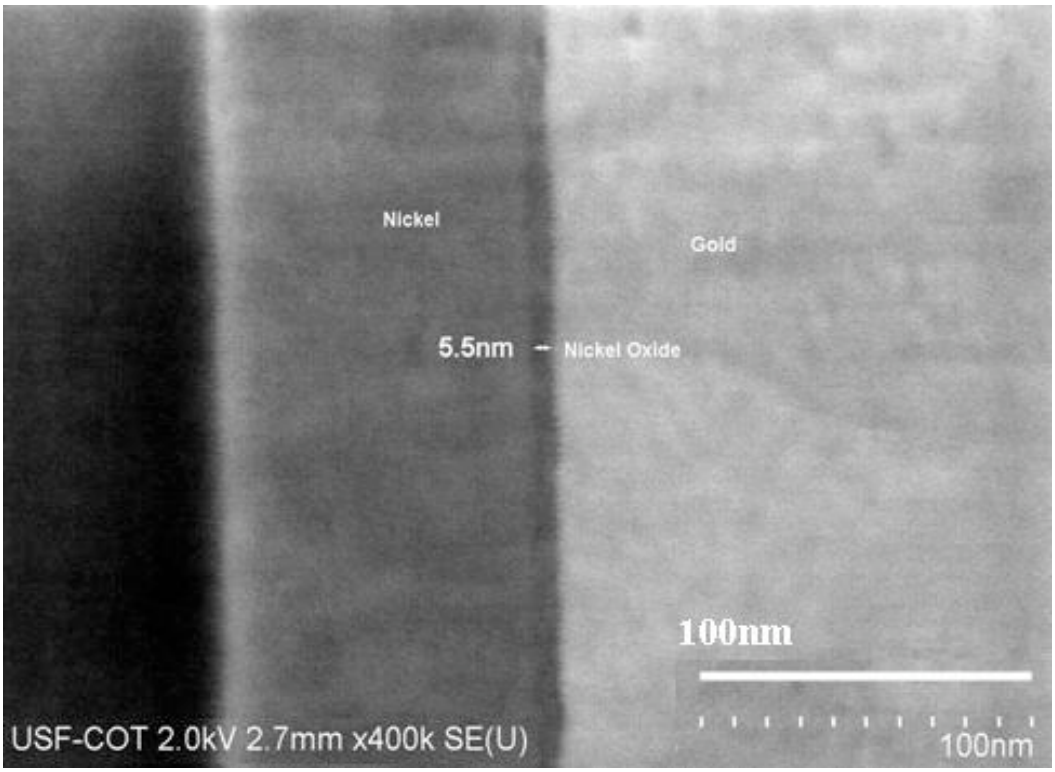

Figure 5.13: SEM Micrograph Showing the Cross-Section of a MIM Diode

5.4.2 Polyaniline

Polyaniline with 50K mol. wt. was obtained from Sigma-Aldrich. Polyaniline was dissolved N-methyl 2-pyrrolidinone (NMP) containing 60% $CHCl_3$. The dissolved mixture containing 0.8 mg/ml of P-Ani was taken in a microlitre syringe and kept ready. The LB film deposition was done using NIMA Technology's LB trough (model 611D) shown in Figure 5.14.

Figure 5.14: Visual of the L-B Trough Used for Polyaniline Deposition. From [57]

This deposition process requires an ultimate clean trough, since any dust particle present in the surface may cause a change in pressure. Hence the trough was thoroughly cleaned with $CHCl_3$ and dried with N_2. The trough was checked for any unevenness on the surface due to presence of impurities by filling the trough with Millipore DI water. The pH of the DI water was maintained at 7 by the MilliQ™ system. The surface pressure is measured by the Wilhelmy plate-method. In this method a measurement is made by determining the force due to surface tension on a plate suspended so that it is partially immersed in the subphase (see Figure 5.15). This force is then converted into surface tension (mN/m or dynes/cm) with the help of the dimensions of the plate. The Wilhelmy plate is hung from a Langmuir film balance to measure the surface pressure and barriers for the available surface area.

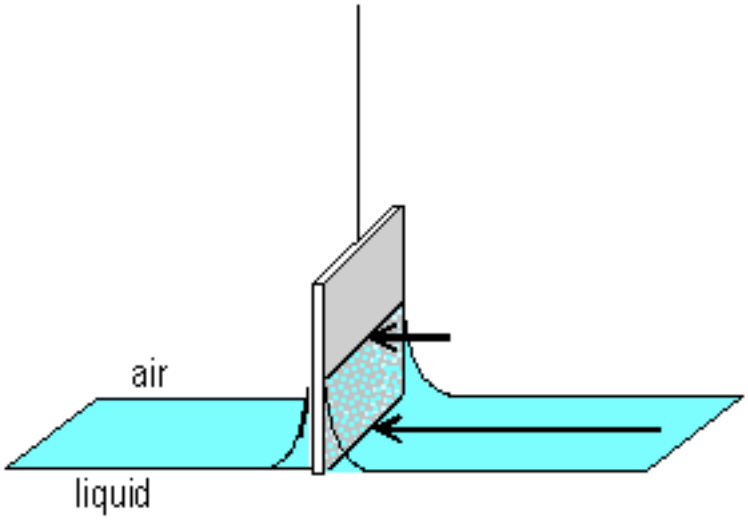

Figure 5.15: Schematic of a Wilhelmy Plate Balanced in a Langmuir Trough. From [31]

After establishing a clean surface, the Ni coated substrate was immersed in the LB trough using a computer-controlled dipper. A barrier scale used to compress the organic layer was pulled back and polyaniline was introduced in the trough. Later, the dissolved P-Ani mix was introduced over the DI water surface, while observing the change in pressure through the Wilhelmy plate and balance. After reaching a constant pressure isotherm, the barrier is closed. The pressure area isotherms of the polyaniline monolayer were performed at a barrier compression speed of 10 cm^2/min at room temperature. Then the dipper was slowly pulled out at a rate of 2 mm/min to deposit a monolayer of polyaniline. The pressure-area isotherm obtained while coating the Ni sample with polyaniline is shown in Figure 5.16.

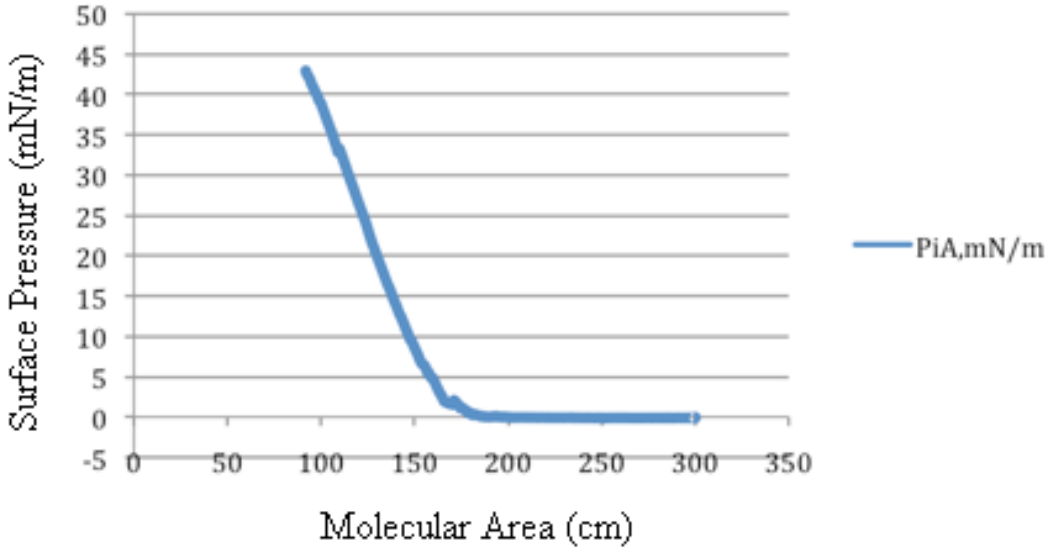

Figure 5.16 Pressure-Area Isotherm of PANI

The pressure area isotherm plot shows the various phases of the polyaniline layer as it gets transferred to the Ni film. When the barrier is compressed, more polyaniline layer is forced into a smaller surface area and when the sample is lifted, the polymer layer sticks to the surface. The base flat line shows the liquid phase of the polymer layer which transforms to a solid phase as observed from the knee of the plot. Thus a monolayer of polyaniline is coated on the Nickel layer forming an ultra-thin dielectric for the hybrid MIM diode.

5.5 Comments on Fabrication Procedure

(a) Step Coverage:

The contact area of the MIM diodes was designed to be 1 μm^2 to operate at 94 GHz. This active area of the device was fabricated using e-beam lithography, since a high-resolution optical lithography tool was not available. Thus for developing the 1 μm^2 diode, optical as well as e-beam lithography process had to be utilized. As mentioned in the processing sequence, the contact pads and the bottom electrodes were fabricated using optical lithography, while the top electrode was fabricated using e-beam lithography. In the e-beam lithography process, PMMA was used as the photoresist. PMMA, when dispensed on the wafer yields a very thin layer in the range of 150 nm. This restricts the metal deposition to 70 – 100 nm. This would cause a potential sidewall coverage issue.

By increasing the thickness of the e-beam resist the step-coverage issue in the diode can be minimized. Adding another layer of e-beam resist called the bilayer PMMA (PMMA-Co-MAA) will increase the thickness of the overall resist layer [26]. The additional layer of polymer provides extra thickness of about 500 nm, allowing us to deposit a thicker top electrode and also provides an undercut during the e-beam litho process, facilitating the lift-off process.

(b) Contact Area Alignment:

Another issue with e-beam lithography was the difficulty in aligning the top electrode to define exactly 1 μm^2 by intersecting the bottom electrode. Since no

alignment markers were made for the e-beam litho process, all the diodes had to be individually patterned. This gives more room for error since every diode has to be manually aligned. A virtual alignment mark, which can be enabled in the JEOL SEM, was used to ballpark the starting point of the design. Hence the contact area of the diode might not be exactly 1 μm^2 as expected. This would affect the operational frequency of the diode.

(c) Silicon Membrane Etch:

The MIM diodes fabricated for MMW measurements were developed on a silicon membrane. The ideal thickness to minimize surface wave loss was determined to be 10 μm. This was accomplished by etching the silicon substrate by performing a wet-chemistry process as described earlier. A timed-etch procedure was carried out by determining the initial thickness of the substrate and the etch rate of the silicon etchant. However, as the etching process begins, the reactivity of the etchant decreases, causing a slower etch rate. Hence, a close watch had to be kept during the entire etching process to maintain the etch rate by adding newer solution or by determining the extra time the etch process would take. Additionally, since the silicon substrate has a native curvature, the etched profile would also display the same trend. Figure 5.17 shows the variation in membrane thickness obtained after performing silicon etching.

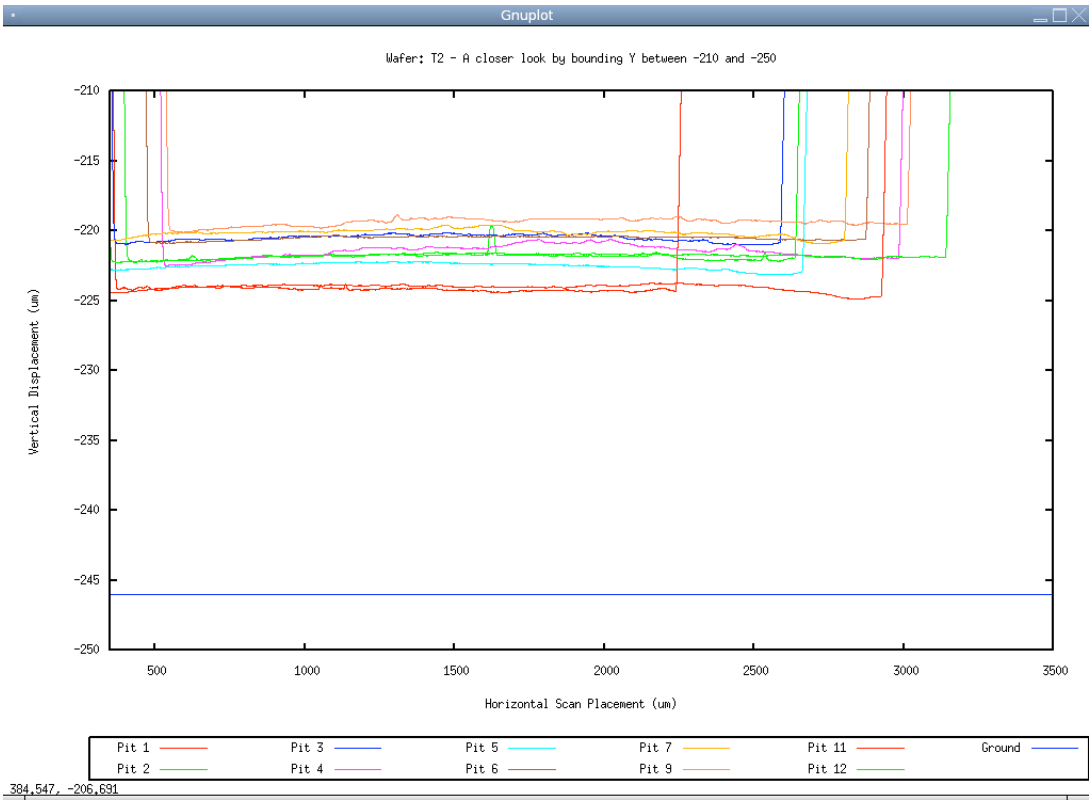

Figure 5.17: Profilometer Plot Illustrating the Non-Uniformity in Etch Profiles

In summary, MIM diodes were designed with two different contact areas (100 μm^2 and 1 μm^2). Ni-NiO-Cr was used as the material combination for developing these diodes. The fabrication methodologies were identified and the diodes were fabricated with optical and e-beam lithography. Finally, an alternate method to deposit a thin layer of polymer was also identified and the MIM diodes were fabricated with a polymer insulator. In addition, some of the key problem areas were also identified which might affect the device performance.

CHAPTER 6

RESULTS - DC MEASUREMENTS

6.1 Experimental I-V Characteristics of MIM Diode

The dc I-V characteristics of the fabricated MIM diodes were measured at room temperature using a HP4145B semiconductor parametric analyzer connected in series with a probe station (Cascade Micromanipulator). The diodes were probed using titanium coated probe tips with 1 μm diameter. The measurement unit was connected to a PC via a General Purpose Interface Board (GPIB) and the data points were recorded using Metrics Inc., Interactive Characterization Software. The dc characteristics of the diodes were measured under a two-terminal arrangements; the measurements being taken in the forward and reverse-bias conditions. The I-V behavior of the diodes was obtained by applying voltages from –0.5 V to +0.5 V. The experiments were limited to these voltages since higher bias voltages could result in dielectric breakdown of the insulator layer.

6.1.1 I-V Characteristics of MIM Diode with 100 μm^2 Contact Area

A typical I-V curve of Ni-NiO-Cr MIM diode fabricated with 100 μm^2 contact area is shown in Figure 6.1. The MIM diodes exhibited non-linear and asymmetric behavior at 0.5 V of applied bias. At very low voltages (< 0.2 V) the diode exhibits

linear response, since the current is proportional to the applied bias. But, beyond this initial voltage (V > 0.2 V), a non-linear response is obtained. The MIM junctions exhibited current in the range of -9 μA to 11 μA when a bias voltage was swept from -0.5 V to +0.5 V. The resistance exhibited by these diodes was typically in the range of hundred kΩ. Figure 6.2 shows the distribution of zero-bias resistance of all the diodes. The I-V characteristics of different diodes fabricated in this research are shown in Appendix C.

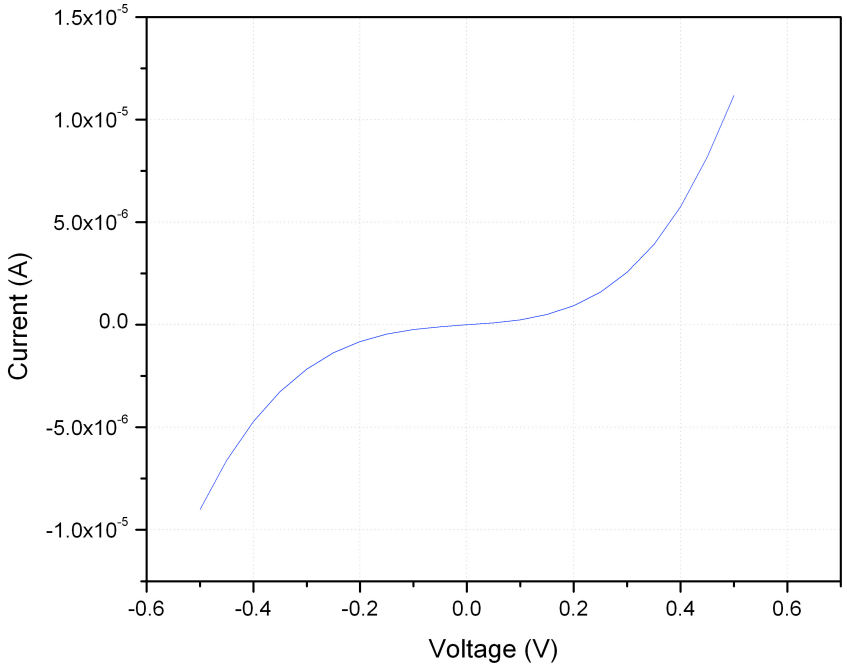

Figure 6.1: Typical I-V Characteristics of MIM Diode with 100 μm^2 Contact Area

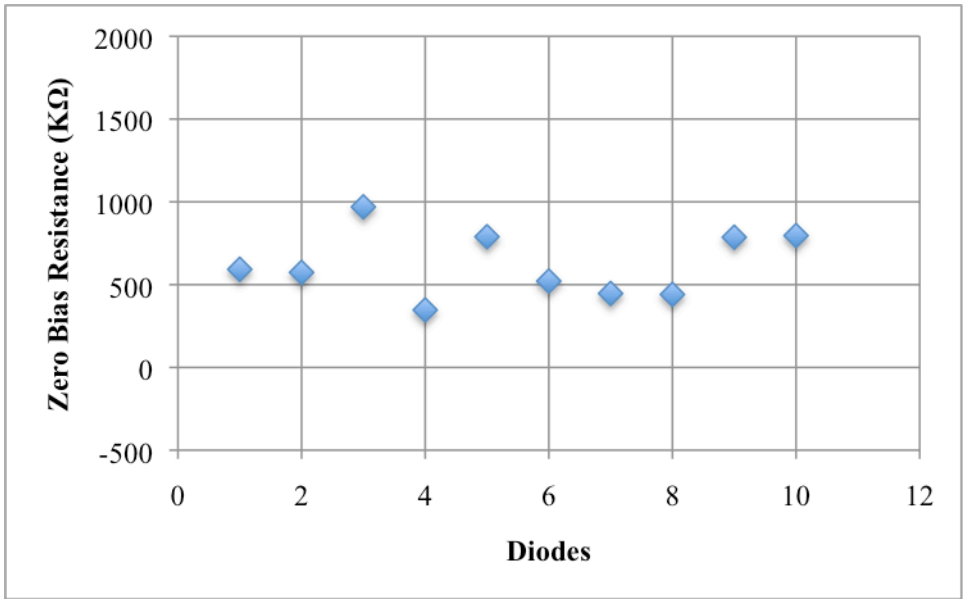

Figure 6.2: Distribution of Zero Bias Resistance of 100 μm^2 MIM Diode

The performance of the diode is characterized by its current sensitivity and detectivity. Maximum sensitivity is obtained at a DC bias point where maximum curvature of the I-V characteristics occurs [4]. The sensitivity was obtained from the I-V plot by obtaining the first and second derivatives and then taking the ratio of the second to the first, as given by

$$S = \frac{I''(V)}{I'(V)} \tag{6.1}$$

Where,

$$I''(v) = \frac{d^2 I}{dv^2} \tag{6.2}$$

And,

$$I'(v) = \frac{dI}{dv} \tag{6.3}$$

The first derivative of the I-V plot shows the measure of rate of change of conductance with applied voltage, and provides a useful way of comparing the forward and reverse characteristics. The second derivative of the I-V plot shows the non-linearity of the diode. The ratio of second derivative to the first derivative obtained from the I-V plot gives the sensitivity of the diode, which characterizes the diode performance. Figure 6.3 shows the first derivative or the rate of conductance obtained from the I-V characteristics of the MIM diode.

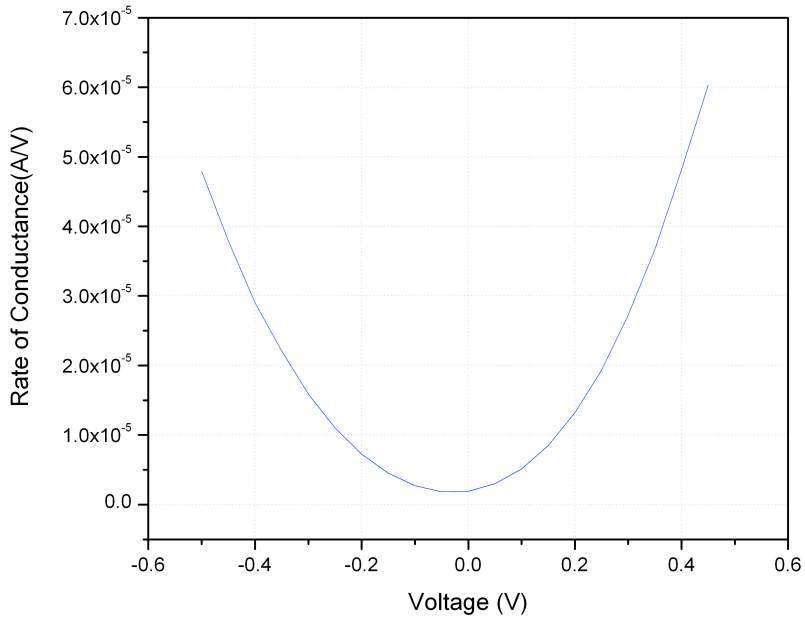

Figure 6.3: Rate of Conductance of MIM Diode with 100 μm^2 Contact Area

The asymmetry in the I-V plot is more pronounced in the rate of conductance vs. voltage plot, showing the existence of a difference in work function between the metal electrodes. The difference in work function between Ni and Cr is around 0.65 eV. Even though this difference is not large, asymmetrical and non-linear behavior was demonstrated. Figure 6.4 shows the sensitivity of the diode. The peak sensitivity was around $15V^{-1}$, which is the highest obtained value for a room temperature measurement. The distribution of the peak sensitivity obtained for the 100 μm^2 MIM diodes are displayed in Figure 6.5. The sensitivity of 10 different diodes on the same substrate was calculated from its corresponding I-V characteristics. It can be observed that the sensitivity of all the diodes has been consistent throughout the substrate demonstrating a fair level of uniformity.

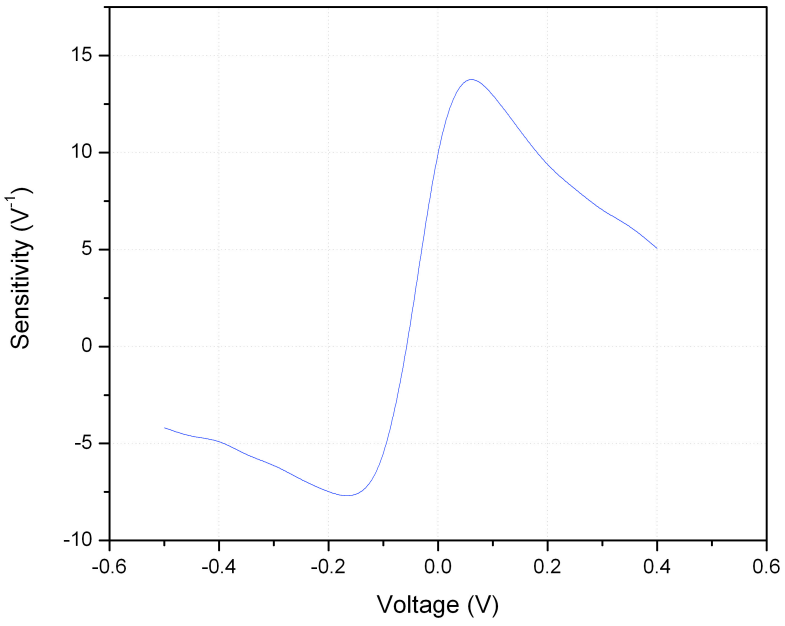

Figure 6.4: Sensitivity of MIM Diode with 100 μm^2 Contact Area

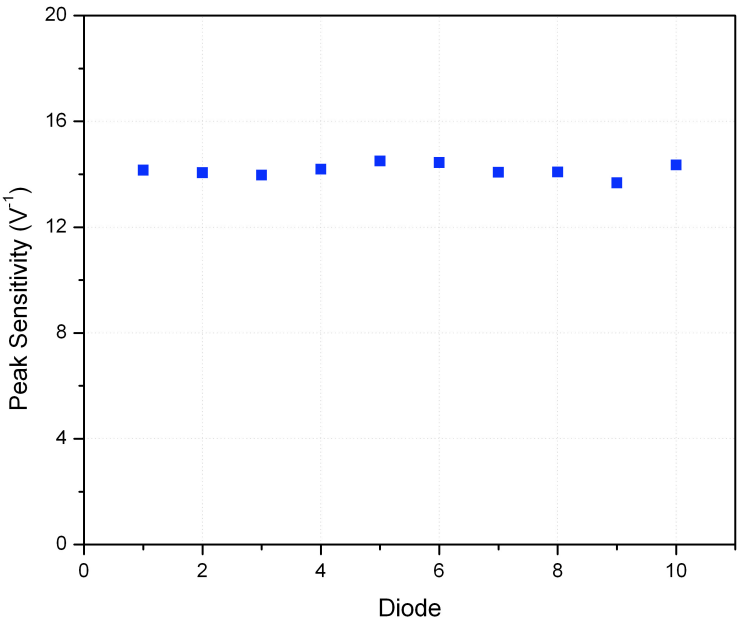

Figure 6.5: Distribution of the Peak Sensitivity for 100 μm^2 MIM Diodes

6.1.2 I-V Characteristics of MIM with 1 μm^2 Contact Area

Following the measurement of 100 μm^2 diode, the I-V characteristics of 1 μm^2 diode was measured using the same test set-up. The voltage was swept from -0.5V to -0.5V and the corresponding current was recorded. I-V characteristics of a typical MIM diode with 1 μm^2 contact area are shown in Figure 6.6. The forward and reverse currents were in the range of -2.5 μA to 3 μA. From Figure 6.6 it is observed that the diode exhibited a minimal asymmetry. The zero bias resistance of the diodes was determined to be in the range of few hundred kΩ. Figure 6.7 shows the distribution of zero bias resistance throughout the wafer. The I-V characteristics of all the 1 μm^2 MIM diodes measured is shown in Appendix C.

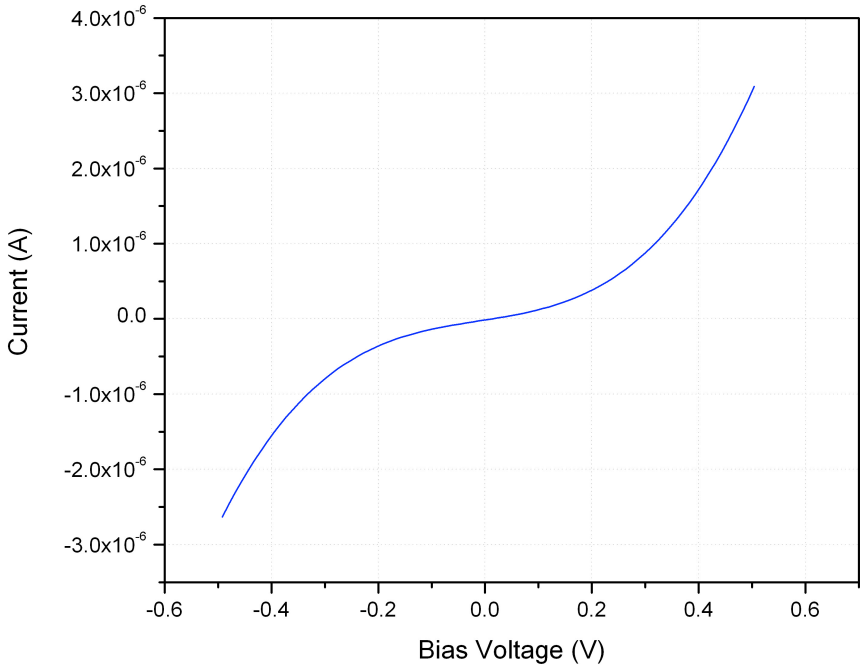

Figure 6.6: Typical I-V Characteristics of MIM Diode with 1 μm^2 Contact Area

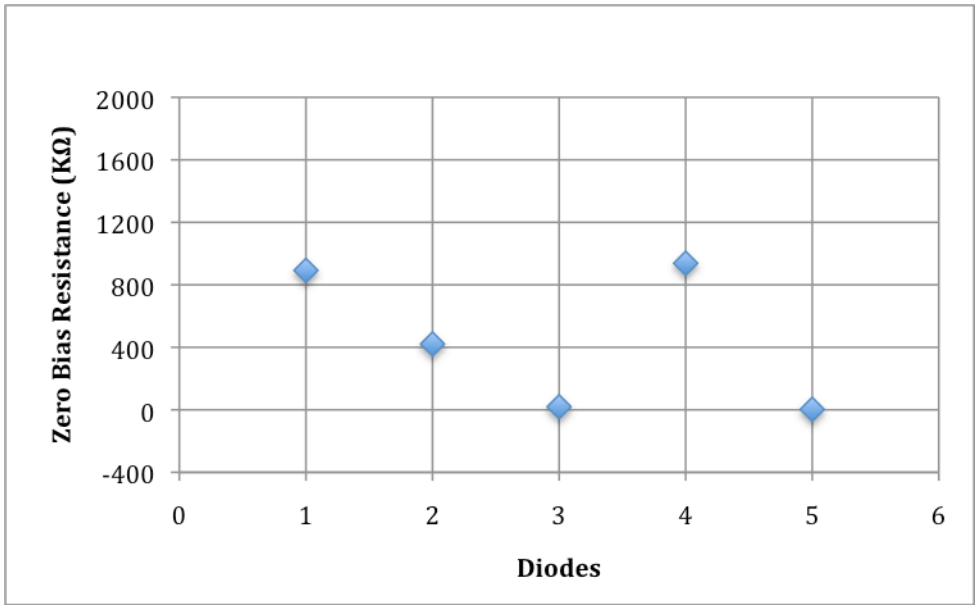

Figure 6.7: Distribution of Zero Bias Resistance of 1 μm^2 MIM Diode

Although the I-V plot exhibits a minimal asymmetry in the device, the actual asymmetry of the diode can be better observed from the first derivate plot of the I-V behavior. Figure 6.8 shows the rate of conductance plot of a typical MIM diode. This demonstrates the difference in the forward and reverse bias region of the diode.

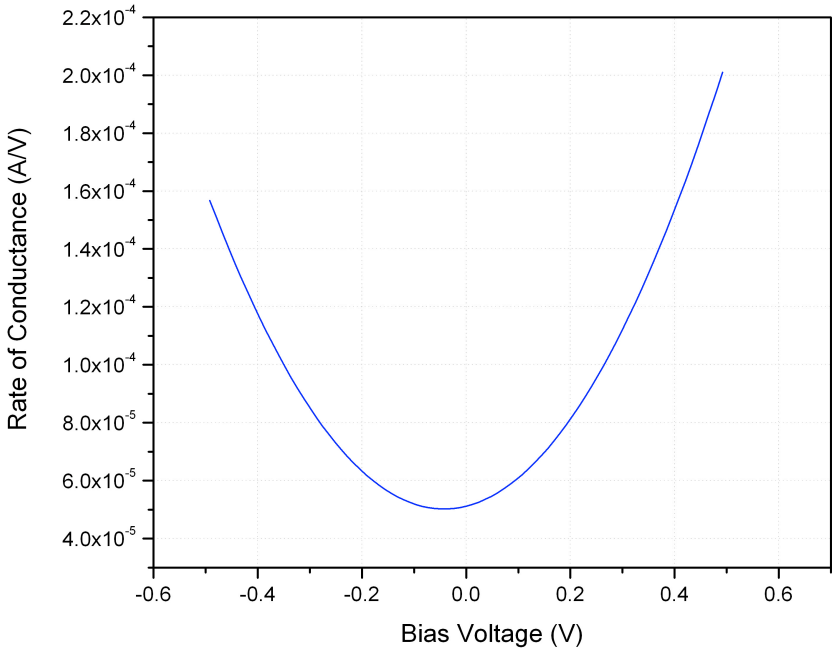

Figure 6.8: Rate of Conductance of MIM Diode with 1 μm^2 Contact Area

Additionally, the sensitivity of the diode was determined by finding the ratio of the second derivative and first derivative of the I-V characteristics. The diodes exhibited a maximum sensitivity value of 7 V^{-1} as shown in Figure 6.9. The sensitivity of all the diode fabricated was determined to show the distribution. Figure 6.10 shows the distribution of diode sensitivity through the substrate. The sensitivity values were found to be varying from 7 to 3.5 V^{-1}.

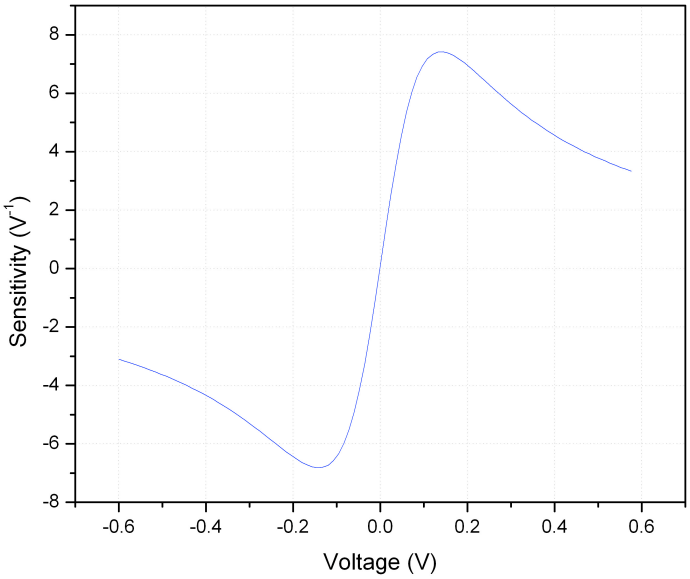

Figure 6.9: Sensitivity of 1 µm^2 MIM diode

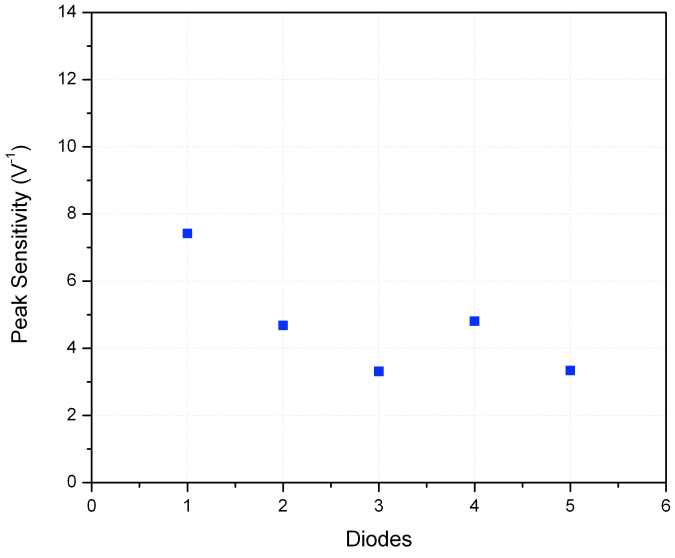

Figure 6.10: Distribution of Peak Sensitivity Obtained for 1 µm^2 MIM Diodes

6.1.3 I-V Characteristics of Polymer MIM Diode:

After establishing the electrical characteristics of MIM diodes with Ni-NiO-Cr, MIM diodes fabricated with Ni-PANI-Cr were investigated. In this section, the I-V characteristics of MIM diode fabricated with Ni-PANI-Cr is presented. These diodes were fabricated with a 100 μm^2 contact area. The I-V characteristics of a polyaniline based MIM diode is shown in Figure 6.11.

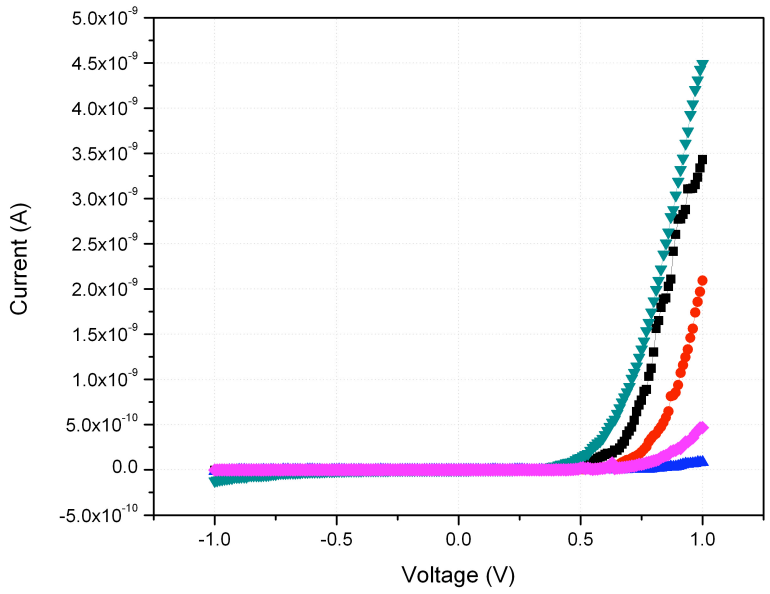

Figure 6.11: I-V Characteristics of MIM Diode with Polyaniline Insulator

The diode exhibited highly non-linear and asymmetric I-V characteristics at applied bias of 1 V. Although the diodes exhibited very small forward current (in the order of nA), the reverse bias current was very negligible. The forward current at +1 V is ~4.5 nA, and the reverse current at -1 V is in the pA range. Similar to the Ni-NiO-Cr

diodes, the polyaniline-based diodes also exhibited very low current in low voltages. When the bias voltage was increased above 0.2 V the output current increased. However, this increase was not comparable to the Ni-NiO-Cr diodes. The resistance of these diodes was very high (unlike the solid-state diodes discussed earlier); typically in the range of a few hundred MΩ.

Typically the resistance of the diode increases when the thickness of the dielectric increases, thereby reducing the probability of electron tunneling. The thickness of the polyaniline deposited in this fabrication process is estimated to be 2 to 3 monolayers. However, the thickness of the polyaniline could not be measured. From the I-V data of the diode it can be stated that, either the diode has a thick insulator layer sandwiched between the metal electrodes or the barrier height formed by the Ni-Polyaniline interface is high. When compared with the NiO-based MIM junction, this diode exhibits better asymmetry suited for detector applications. However, the resistance is higher than the NiO tunnel junctions making it less suitable for any application. Hence the barrier layer needs to be investigated to achieve better diode characteristics.

A noteworthy point to mention is that the polyaniline was deposited using the previously mention L-B process, after which it was subjected to other harsh chemicals and a photolithography process for defining the top electrode. Hence, the polymer layer might have degraded resulting in the high resistance I-V characteristics. Additionally, the polyaniline was deposited on Ni surface, which tends to form a native oxide upon exposure to air. This could have caused a Nickel Oxide formation thus creating a dual barrier. This native oxide formation could contribute to the increase in dielectric

thickness, thereby reducing the tunneling current. Therefore, to achieve better diode characteristics with polyaniline insulator, the diode processing should also be done with minimal chemical exposure and the polyaniline should be carried out in an inert atmosphere to avoid native oxide formation.

6.2 Theoretical DC I-V Characteristics

The tunneling equation given in chapter 3 was used to compare the actual device data. To do this it was necessary to determine the parameters s, ϕ_1, and $\Delta\phi$. The value of $\Delta\phi$ can be determined from the difference in workfunction of the metals, Ni and Cr. Thus $\Delta\phi$ is determined to be 0.65 eV. The thickness of the insulator layer was determined to be 3 nm from the ellipsometry measurements. Finally, the barrier height ϕ_1 is related to the workfunction of metal 1 and the activation energy of NiO as described in Eq. 3.1. The activation energy of NiO is approximately 0.6 eV [58]. Thus the barrier height ϕ_1 is determined as, ϕ_1=5.15-0.6 = 4.5 eV.

Using these parameters, the theoretical I-V curve was determined. Figure 6.12 shows the I-V curve for Ni-NiO-Cr diode with dielectric thickness as 3 nm, ϕ_1 as 4.5 eV and $\Delta\phi$ as 0.65eV. It is observed that the theoretical curve is largely asymmetric and non-linear with current in the range of pA. Hence exhibiting a huge resistance in the order of hundreds of GΩ.

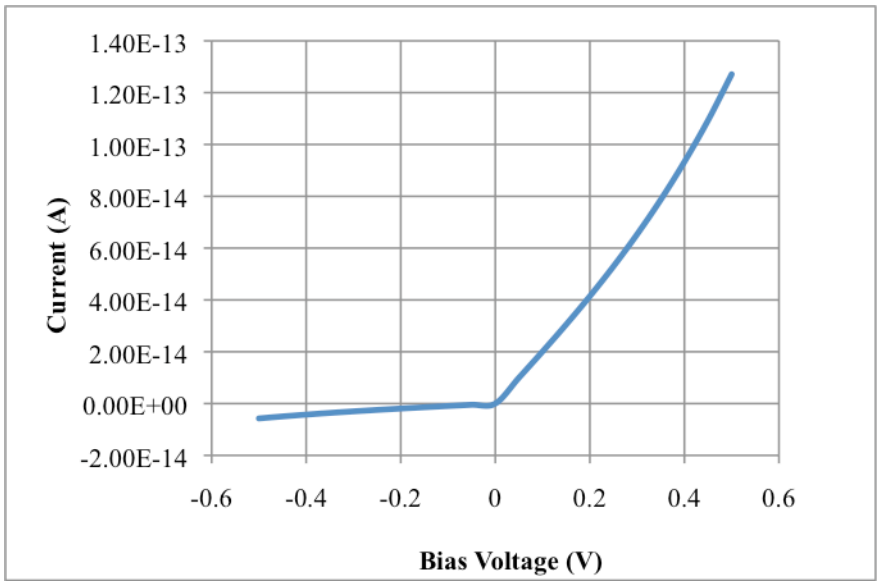

Figure 6.12: Theoretical I-V Curve for s= 3 nm, ϕ_1 = 4.5eV and $\Delta\phi$ = 0.65eV

Although the barrier height was determined as 4.5eV from the equation, that may not be the case when considering the actual barrier height between the metal 1 and interface. Hence for a barrier height of 4.5 eV and thickness of 3 nm, the probability of electron tunneling will be low, yielding lower current as demonstrated by the theoretical plot. But the current obtained by the fabricated diodes is higher than the theoretical value for the same dielectric thickness. Hence the barrier height has to be changed to match the experimental value.

Typical barrier heights reported in the literature for Ni-NiO interface were usually 0.2 eV to 1 eV [59]. So the theoretical tunnel equation was calculated using these barrier height values. Figure 6.13 shows the theoretical curve plotted using ϕ_1 as 0.95 eV, ϕ_2 as 0.3 eV and dielectric thickness as 3 nm. It is observed that this theoretical result matches

the actual results than the previously obtained theoretical plot. A possible explanation for the lower effective barrier might be that for thin oxides (3 nm), the barrier does not necessarily have a long periodic structure, consisting of only few monolayers. This might produce a reduced barrier height, which is not accounted for in the tunneling equation. Additionally, the image charges reduces the barrier height, which is not taken into account. These combinations would have reduced the effect barrier height of the junction.

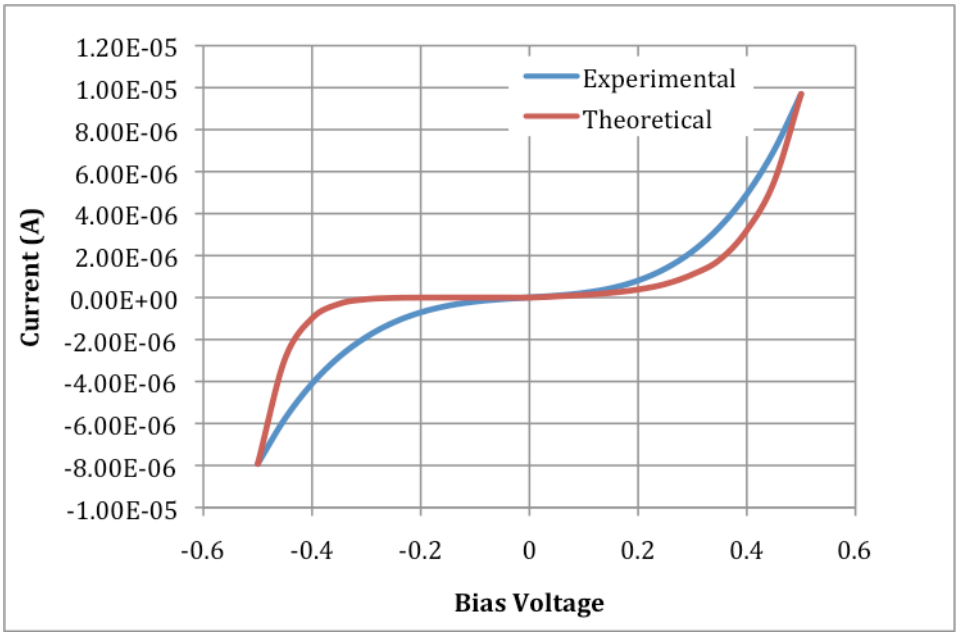

Figure 6.13: Experimental and Theoretical I-V Characteristics of MIM Diode

6.3 Comments on DC Characteristics of MIM Diodes

MIM diodes with two different contact areas (100 μm^2 and 1 μm^2) were fabricated with Ni-NiO-Cr and tested for its DC I-V characteristics. Although the I-V characteristics of the diodes were similar, the output current, sensitivity and the zero-bias resistance (ZBR) exhibited by the diodes vary. Table 6.1 shows the variation in the electrical characteristics of the measured diodes.

Table 6.1 Electrical Characteristics of MIM Diode

Diode Area	100 μm^2	1 μm^2
Current	10 μA	5 μA
ZBR	500 K – 800 K	~ 900 K
Sensitivity	15 V^{-1}	7 V^{-1}

It is observed that as the diode area decreases from 100 μm^2 to 1 μm^2, the current and sensitivity drops while the zero-bias resistance increases. However, the size of the contact area affects the diode behavior, there are other factors that contribute to this variation. Upon close observation of each diode, it can be noted that, the current varies from diode-to-diode on the same substrate. This is due to the variation in dielectric thickness across the device. The variation in dielectric thickness or roughness can change the device parameters. The dielectric thickness in the fabricated MIM diode was determined to be 3 nm using an ellipsometry technique, but was observed to be ~ 5 nm in the cross-sectional SEM image shown in the previous chapter. As reported in [60]

disorder effects in MIM junctions are highly unpredictable. Hence even a small thickness variation in the dielectric layer could cause a large fluctuation in its electrical behavior of the diode.

The formation of the dielectric layer seems to be very sensitive, which alters the uniformity of the film even when the samples were processed under the same conditions. Although an optimized deposition condition was established, the dielectric thickness varies from device to device as observed from the output current. Sze [45] indicated that even if the dielectric is not uniform, the thinnest portion in the oxide layer seems to be responsible for the tunneling current. This ensures that, as long as the dielectric layer is thin and without any micro or nano-pores, conduction would take place and the current observed will be an inverse function of dielectric thickness.

Furthermore, the roughness of the dielectric layer was determined in the previous chapter to be ~ 0.6 nm in a 3 nm film. The surface non-uniformity influences the current-voltage characteristics by increasing the active area of the diode. Eventhough the contact area of the diode is estimated to be 1 μm^2, due to film roughness and lithographic misalignment the actual area responsible for conduction can be more than expected. This can further reduce the device performance. Several other factors can also contribute to the dielectric variation beginning with the sample placement on the substrate holder to the slight environmental variation in oxide deposition conditions which might alter the roughness of the top and bottom interfaces of the oxide layer [61].

6.4 Temperature Dependency of MIM Diodes

Tunnel diodes are capable of carrying large currents. The flow of this current results in joule heating of the diode stack. Hence the thermal stability and response of the diode is a critical parameter that needs to be understood to ensure that the diode is not overloaded. In this section the temperature dependency of a MIM diode at high temperature will be discussed.

The MIM diodes developed earlier reported the electrical parameters and other figures of merit exhibited at room temperature [62]. However, the performance of the Ni-NiO-Cr with an ultra-thin insulator layer at elevated temperatures has never been reported. A comprehensive understanding of thermal stability and response of the MIM diodes is critical prior to its use in commercial products. In this experiment the diodes were heated to different temperatures up to 400ºC, and then tested again to evaluate their electrical characteristics, particularly the I-V characteristics, zero-bias resistance and sensitivity of MIM junctions. The resistance and the sensitivity were extracted from the current-voltage (I-V) curve. For this experiment a MIM diode with 100 μm^2 contact area was selected, due to the relative ease of measurement and an insulator are large enough to verify the morphology at different temperatures.

6.4.1 Electrical Characterization

For the post-deposition annealing process, a ceramic hot plate was utilized. The samples were annealed at 250°C, 350°C and 400°C for 15 minutes under ambient conditions and then the I-V measurements were determined for the different temperature

variants at room temperature. Post deposition annealing is known to improve the electrical properties of thin film diodes [63, 64] and the resistivity of NiO thin films have been reported to change when the structure changes from amorphous to polycrystalline at higher substrate temperatures [65]. Figure 6.14 shows the I-V plot of the MIM diodes measured after annealing at four different temperatures.

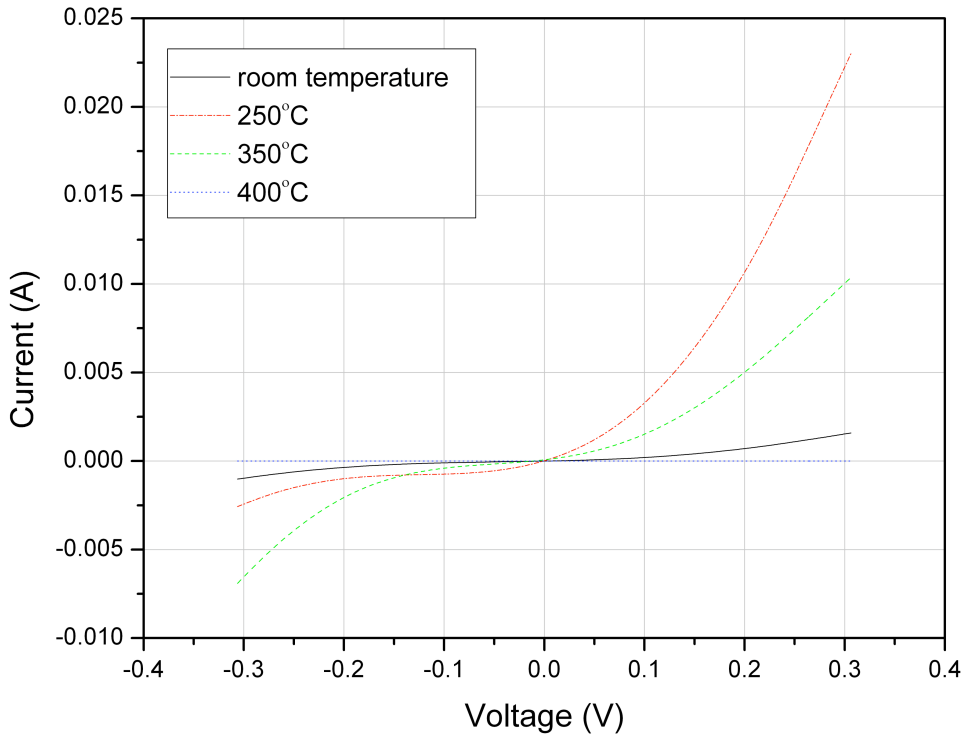

Figure 6.14: I-V Characteristics of MIM Diode Annealed at Different Temperatures

As can be seen from Figure 6.14, all the diodes exhibited non-linear and highly asymmetric characteristics with higher current output than the unannealed diodes. From

Figure 6.14, it can be observed that the un-annealed diode exhibits a forward bias current of ~ 2 mA. When the diodes were subjected to heat treatment; at 250°C, the forward bias current increased to ~20 mA. Upon increasing the annealing temperature to 350°C, the current reduced to 10 mA. Finally, when the diodes were subjected to a temperature of 400°C, a steep drop in current to the range of few nA was observed. Additionally, from the I-V characteristics, the sensitivity of the diodes was also extracted. Figure 6.15 shows the sensitivity of the MIM diodes annealed at various temperatures.

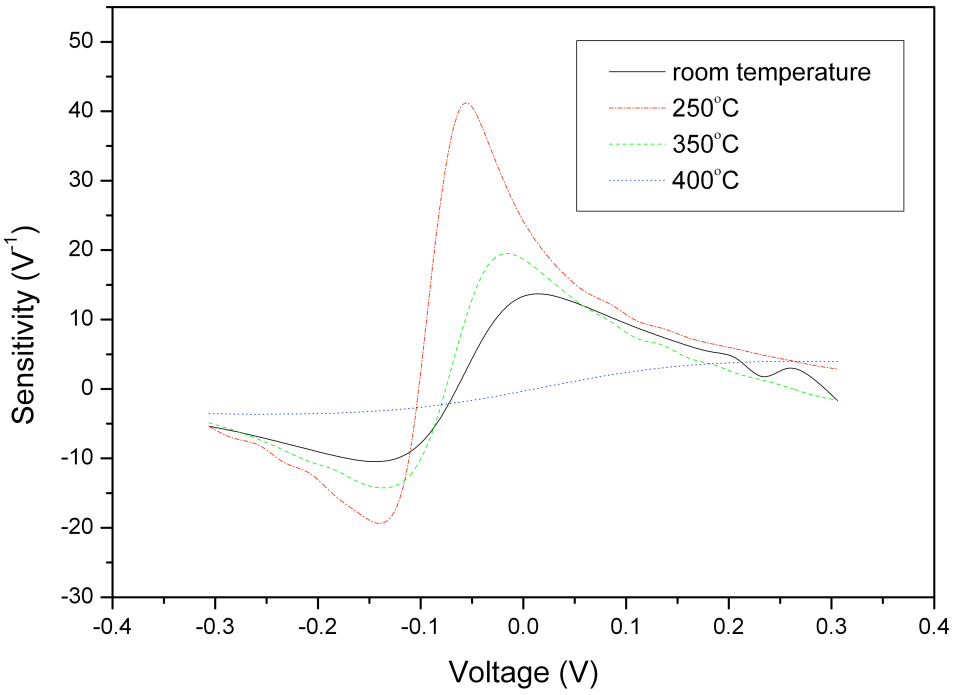

Figure 6.15: Sensitivity of MIM Diode Annealed at Different Temperatures

For the un-annealed diodes, the sensitivity was found to be $14V^{-1}$, which was typical for the 100 μm^2 MIM diode. The diodes annealed at 250°C had an increased electrical response with a very high sensitivity of $42V^{-1}$. Upon increasing the annealing

temperature to 350°C, the diode current dropped, but still was higher than the room temperature diode and the sensitivity was determined to be $23V^{-1}$. This demonstrates that the diode is still operational, even though the current and sensitivity dropped. When the diode was further annealed at 400°C, the current dropped instantaneously; exhibiting a very low sensitivity of $4V^{-1}$. To better understand this behavior, the resistance at zero-bias was determined from the I-V characteristics, since it is exponentially dependant on the width of the tunneling layer. Figure 6.16 shows the variation in sensitivity and zero bias resistance with change in the annealing temperature on the MIM diode. The un-annealed diode exhibits a zero bias resistance of ~800 Ω which decreases to ~300 Ω when the diode was annealed at 250°C. When the diode was further annealed the zero bias resistance increased to ~1400 Ω. However, when the annealing temperatures exceeded 400°C, the zero-bias resistance increased sharply to the GΩ range causing the diode to be un-operational.

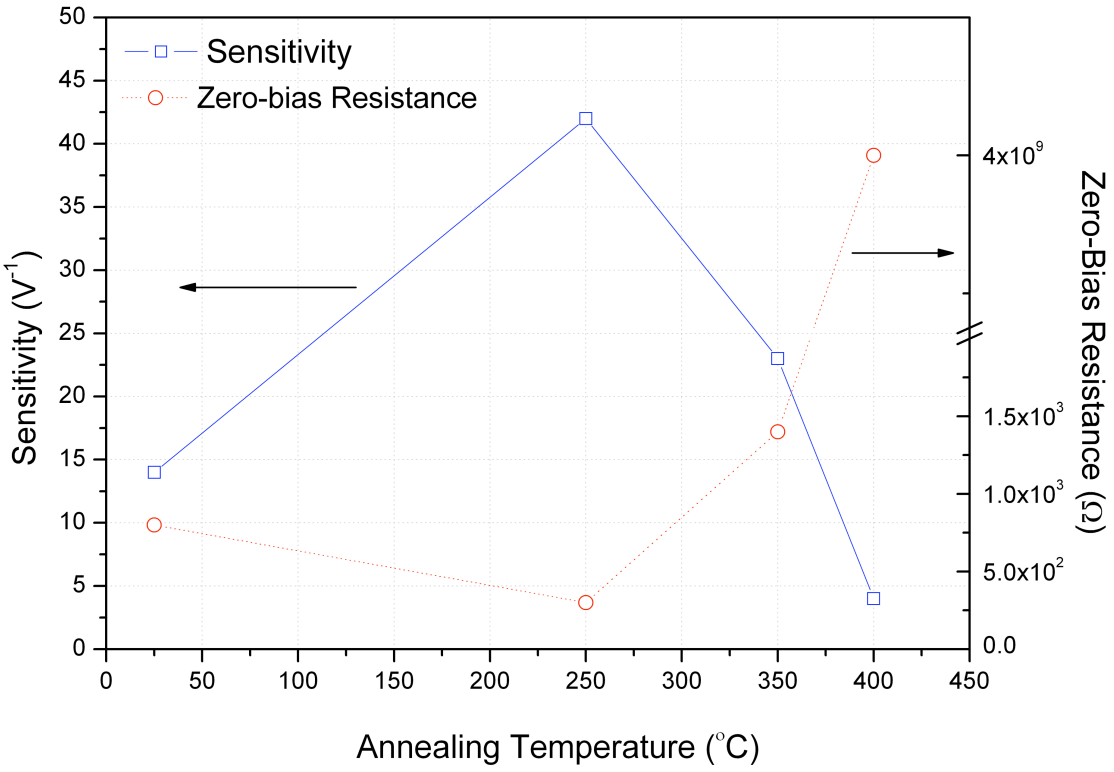

Figure 6.16: Zero-Bias Resistance of MIM Diode Annealed at Different Temperatures

A similar phenomenon was observed in [63, 64], wherein the current increases upon increasing the annealing temperature causing lowering of barrier height between the oxide and metal interface. This decrease in barrier height causes more electrons to tunnel through the insulator layer. However, when the annealing temperature was increased to 350°C, we observe a drop in current and sensitivity. This can be attributed to the increase in barrier height and width due to the interdiffusion of metal and oxides, which reduces the probability of electron tunneling. Also the structural transformation of the insulator layer and possible O_2 deficiency in the insulator layer can be contributed to the

degradation in the electrical characteristics of the MIM diode. The un-annealed diodes exhibit a low electrical response, which is enhanced by annealing it to 250°C and degrades upon subjecting them to further annealing. At 250°C, the electrical as well as structural changes affect the MIM stack, especially the insulator layer. Hence the structural analysis of the MIM junction needs to be analyzed.

6.4.2 Structural and Morphological Characterization

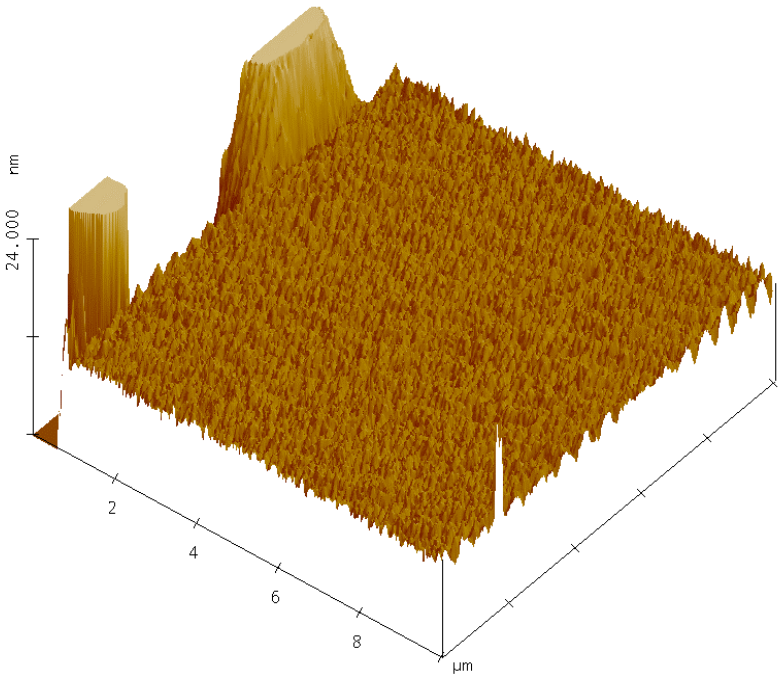

(a)

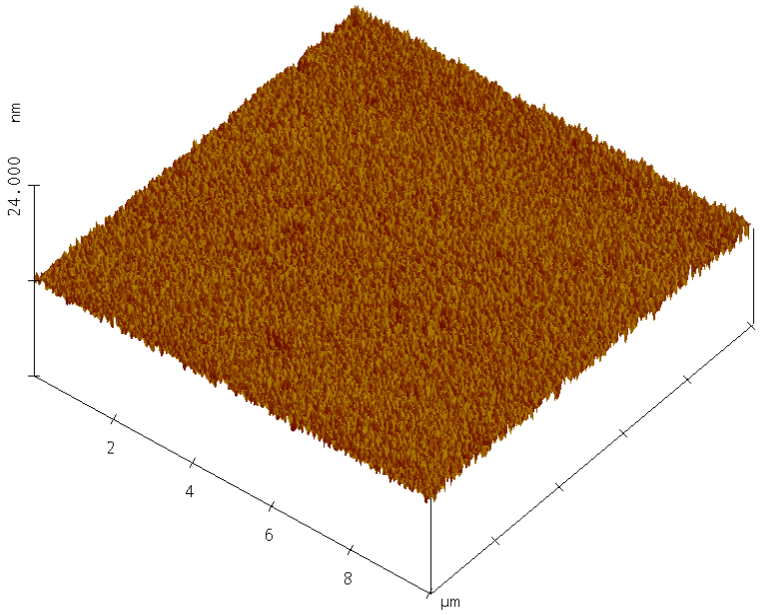

(b)

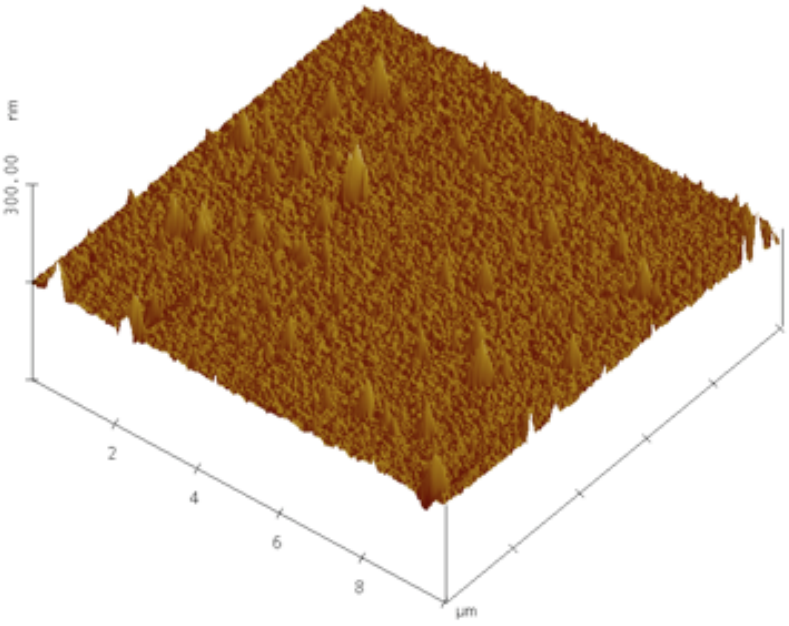

(c)

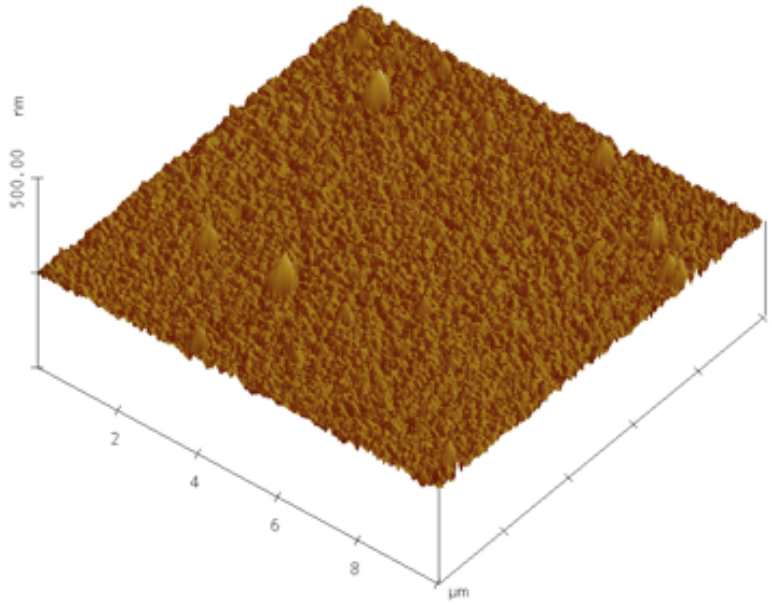

(d)

Figure 6.17: AFM Micrograph of Samples Annealed at (a) Room Temperature, (b) 250°C, (c) 350°C, and (d) 400°C

AFM data shown in Figure 6.17 represents the effect of annealing temperature on the surface morphology of NiO films deposited by plasma oxidation. The un-annealed sample exhibits a uniform amorphous film as seen in Figure 6.17(a), over the 10 μm^2 area. The surface roughness of the un-annealed film was determined to be 0.6 nm on a ~ 5 nm thick NiO film. As the temperature was increased, NiO grains of varying sizes started to appear. Figure 6.17(b) shows the AFM morphology of the sample annealed at 250°C. It is observed that the film is very uniform with 0.37 nm surface roughness. Upon annealing at 250°C the roughness of the diode decreases, causing enhanced electrical response. However, the roughness of the NiO film increases as the annealing temperature

further increases. Figures 6.17(c) and (d) show the NiO film annealed at 350 and 400°C respectively, exhibiting larger grain size and inhomogeneous surface. The roughness of the 350 and 400°C samples was determined to be 5.4 and 7.2 nm respectively. The roughness of the NiO film initially drops at 250°C, but tends to increase with higher temperature, suggesting the formation of a crystalline phase and also due to diminishing grain boundaries. But with higher temperatures lattice mismatch occurs increasing the grain growth and making the structure more crystalline.

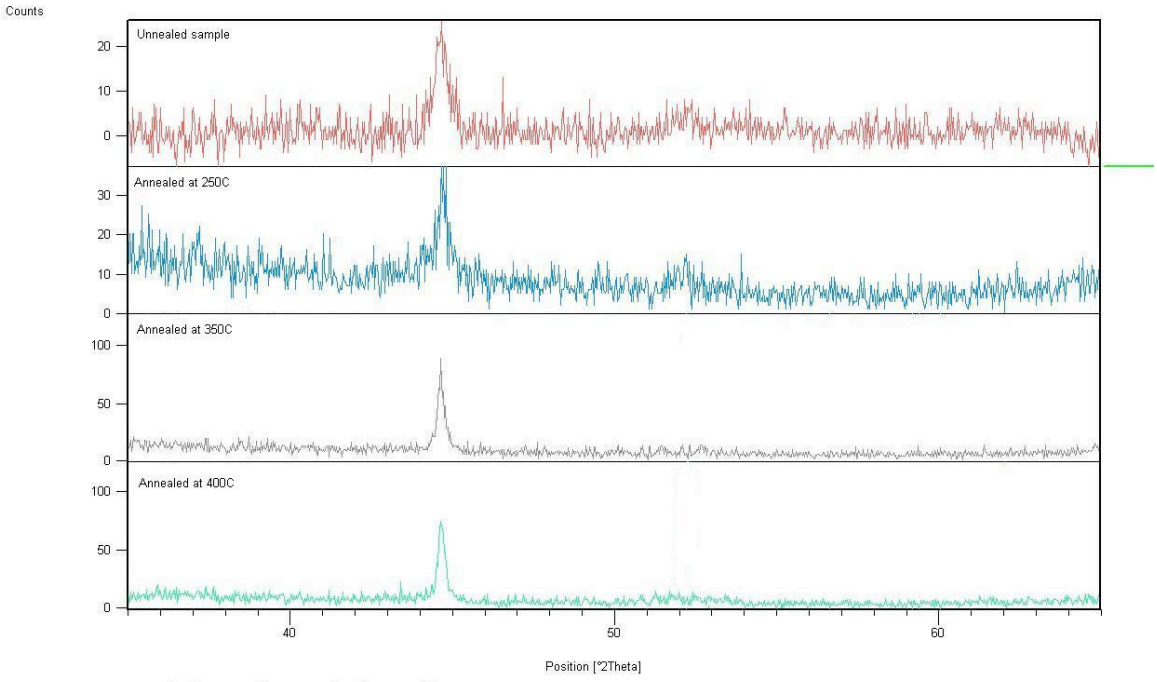

Figure 6.18: XRD Pattern for NiO Films Deposited Through Plasma Oxidation and Annealed at Different Temperatures

Figure 6.18 shows the XRD pattern for NiO films deposited with plasma oxidation and annealed at temperatures varying from room temperature to 400°C. From the XRD spectra of the NiO films it was found that the oxide films had both amorphous and polycrystalline structures. The diffraction pattern for the un-annealed sample shows a NiO peak with low intensity. These films exhibited less current due to the amorphous nature of the film. On the other hand, the diffraction patterns of the annealed samples show the presence of diffraction peaks with a NiO (200) orientation. As the annealing temperature increases, the crystallinity increases (shown by increased peak intensity), causing an increase in current tunneling through the insulator layer. At 350°C, we observe a drop in tunneling current, which drops steeply when the annealing temperature was increased to 400°C. Also it is noted that the intensity of the peak increases with a strong (200) peak indicating increased crystalline structure. Hence this data agrees with the AFM as well as the electrical response of the MIM diode at different temperature.

The XRD and AFM analysis clearly shows the structural transformation for NiO films annealed at different temperatures. This analysis suggests that although amorphous structures yield good electrical characteristics, annealing to 250°C improves the electrical response. By annealing to 250°C, the insulator layer undergoes a phase transformation from being amorphous to polycrystalline, forming a homogenous film with less surface roughness than the un-annealed film. This causes the diode to conduct more current through the NiO layer. The samples annealed at 350 and 400°C exhibited a more crystalline surface with much larger grain sizes, thus impeding the tunneling of electrons through the insulator layer.

As mentioned earlier, the insulator layer was deposited by plasma oxidation at low substrate temperatures, typically depositing a uniform amorphous film. Formation of polycrystalline NiO seems to stabilize the electrical property and enhance the thermal stability of the material. However a crystallized film demonstrates degradation in electrical characteristics. In order to understand the physical nature of the insulator layer changing from amorphous to crystalline by post deposition annealing, a cross-sectional TEM study was performed. Figure 6.19 shows the microstructural TEM images of a MIM diode annealed at different temperatures.

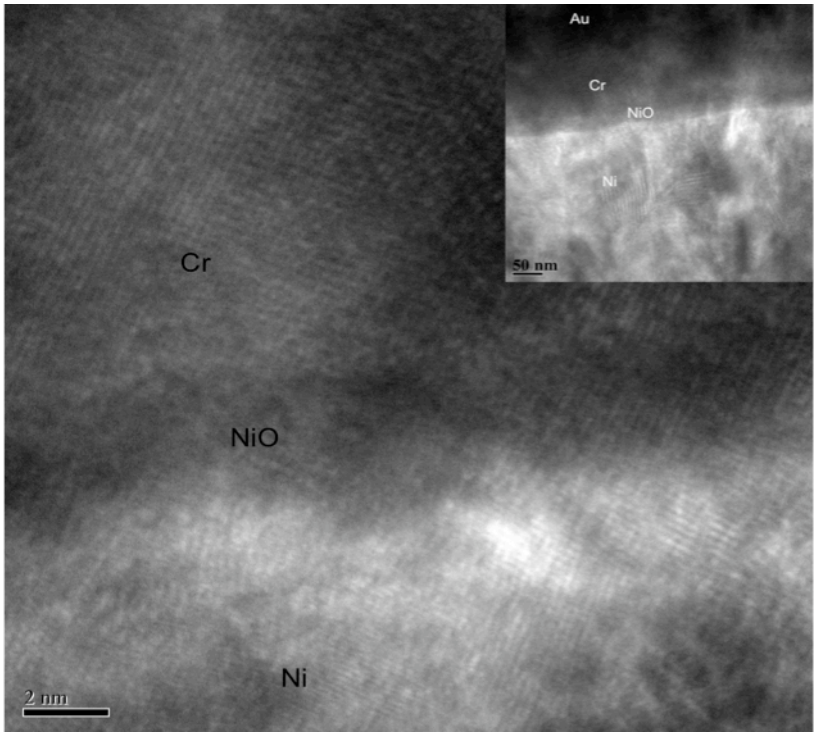

(a)

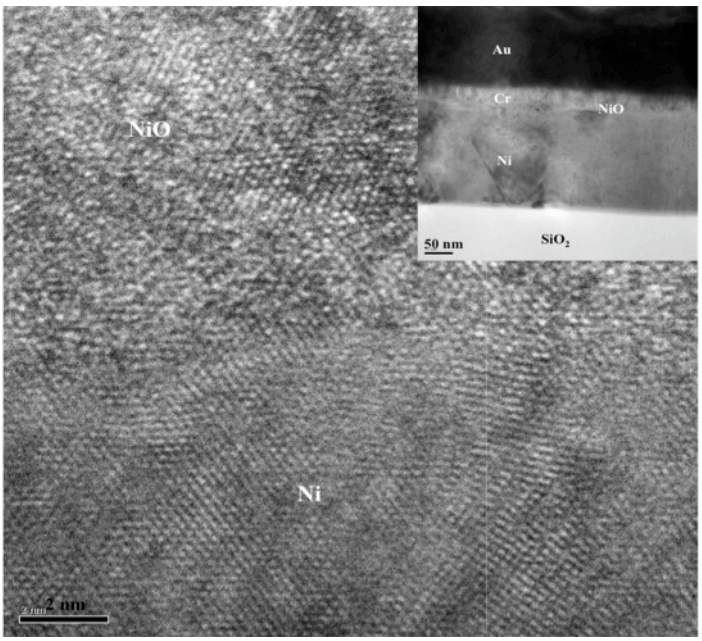

(b)

Figure 6.19: TEM Micrograph of MIM diode Annealed at (a) 250°C and (b) 350°C

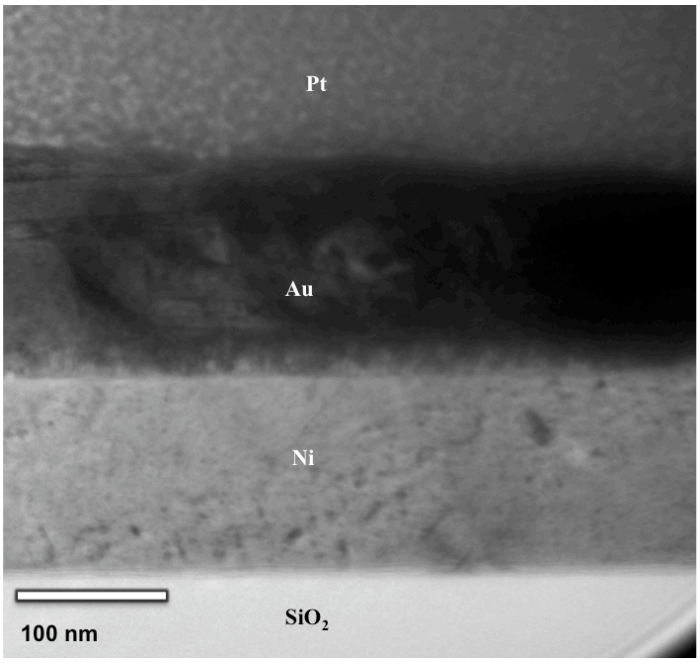

Figure 6.20: TEM Micrograph of MIM Diode Annealed at 400°C

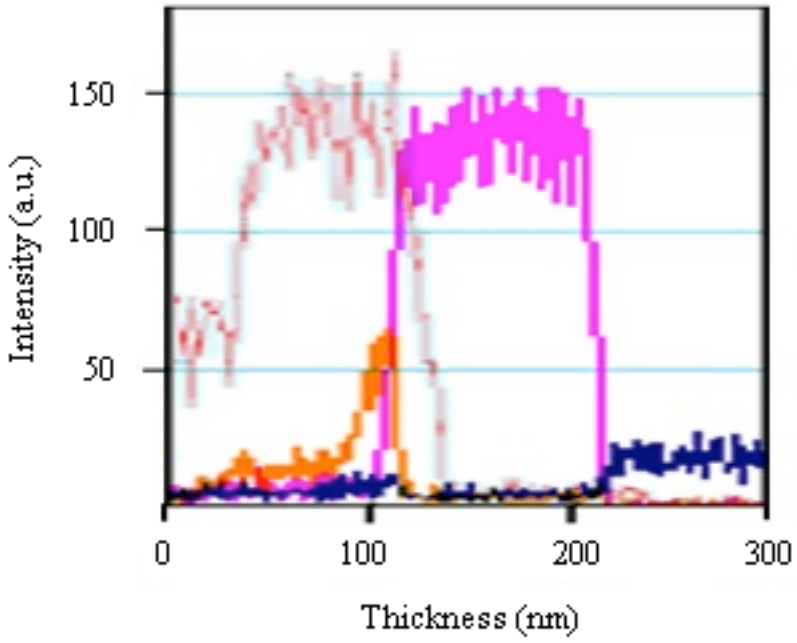

Figure 6.21: Energy Dispersive Spectra Showing the Diffusion Length of Annealed Materials.

Data shown in Figures 6.19(a), and (b) were obtained from samples subjected to 250 and 350°C annealing, respectively. The cross-sectional micrograph of the as-deposited MIM diode shown in a previous chapter exhibits a distinct transition between each layer. Similarly the sample annealed at 250°C shown in Figure 6.19(a) also exhibits a definite boundary between each layer. Moreover, the insulator region exhibits a polycrystalline structure with finer grain as confirmed by the AFM morphological analysis. However, the sample annealed at 350°C shows a clear crystalline structure as can be observed in Figure 6.19(b), which correlates with the XRD data. The inset micrograph shows the MIM stack with different layers. This phase transformation of the insulator layer provides evidence for the decrease in current and sensitivity.

When compared with the TEM image of the MIM junction annealed at 350°C, the film annealed at 400°C shown in Figure 6.20 has a deteriorated film structure. Specifically, the individual layers were merged at the higher annealing temperature. A diffused boundary between the Ni and Au layer can be observed from Figure 6.20.

In order to identify the composition of the film annealed at 400°C, the energy dispersive spectrum (EDS) was obtained on the TEM. The spectrum with different layers in the MIM stack is shown in Figure 6.21. It is well known that the high temperature annealing can cause diffusion of the elements in different layers. As shown in Figure 6.21, the EDS spectrum shows a large intensity of Ni and Au than any other element, revealing the diffusion length of different elements in the MIM structure. As evaluated earlier, the Au layer has diffused all the way to the Ni layer through the insulator suggesting the diffusion of Au as the cause for the device breakdown at annealing temperatures over 350°C.

Thus, these experiments provide the data for efficient operation of MIM diodes up to 350°C. Although the diode operates well at room temperature, annealing it to an optimal temperature (250°C in this case) enhances the performance of the diode. The annealed diode exhibits higher current, sensitivity and low zero bias resistance. Based on these results, it is suggested that the annealing temperature must be restricted to temperature below 350°C to minimize the degradation in electrical properties caused by the crystalline nature as well as the interdiffusion of the MIM layers. Nevertheless, the electrical and structural analysis suggests 250°C is the optimal temperature at which the MIM can perform with better characteristics.

6.5 Thickness Dependency of MIM Diodes

As mentioned earlier, the conduction in a tunnel junction is limited by the dielectric thickness. In order to facilitate electron tunneling, the insulator layer has to be fabricated with a very thin film – on the order of few nanometers. In this section, the thickness dependency of a MIM diode on its electrical performance will be discussed. For energy conversion and detection purpose MIM diodes are typically fabricated with an ultra thin insulator layer. In this experiment, MIM diodes were fabricated with three different thicknesses of insulator; specifically 40, 20 and 10 nm thick dielectric was deposited. The electrical characteristic of each diode was then measured using the previously mentioned test set-up. Figure 6.22 (a), (b), (c) shows the I-V characteristics of MIM diodes with different dielectric thicknesses.

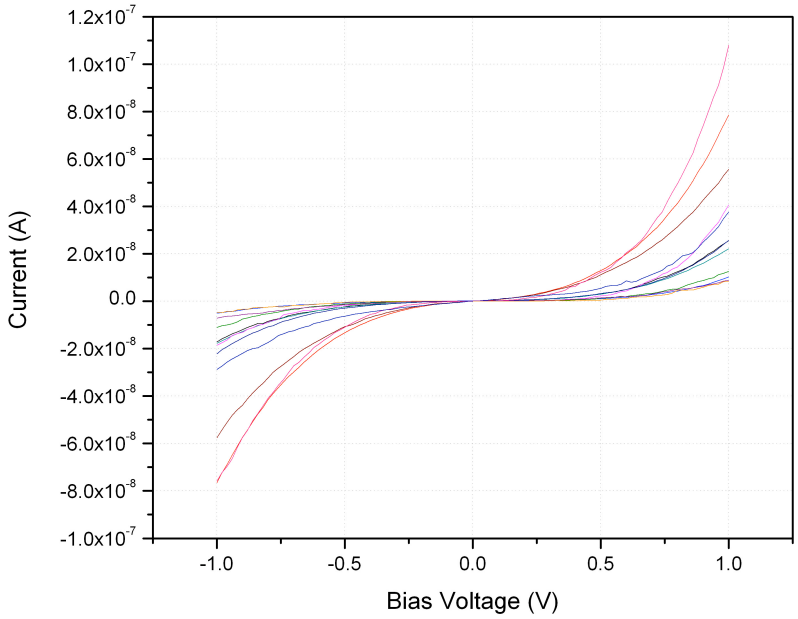

(a)

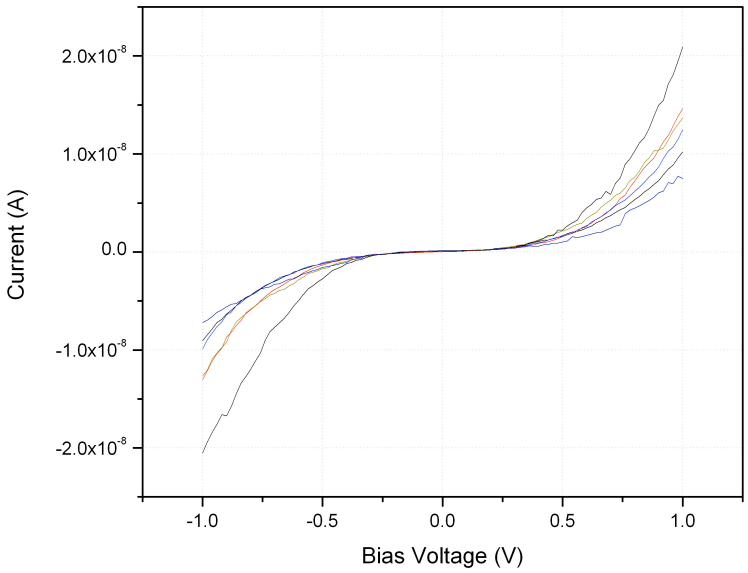

(b)

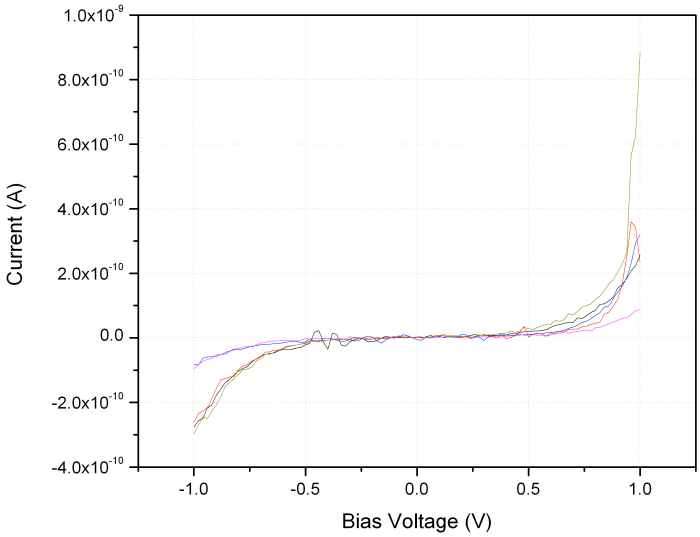

(c)

Figure 6.22: I-V Characteristics of MIM Diode Deposited with (a) 10 nm, (b) 20 nm and (c) 40 nm NiO

As can be seen from Figure 6.22, all the diodes exhibited non-linear and highly asymmetric characteristics, but with much lower current. The diode deposited with 10 nm of NiO exhibited a maximum forward bias current of ~ 100 nA. When the thickness was increased to 20 nm, the diode exhibited a drop in tunneling current. The maximum forward bias current at 1V was in the order of ~ 20 nA. The diodes with the highest thickness of 40 nm yielded a maximum tunneling current of 1 nA. Hence, when the thickness of the dielectric doubles, the current decreases by a factor of five. It is observed that the variation in current at forward bias for a 10 nm thick dielectric is noticeably large compared to 20 nm and 40 nm MIM junctions. This suggests that at lower thickness, the uniformity is being compromised across the diode. This experiment verifies the dependency of tunneling current on dielectric thickness. Thus, in order to obtain higher current output, the dielectric thickness should be very thin and uniform

In summary, all the MIM diodes fabricated with NiO as well as polyaniline insulator exhibited significant asymmetry and nonlinearity. The sensitivity obtained from these diodes was also significantly higher than any reported value. Also, when the diodes were subjected to heat treatment, the electrical characteristics were observed to be stable up to 350°C, while the optimal anneal temperature for better diode performance was determined to be 250°C. The sensitivity of the diodes also increased upon annealing. In addition, when the dielectric thickness was increased a significant drop in the current was observed proving the dependency of electrical characteristics on the insulator thickness. A comparison table is presented showing the sensitivity obtained by different research

groups. Table 6.2 presents a comparative table showing the sensitivity values obtained by different research groups using different design and material combinations.

Table 6.2: Comparison of Sensitivity of MIM Diodes Fabricated by CERC with other Research Groups

Research Group	*Type of MIM diode*	*Junction Area*	*Sensitivity*
Heiblum et. al. [39]	Ni-NiO-Ni	3.8 μm^2	4.3 V^{-1}
Hoofring et. al. [4]	Ni-NiO-Au	0.64 μm^2	4.55 V^{-1}
UCF – CREOL [26]	Ni-NiO-Ni	0.075 μm^2	2.75 V^{-1}
ETH, Zurich [40]	Ni-NiO-Ni	0.056 μm^2	1.6 V^{-1}
UND [41]	Ni-NiO-Pt	0.0025 μm^2	-13 V^{-1}
UND [41]	Al-Al_2O_3-Pt	0.0025 μm^2	1.3 V^{-1}
UND [41]	Al-Al_2O_3-Ni	0.0025 μm^2	1 V^{-1}
UND [41]	Al-Al_2O_3-Al	0.0025 μm^2	-1.4 V^{-1}
CERC	Ni-NiO-Cr	100μm^2	14 V^{-1}
CERC	Ni-NiO-Cr	1μm^2	7 V^{-1}
CERC	Ni-NiO-Cr Annealed at 250°C	100μm^2	42 V^{-1}

CHAPTER 7

LOW FREQUENCY AND MILLIMETER WAVE MEASUREMENTS

In this chapter the low frequency and mm-wave wave response of the MIM diode is discussed. Low frequency measurements were performed on the 100 μm^2 area diode and the 1 μm^2 area diode while mm-wave measurements were carried out on the 1 μm^2 MIM diode. Millimeter-wave measurements were performed by feeding a 94 GHz signal to the individual diode elements through a waveguide. The rectified output was observed and recorded through a high precision digital multimeter.

7.1 Experimental Arrangement:

The low frequency measurement of 100 μm^2 diode and 1 μm^2 diode was performed using a different set of measurement units. For the 100 μm^2 diode, since the operation frequency was much lower, a function generator from Agilent Technologies (Model 33220A) was used as the input source. The output from the diode was recorded using a digital oscilloscope from Tektronix (Model TDS 3014). The diodes were connected via a coaxial cable through a probe station from Micromanipulator Company, Inc., (Model 6200). The function generator can produce frequencies up to 20 MHz with a maximum 10 V peak-peak, while the oscilloscope was capable of exhibiting up to 5 MHz signal on 4 channels. A schematic arrangement for measuring the 100 μm^2 MIM diode is

shown in Figure 7.1 (a). The input signal from the function generator was also hooked up to one of the channels in order to compare the input and output signal.

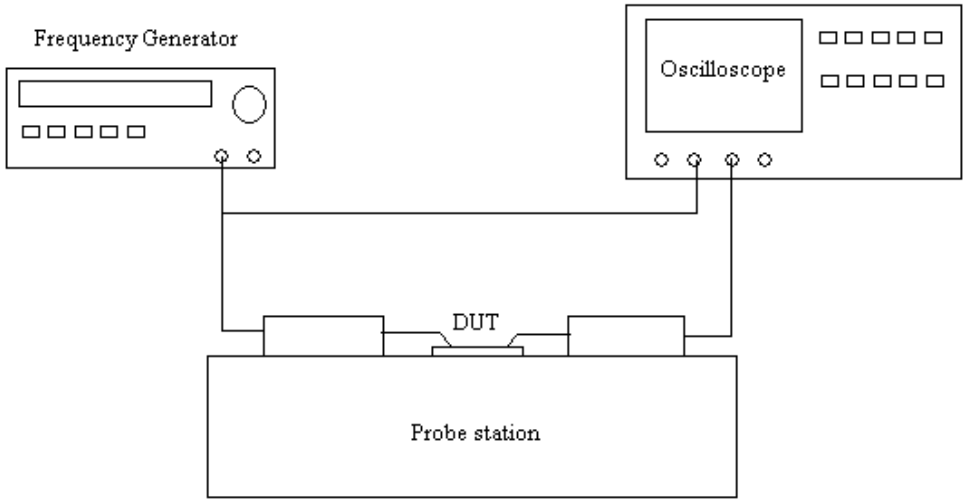

(a)

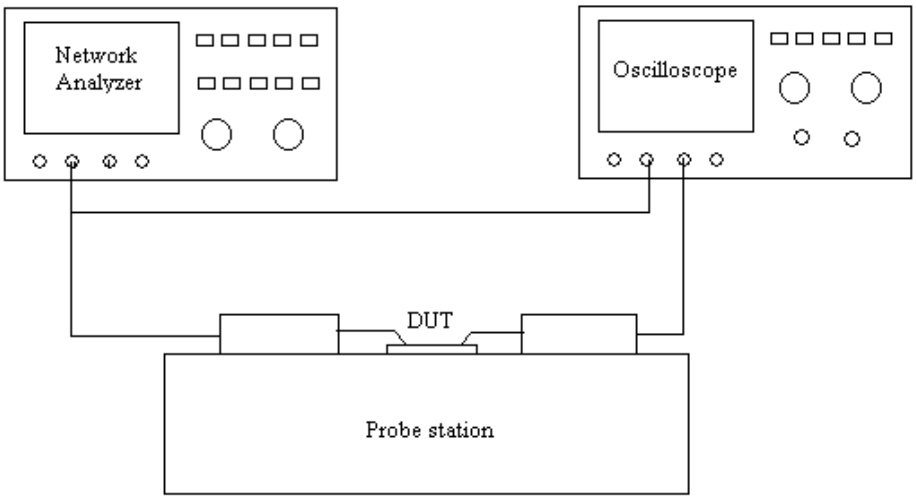

(b)

Figure 7.1: Schematic of the Test Set-up Used for Measuring the Low Frequency Behavior of (a) 100 μm^2 and (b) 1 μm^2 Area MIM Diode

The low frequency response of the 1μm^2 diode was measured in a different set-up since the input signal source had to be more than 20 MHz. For this purpose, a network analyzer was used as the signal source along with a high frequency oscilloscope. The network analyzer used for this purpose was Agilent's 8713D capable of generating signals up to 13 GHz. Similar to the low frequency measurement, the input from the network analyzer was connected to one of the channels on the oscilloscope and to the input of the diode through a high-frequency gold coated probe. A Karl-Suss semi-automatic (Model SA-5) probe station was used for this purpose. The output of the diode was connected to the digital oscilloscope via the probe station. The experimental arrangement for this measurement is very similar to the previous measurement set-up, shown in Figure 7.1 (b).

The mm-wave measurements were carried out with the experimental arrangement shown in Figure 7.2. A Wiltron 360B vector network analyzer (VNA) was used as the signal source for mm-wave measurement through a waveguide conversion module. The input signal was fed to the diode through the gold transmission line and the output of the diode was connected to a high precision digital multimeter from Keithley Instruments Inc., (DMM 2000). The VNA also has the capability to change the input power that can be added to the source signal. The probe station used for this measurement was the same as the one used for low frequency measurements. However, for the high frequency measurement, to minimize signal losses, special types of probes were used. The probes were connected to the waveguide of the VNA module and had a probe pitch of 150 μm, which was the spacing for the CPW lines fabricated along with the MIM diodes.

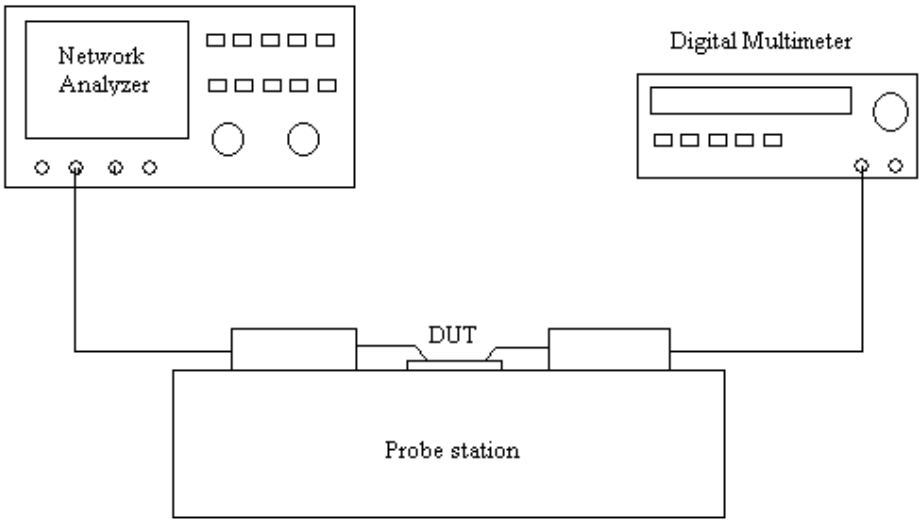

Figure 7.2: Schematic of the Test Set-up Used for Millimeter Wave Measurement

Figure 7.3: Actual Millimeter Wave Test Set-up Used to Measure the MIM Diode

7.2 Experimental Results

7.2.1 Low Frequency Characteristics of 100 μm^2 MIM Diode

In order to verify the concept of rectification in the MIM diode, the low frequency behavior of MIM diode fabricated with 100 μm^2 contact area was measured. A function generator provided an AC signal and the DC out was measured using an oscilloscope. The function generator was connected to one terminal of the diode and the output was connected to the oscilloscope. The cut-off frequency was determined to be around 1 MHz from the previous chapter; hence the input frequency was kept on the lower end and gradually increased. The input and the output signals observed on the oscilloscope are shown in Figure 7.4. Initially, the input frequency was kept at 100 Hz with 0 V offset voltage and a 2 V peak-peak voltage. The forward voltage was observed to be 29 mV and reverse voltage was 34 mV. This reversal in polarity is due to the interchange of input and output lines.

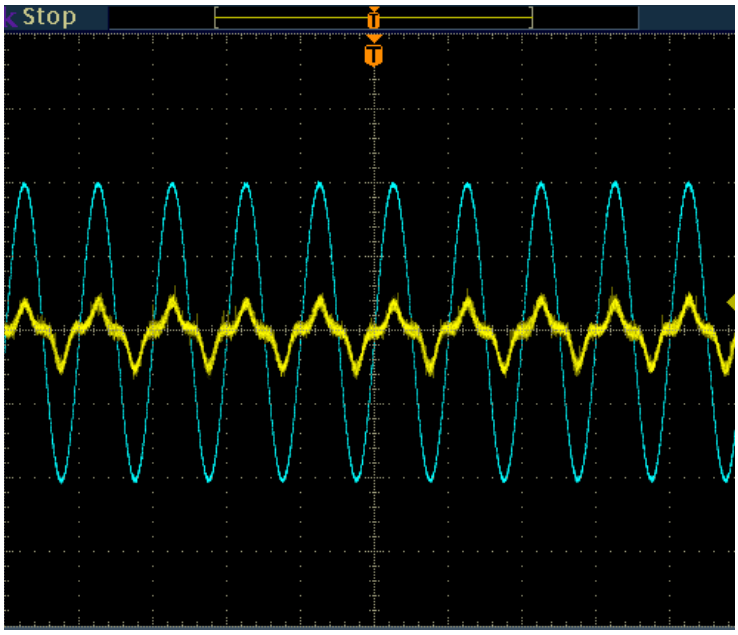

(a)

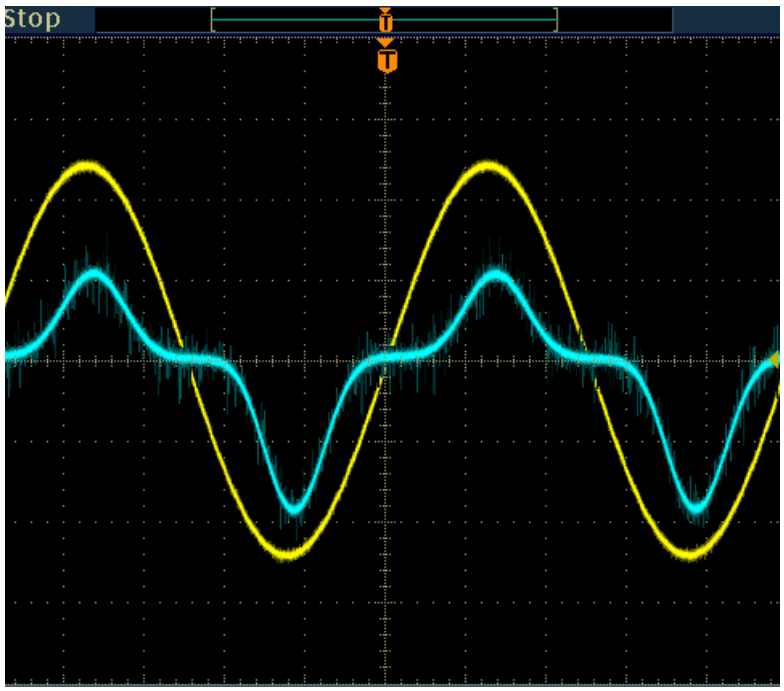

(b)

Figure 7.4: Rectification of 100 μm^2 MIM Diode at (a)100 Hz and (b)1 KHz

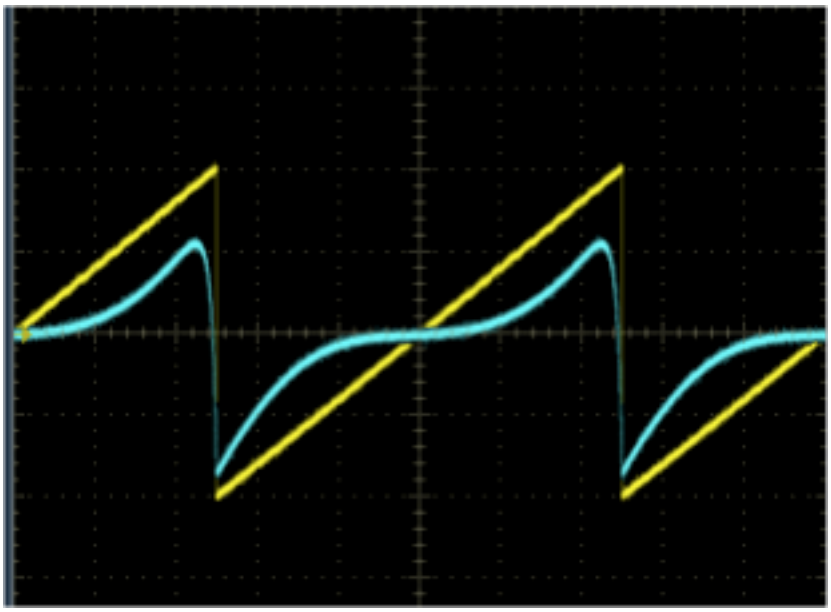

Figure 7.5: DC Output Signal of MIM Diode with a Ramp Function

Later the input frequency was increased to 1 KHz and the corresponding output was observed. Figure 7.4 shows the AC and DC signal observed form the diode at 100Hz and 1KHz. The diodes exhibited the same response when the frequency was increased. The forward voltage was observed to be 26 mV and the reverse voltage was 38 mV. Figure 7.5 shows the DC behavior of the diode when a ramp signal was given as the input. From the figure it can be observed that the DC out looks exactly like the I-V plot. Since the diode exhibits conduction in forward and reserves bias conditions, we can observe the DC out signal in both polarities. It is also observed that the DC output signal turns on after the input signal reaches a certain voltage and then turns off. The similar behavior is noticed in the reverse bias. The diode also demonstrates an asymmetric behavior showing different voltage out in the forward and reverse bias exhibiting MIM diode characteristics.

However, when the frequency was increased to 1 MHz, the DC signal started to lose the typical trend that was seen at lower frequencies and became more like a triangular wave. Although the cut-off frequency was determined to be ~ 1 MHz, the diode seems to lose its rectification property at much lower frequency. This change can be attributed to several diode issues, such as, aging, roughness in dielectric, and capacitance variations due to variation in dielectric thickness.

7.2.2 Low Frequency measurement of 1 μm^2 MIM Diode

Following the 100 μm^2 diode measurement, MIM diode with 1 μm^2 contact area was set-up for rectification measurement. Although the diodes were designed to operate at 94 GHz, the testing was carried out in the upper MHz regime. Since the function generator could produce only up to 20 MHz signal, a network analyzer capable of generating 13 GHz was used. As mentioned earlier this measurement was carried out in a different probe station setup. The signal from the network analyzer was connected to the input of the diode through a 150 μm pitch probe and the oscilloscope. The output from the diode was also connected to the oscilloscope. Since the oscilloscope could measure only up to 500 MHz, the input signal from the VNA was limited to 200 MHz. Figure 7.6 shows the AC to DC testing of the 1 μm^2 MIM diode at 200 MHz.

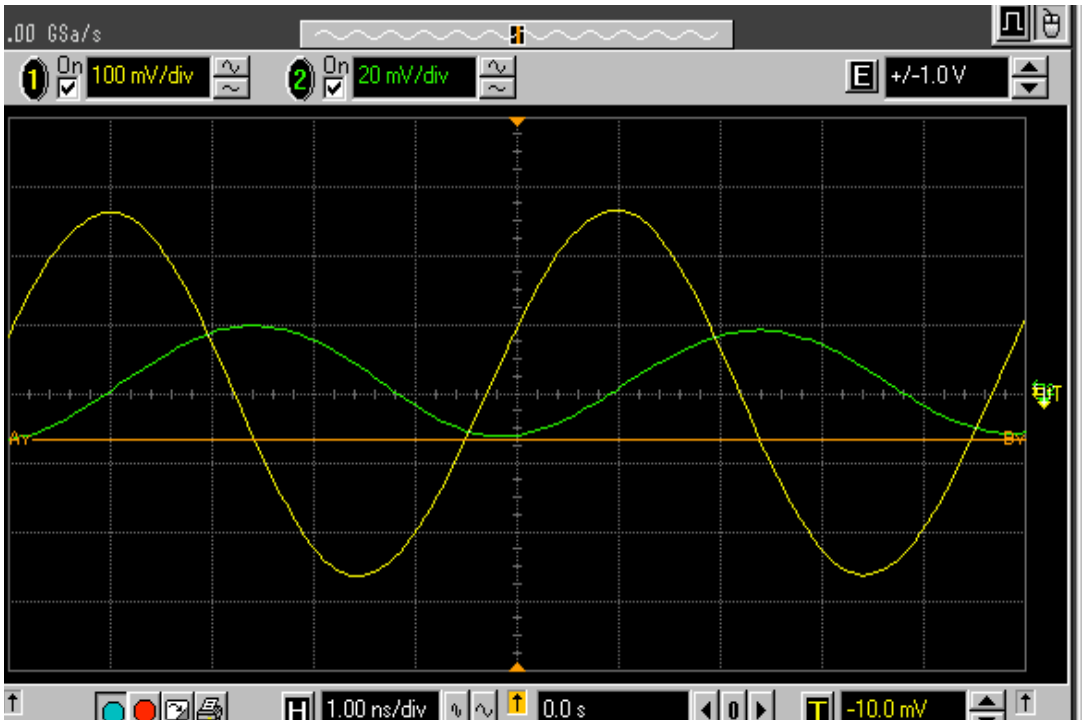

Figure 7.6: AC to DC Measurement of the 1 μm^2 MIM Diode at 200 MHz

The input frequency was set at 200 MHz with 500mV peak-peak signal. The diode did not demonstrate any rectification like behavior like the 100 μm^2 diode; instead the diodes exhibited an offset sine wave output with much smaller amplitude. Also it can be noticed that the output signal from the diode displayed larger amplitude in the forward cycle (20 mV) than the reverse (15 mV). This suggests that the diode exhibits asymmetric characteristics. The same characteristics was demonstrated when the frequency was changed from 50-200 MHz. When the amplitude was increased, the diode exhibited a slight form of charging and discharging effect like a RC circuit. Figure 7.7 shows the diode response with change in amplitude.

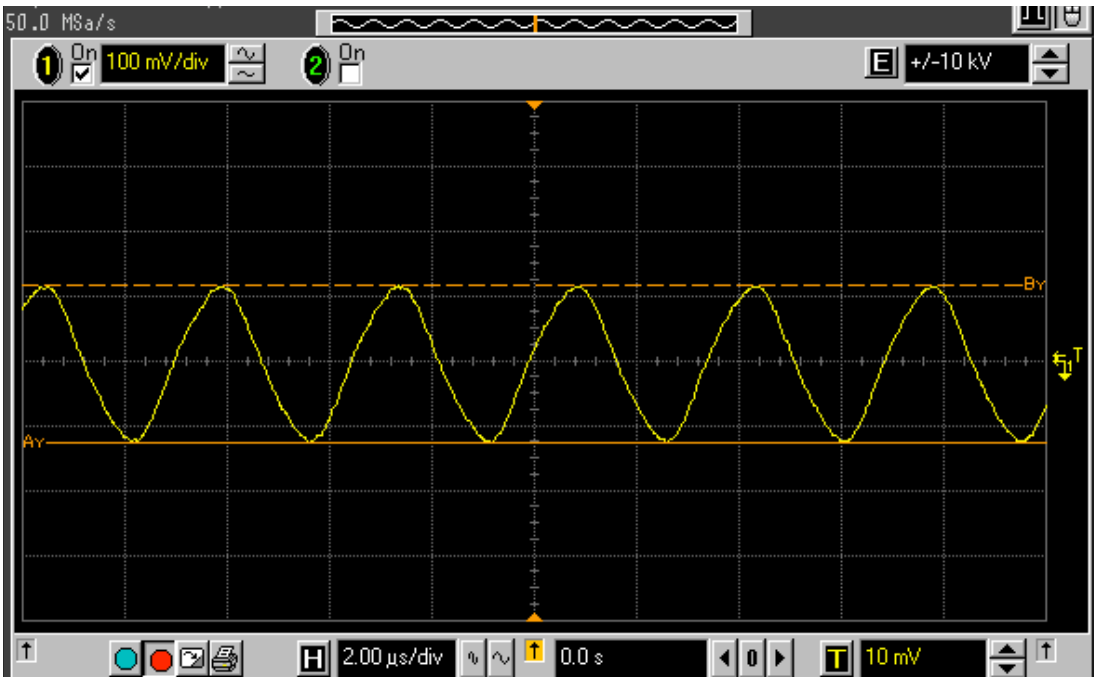

Figure 7.6: DC Response of 1 μm^2 Diode with Increase in Amplitude

A slight slant in the signal can be observed from Figure 7.7. Initially, the diode behavior exhibited an output signal with 20 mV. When the amplitude of the input signal was increased, the dc output voltage exhibited an increase in diode response. Although the diode did not exhibit rectification characteristics, it displayed a charging behavior suggesting a capacitor like structure. In a way a MIM diode is like a parallel plate capacitor structure. Moreover, the diode was fabricated for mm-wave testing, hence the lead lines and the transmission were designed to operate at high frequency, operating the diode at a lower frequency would not yield desirable result as observed.

Later, an external power supply (Keithley 2400) was connected to the diode input through the VNA to apply an external bias along with the RF signal. A high-precision multimeter (Keithley 2000) was also connected in parallel to the oscilloscope to measure the output current. The RF power was set at 10 GHz to be sourced from the VNA. The bias voltage was varied from 50 mV to 300 mV in steps of 50 mV and the corresponding current was measured. Also the RF power was switched changed from zero RF power to 0 dBm (1 mW). Thus current was measured by biasing the diode with RF power ON and OFF.

When the input signal was turned ON the diodes responded positively, resulting ~9.5 μA at 50 mV bias voltage and no RF power. When the RF power was turned on, the output current increased to ~ 10 μA. This behavior was also noticed when the bias voltage was gradually ramped up. From this experiment it is observed that apart from the external bias, applying an RF power also provides an extra bias, thus increasing the output current. Different diodes exhibited change in current upon applying external bias or power, which was typically in the range of tens of μA. This suggests that although the diodes did not exhibit typical rectification characteristics, applying a signal with and without external bias could generate an output current. Table 7.1 shows the change in current with change in bias voltage and RF power.

Table 7.1 Variation in Current with Change in Bias Voltage on 1 μm^2 MIM Diode

Bias Voltage (mV)	Current at No RF power (μA)	Current at 1mW power (μA)
50	9.55	9.92
100	19.2	20.1
150	29.3	30.6
200	39.7	41.5
250	49.4	51.5
300	59.2	62.2

7.2.3 Millimeter Wave Response of MIM Diode

The MIM diodes fabricated on silicon substrates were used for 94 GHz measurements. Wiltron 360B Network analyzer was used for the diode testing along with Wiltron SM5184 transmission and reflection module.

After the on-wafer calibration was performed, the probes were moved to the edge of the diode contact pads and gently placed to make a good contact. A 94 GHz signal with a 0 dBm power (1 mW) was given as an input to the MIM diode using the VNA as a continuous signal generator. The diode was connected to a multimeter to record the output current.

When the input signal was provided, the diodes responded positively and output current was measured in the multimeter. The current recorded was predominantly in the

order of low μA. The amplitude and Vp-p was not noted since, the VNA was not hooked up to an oscilloscope, which is the only way of know the input voltage. Due to the unavailability of a high frequency oscilloscope, the amplitude of the input signal could not be observed. Figure 7.8 shows the distribution of current recorded for different diodes upon feeding a 94 GHz signal. From the distribution it can be seen that all of the diodes exhibited various current output. This suggests that the 1 μm^2 diode fabricated with the aforementioned procedures have a non-uniform dielectric.

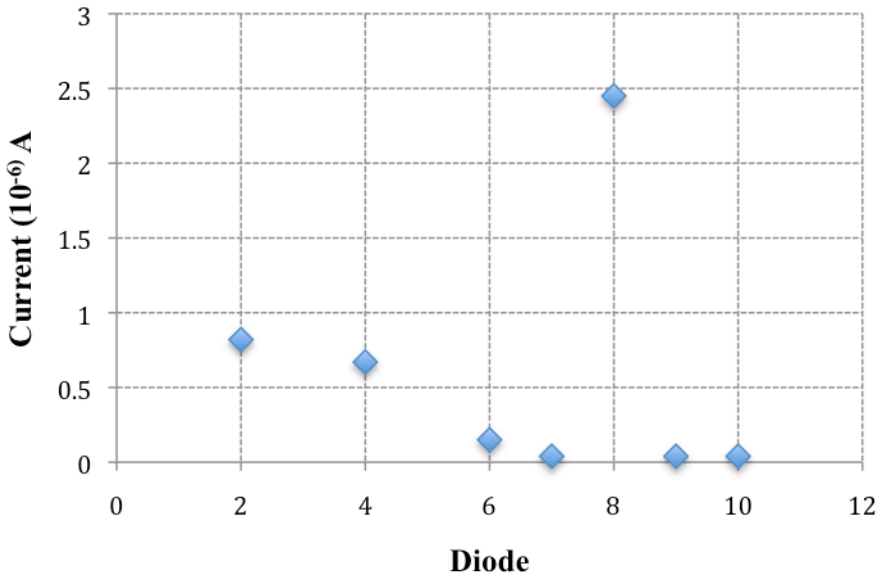

Figure 7.8: Distribution of Output Current for Diodes upon Subjecting to Millimeter Wave Signal

From the low frequency measurement of the 1 μm^2 diode discussed in the previous section, it was determined that by applying a bias voltage and RF power, a higher output current can be achieved. Hence even in the mm-wave measurement,

external bias was applied to the diode and the current was measured. The RF power was varied from -15 dBm to 5 dBm and the corresponding current was measured. Figure 7.9 shows the variation in current with input RF power in different diodes.

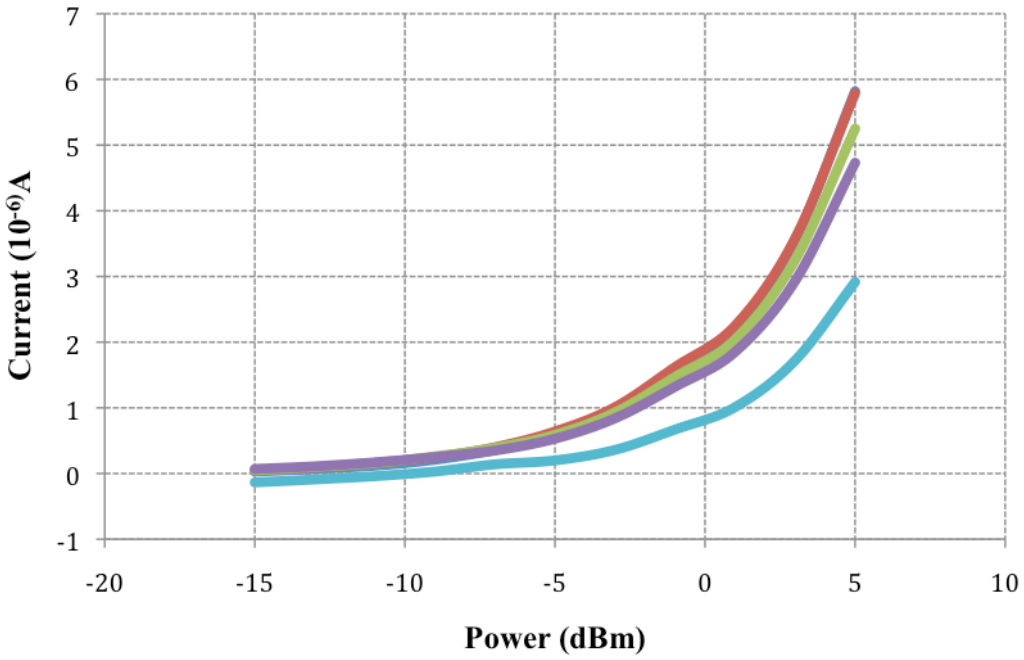

Figure 7.9: Variation in DC Current with Change in Input Power

As can be seen from Figure 7.8, all the diodes exhibited the same trend of increase in current with increase in RF power. From the AC measurements it can be noted that the current was in the same range as the DC I-V measurement discussed in the previous chapter. Although the diodes displayed acceptable level of output current, when considering the efficiency, the diode performance is on the lower side. At 0 dBm or 1mW input power, and no external bias the diodes yielded a maximum of 2 μA with mega

ohms resistance. The efficiency (η) of a device can be defined as the ratio of output power to the input power. Hence the efficiency was determined to be 0.4%. Finally, to measure the reflection coefficient or the return loss of the MIM diodes, the S11 pattern of the diodes were measured. The on-chip calibration standards were initially calibrated, and then using the two-port configuration the return loss was measured. Figure 7.10 shows the return loss of different MIM diode measured from 75 GHz to 110 GHz.

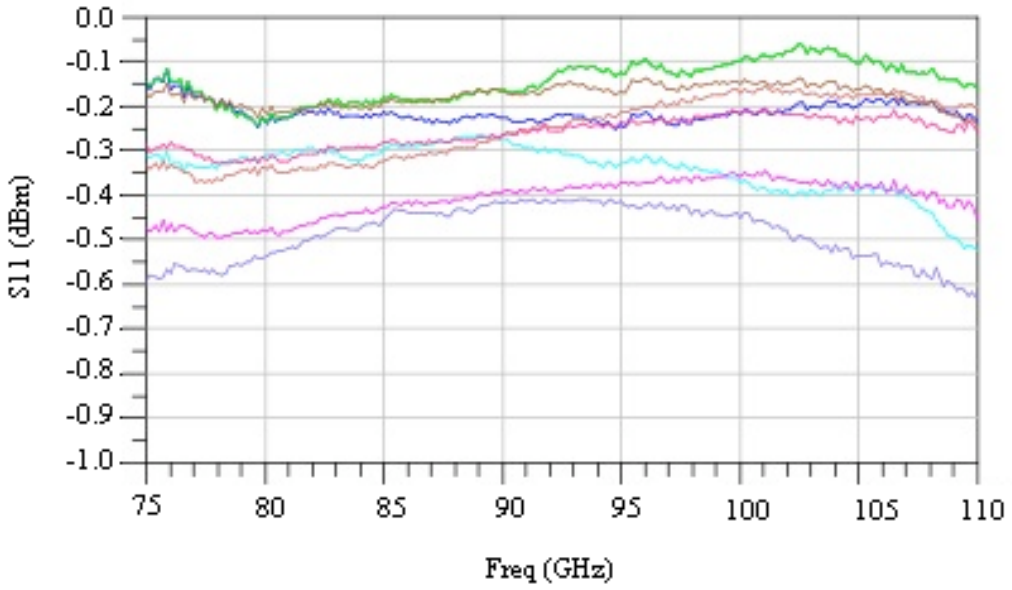

Figure 7.10: Return Loss of MIM Diode Measured from 75 to 110 GHz

From Figure 7.10, it is observed that all the diodes exhibited very high return loss. Typically, a perfectly matched device will have very low return loss approaching - ∞. This suggests that the diodes are rejecting most of the signal that is transmitted through the lead lines. This can be resolved by providing a matching network between the

transmission line and the diode or by developing the diode with much less resistance. But, in order to achieve maximum efficiency, a matching network would be preferred. Thus the experiment provides evidence of AC to DC conversion in spite of the issues.

In summary, the diodes when subjected to 94 GHz signal yielded about μA current output as exhibited from the I-V characteristics. However, when the diode was operated at a lower frequency, did not display any rectification like behavior. This might be because the diodes were designed for high frequency operation and hence the frequency mismatch causes the diode not to demonstrate rectification characteristics. In addition to mismatch, the diodes can be considered as a classic parallel plate capacitor with a thin dielectric layer. At high frequencies, a typical capacitor will behave as a short. Similarly, the diodes also displayed capacitor like behavior by exhibiting the characteristics of a short circuit as seen from the oscilloscope data.

CHAPTER 8

CONCLUSION AND FUTURE OUTLOOK

Thin Film MIM tunnel junctions with Ni-NiO-Cr with 1 μm^2 contact area were fabricated on bulk micromachined silicon substrate and its ability to convert mm-wave signal to DC output was investigated. These devices were developed using a one step e-beam lithography process to define the active area of the tunnel junction. The electrical behavior of the device was evaluated by testing its dc I-V and mm-wave characteristics. The diodes exhibited significant asymmetry and non-linearity with a maximum sensitivity of 7 V^{-1}.

MIM tunnel junctions were subjected to mm-wave measurement by directly feeding the signal to the diode through a VNA and the output current was measured using a high precision digital multimeter. The devices responded well to mm-wave signals yielding dc current output. When the diode was fed with a 94 GHz signal with 0 dBm (1 mW), a rectified output in the range of μA was observed. The output current was controlled by varying the bias and the input power of the mm-wave signal. Thus, thin film MIM tunnel junctions with dissimilar electrodes were developed on silicon membrane for the first time for mm-wave detection.

In addition, MIM junctions were also fabricated with larger device area (100 μm^2) using conventional photolithography on silicon substrates. The electrical response of

these diodes was investigated by measuring it dc I-V response at room temperature. Further, the effects of post-deposition annealing on the device stability were analyzed. The diodes demonstrated enhanced electrical characteristics up to 250°C, with a maximum sensitivity of $45V^{-1}$. These diodes exhibited the highest sensitivity ever reported by any research group.

As an alternate method of fabricating MIM junctions, the feasibility of using an organic layer as the dielectric was investigated. For this, a monolayer of polyaniline was used as the dielectric layer. The organic insulator layer was deposited using Langmuir-Blodgett technique and its electrical characteristics were evaluated by I-V measurement. The polyaniline based MIM junctions yielded a better asymmetry and non-linearity than the NiO based tunnel junctions. However, the current exhibited by the polyaniline tunnel junctions were lower than NiO tunnel junctions.

8.1 General Comments and Suggestions

The NiO based tunnel junctions exhibited non-linear and asymmetrical electrical characteristics. However, the current exhibited varied with every device. This can be attributed to the non-uniformity in the dielectric thickness. Although the thickness of the dielectric was experimentally determined to be 3 nm, even a slight variation in the thickness can contribute to deviation in current output.

The surface roughness of the film can also contribute to this discrepancy. From the fabrication process it is identified that the NiO layer is deposited at 30 mTorr. This is fairly high for a thin film deposition process and would increase the roughness of the film, causing a large non-uniformity. This non-uniformity will contribute to the variation

in diode output. Hence, to achieve uniform current output the dielectric deposition process has to be done at lower pressures.

Also, the diodes were fabricated as a step-by-step process, wherein a photolithography process was involved after each layer. This causes the thin films to be exposed to several chemicals, potentially causing the device to perform less effectively. Hence a multi-step deposition process has to be adopted to preserve the MIM stack especially the insulator layer.

The diode development has to be done by considering composite materials, alternate dielectric with smaller barrier height and width. Only by using smaller barrier height materials, can we achieve conduction at very small voltages. In that view, using organic layers as dielectric seems promising, but it has to be optimized to achieve an ultra-thin layer of the organic material.

The mm-wave measurements were carried out by directly connecting the 94 GHz source to the tunnel junction and the rectified current was measured using a multimeter. However, the tunnel junctions need to be coupled with an antenna to determine the radiation and coupling parameters. Thus as a next step towards enhancing the mm-wave detector, the MIM junctions have to be integrated with an antenna and evaluated.

REFERENCES

[1] D.A. Jennings, F.R. Petersen, and K. M. Evenson, "Extension of Absolute Frequency Measurements to 148 THz: Frequencies of 2.0- and 3.5 μm Xe Laser," *Applied Physics Letters,* vol. 26, pp. 510-511, 1975.

[2] C. W. Slayman and T. K. Gustafson, "Metal-Barrier-Metal Junctions for Room Temperature Millimeter-Wave Mixing and Detection," in *Microwave Symposium Digest, MTT-S International*, 1981, pp. 338-340.

[3] J. W. Dees, "Detection and harmonic generation in the sub-millimeter wavelength region," *Microwave Journal,* vol. 9, pp. 48-55, 1966.

[4] A.B. Hoofring, V.J. Kapoor, and W. Krawczonek, "Submicron Nickel-Oxide-Gold Tunnel Diode Detectors for Rectennas," *Journal of Applied Physics,* vol. 66, pp. 430-437, 1989.

[5] S. E. Borek, "An Overview of Through the Wall Surveillance for Homeland Security," in *Proceedings of the 34th Applied Imagery and Pattern Recognition Workshop*, 2005, pp. 42-47.

[6] L.R. Wicker and D. C. Webb, "The Potential Military Application of Millimeter Waves," in *Millimeter and Submillimeter Wave Propagation and Circuits*, 1978, pp. 1.1-1.6.

[7] C.R.Nave, "Hyperphysics: Electromagnetic Spectrum," 2006.

[8] J. D. Vincent, *Fundamentals of Infrared Detector Operation and Testing*. New York, NY John Wiley& Sons, 1989.

[9] P. Bhartia and I. J. Bahl, *Millimeter Wave Engineering and Applications*. New York, NY: John Wiley & Sons, 1984.

[10] NASA, "Infrared Waves," in *The Electromagnetic Spectrum*, 2007.

[11] Maureen Kaine- Krolak and M. E. Novak, "An Introduction to Infrared Technology: Application in the Home, Classroom, Workplace, and Beyond..", 1995.

[12] FLIR, "FLIR Thermal Imaging Infrared Camera," 2005.

[13] TSA, "Millimeter Wave: Whole Body Imaging," 2008.

[14] E.R.Brown, "Fundamentals of Terrestrial Millimeter-Wave and THz Remore Sensing," in *Terahertz Sensing Technology*. vol. 2, Dwight L. Woolard, William R. Loerop, and M. S. Shur, Eds.: World Scientific, 2003.

[15] I. M. Blankson, "Passive Millimeter Wave Imaging with Super-Resolution: Application to Aviation Safety in Extremely Poor Visibility," 2001.

[16] G. R. Huguenin, "Millimeter Wave Concealed Weapon Detection and Through-the-Wall Imaging Systems," in *", Proceedings of SPIE*, 1997, pp. 152-159.

[17] D.D. Ferris Jr. and N. C. Currie, "Overview of current technology in mmw radiometric sensors for law enforcement applications," in *Proceedings of SPIE*, 2000, pp. 61-71.

[18] M. Schlechtweg, A. Tessmann, A. Leuther, C. Schwörer, H. Massler, M. Mikulla, M. Walther, and R. Lösch, "Advanced millimeter-wave ICs using metamorphic HEMT technology," *Physica Status Solidi C,* vol. 3 pp. 465-468, 2006.

[19] R. Stevenson, "Chip innovators eye airport surveillance equipment," in *Compound Semiconductor*. vol. 13, 2007.

[20] S. E. Borek, "An Overview of New Surveillance Technologies," in *7th Annual Technologies For Critical Incident Preparedness Conference* San Diego, 2005.

[21] P. J. Costianes, "An Overview of Concealed Weapons Detection for Homeland Security," in *Proceedings of the 34th Applied Imagery and Pattern Recognition Workshop*, 2005, pp. 2-6.

[22] K.J. Linden, W. R. Neal, J. Waldman, A.J. Gatesman, and A. Danylov, "Terahertz Laser Based Standoff Imaging System," in *Proceedings of the 34th Applied Imagery and Pattern Recognition Workshop*, 2005, pp. 7-14.

[23] D. Novak, R. Waterhouse, and A. Farnham, "Millimeter-Wave Weapons Detection System," in *Proceedings of the 34th Applied Imagery and Pattern Recognition Workshop*, 2005, pp. 15-20.

[24] A. Achanta, M.Mckenna, J. Heyman, K. Rudd, M. Hinders, and P. Costianes, "Non-linear Acoustic Concealed Weapons Detection," in *Proceedings of the 34th Applied Imagery and Pattern Recognition Workshop*, 2005, pp. 21-27.

[25] C. Fumeaux, W. Herrmann, F.K. Kneubühl, and H. Rothuizen, "Nanometer Thin Film Ni-NiO-Ni Diodes for Detection and Mixing of 30 THz Radiation," *Infrared Physics and Technology,* vol. 39, pp. 123-183, 1998.

[26] M.R. Abdel-Rahman, F.J. Gonzalez, and G. D. Boreman, "Antenna-Coupled Metal-Oxide-Metal Diodes for Dual-Band Detection at 92.5 GHz and 28 THz," *Electronics Letter,* vol. 40, 2004.

[27] J. Piotrovski and A. Rogalski, "Uncooled Long Wavelength Infrared Photon Detectors," *Infrared Physics and Technology,* vol. 46, 2004.

[28] C.C. Fumeaux, D.F Spenser, and G. D. Boreman, "Microstrip Antenna-Coupled Infrared Detector," *Electronics Letter,* vol. 35, pp. 2166-2167, 1999.

[29] B. Berland, "Photovoltaic Technologies Beyond the Horizon: Optical Rectenna Solar Cell," 2003.

[30] G. P. Gauthier, J. P. Raskin, and G. M. Rebeiz, "A 140-170-GHz low-noise uniplanar subharmonic Schottky receiver," *Microwave Theory and Techniques, IEEE Transactions on,* vol. 48, pp. 1416-1419, 2000.

[31] Wikepedia, "Wilhelmy plate - Wikipedia, The Free Encyclopedia," 2008.

[32] I. Codreanu and G. D. Boreman, "Influence of Dielectric Substrate on the Responsivity of Microstrip Dipole-Antenna-Coupled Infrared Microbolometers," *Appl. Opt.,* vol. 41, pp. 1835-1840, 2002.

[33] E. N. Grossman, J. E. Sauvageau, and D. G. McDonald, "Lithographic spiral antennas at short wavelengths," *Applied Physics Letters,* vol. 59, pp. 3225-3227, 1991.

[34] F. J. Gonzalez, M. Abdel-Rahman, and G. D. Boreman, "Antenna-coupled VOx thin-film microbolometer array," *Microwave and Optical Technology Letters,* vol. 38, pp. 235-237, 2003.

[35] O. Acef, L. Hilico, M. Bahoura, F. Nez, and P. D. Natale, "Comparison between MIM and Schottky diodes as harmonic mixers for visible and microwave sources," *Optics Communications,* vol. 109, pp. 428-434, 1994.

[36] G. M. Elchinger, A. Sanchez, J. C. F. Davis, and A. Javan, "Mechanism of detection of radiation in a high-speed metal-metal oxide-metal junction in the visible region and at longer wavelengths," *Journal of Applied Physics,* vol. 47, pp. 591-594, 1976.

[37] E. Wiesendanger and F. Kneubühl, "Thin-film MOM-diodes for infrared detection," *Applied Physics A: Materials Science & Processing,* vol. 13, pp. 343-349, 1977.

[38] D. Diesing, A. W. Hassel, and M. M. Lohrengel, "Aluminium oxide tunnel junctions: influence of preparation technique, sample geometry and oxide thickness," *Thin Solid Films,* vol. 342, pp. 282-290, 1999.

[39] M. Heiblum, W. Shihyuan, J. Whinnery, and T. Gustafson, "Characteristics of integrated MOM junctions at dc and at optical frequencies," *Quantum Electronics, IEEE Journal of,* vol. 14, pp. 159-169, 1978.

[40] I. Wilke, Y. Oppliger, W. Herrmann, and F. K. Kneubühl, "Nanometer Thin Film Ni-NiO-Ni Diodes for 30 THz Radiation," *Applied Physics A: Solids and Surfaces,* vol. 58, pp. 329-341, 1994.

[41] P. Esfandiari, G. Bernstein, P. Fay, W. Porod, B. Rakos, A. Zarandy, B. Berland, L. Boloni, G. Boreman, B. Lail, B. Monacelli, and A. Week, "Tunable antenna-coupled metal-oxide-metal (MOM) uncooled IR detector," in *Proceedings of SPIE*, 2005, pp. 470-482.

[42] J.-G. Zhu and C. Park, "Magnetic tunnel junctions," *Materials Today,* vol. 9, pp. 36-45, 2006.

[43] J. G. Simmons, "Electric Tunnel Effect between Dissimilar Electrodes Separated by a Thin Insulating Film," *Journal of Applied Physics,* vol. 34, pp. 2581-2590, 1963.

[44] A. Gehring, "Simulation of Tunneling in Semiconductor Devices." vol. PhD Dissertation, 2003.

[45] S. M. Sze, *Physics of Semiconductor Devices*, 2nd Edition ed. New York, NY: Wiley Inter-Science Publication, 1981.

[46] A. Sanchez, J. C. F. Davis, K. C. Liu, and A. Javan, "The MOM tunneling diode: Theoretical estimate of its performance at microwave and infrared frequencies," *Journal of Applied Physics,* vol. 49, pp. 5270-5277, 1978.

[47] D. R. Lide, "CRC Handbook of Chemisty and Physics," 74 ed: CRC Press, 1993-1994.

[48] G. Tech., "Photolithography."

[49] "JEOL JSM 840 Training Manual."

[50] J. C. Nabity, "Nanopattern Generation System software."

[51] B.N.Chapman, *Glow Discharge Processes: Sputtering and Plasma Etching*. New York, NY: Wiley Inter-Science Publication, 1980.

[52] K. I. USA, "Langmuir and Langmuir-Blodgett Films: What and How?."

[53] S. Maleki and P. Kosky, "Frontiers of Nanotechnology," 2005.

[54] S. Krishnan, "Design, Fabrication and Characterization of Thin Film MIM diodes for Rectenna Array," in *Electrical Engineering*. vol. Masters Tampa: University of South Florida, 2004.

[55] H. LaRosa, "Investigation of the Rectenna Concept for Millimeter Wave Detection," in *Electrical Engineering*. vol. Masters: University of South Florida, 2007.

[56] R. J. Powell and W. E. Spicer, "Optical Properties of NiO and CoO," *Physical Review B,* vol. 2, p. 2182, 1970.

[57] Nima, "611D Conventional LB Trough."

[58] K. V. Rao and A. Smakula, "Dielectric Properties of Cobalt Oxide, Nickel Oxide, and Their Mixed Crystals," *Journal of Applied Physics,* vol. 36, pp. 2031-2038, 1965.

[59] P.C. Hobbs, R. B. Laibowitz, and F. R. Libsch, "Ni-NiO-Ni tunnel junctions for terahertz and infrared detection.," *Applied Optics,* vol. 44, pp. 6813-6822, 2005.

[60] V. Da Costa, M. Romeo, and F. Bardou, "Statistical properties of currents flowing through tunnel junctions," *Journal of Magnetism and Magnetic Materials,* vol. 258-259, pp. 90-95, 2003.

[61] V. Da Costa, C. Tiusan, T. Dimopoulos, and K. Ounadjela, "Tunneling Phenomena as a Probe to Investigate Atomic Scale Fluctuations in Metal/Oxide/Metal Magnetic Tunnel Junctions," *Physical Review Letters,* vol. 85, p. 876, 2000.

[62] S. Krishnan, H. La Rosa, E. Stefanakos, S. Bhansali, and K. Buckle, "Design and development of batch fabricatable metal-insulator-metal diode and microstrip slot antenna as rectenna elements," *Sensors and Actuators A: Physical,* vol. 142, pp. 40-47, 2008.

[63] S. W. Jeong, H. J. Lee, K. S. Kim, M. T. You, Y. Roh, T. Noguchi, W. Xianyu, and J. Jung, "Effects of annealing temperature on the characteristics of ALD-deposited HfO2 in MIM capacitors," *Thin Solid Films,* vol. 515, pp. 526-530, 2006.

[64] M. J. Lee and K. S. Chung, "Effects of Post-annealing on Current-Voltage Characteristics of Metal-Insulator (Ta2O5)-Metal Type Thin-Film Diodes," *Journal of Korean Physical Society,* vol. 39, pp. 686-691, 2001.

[65] H.-L. Chen, Y.-M. Lu, and W.-S. Hwang, "Characterization of sputtered NiO thin films," *Surface and Coatings Technology,* vol. 198, pp. 138-142, 2005.

[66] M. R. Abdel-Rahman, B. Monacelli, A. R. Weeks, G. Zummo, and G. D. Boreman, "Design, fabrication, and characterization of antenna-coupled metal-oxide-metal diodes for dual-band detection," *Optical Engineering,* vol. 44, pp. 066401-7, 2005.

APPENDICES

Appendix A: Process Flow for Fabrication of 100 μm^2 MIM diode

Step 1: Substrate Cleaning

RCA Clean 1: To remove organic contaminants

Immerse the substrate in 1:1:5 solution of $NH_4OH + H_2O_2+H_2O$ at 75°C for 15 minutes

Oxide removal: Short Immersion of 1:10 $HF+H_20$ to remove the native silicon dioxide formed on the surface of the substrate

RCA clean 2: To remove Ionic contaminants

Immerse the substrates in 1:1:5 solution of $HCl+H_20_2+H_20$ at 75°C for 15 minutes.

Rinse it with water and N_2 dry.

Step2: Thermal Oxidation

Load sample in oxidation tube furnace. Heat it up to 1100°C. Determine the oxidation time for achieving 1 μm thick oxide and grow oxide.

Step 3: Photolithography

Layer 1- Bottom Electrode

Spin coat – Futurrex 3000 PY negative resist; spin speed – 3000 RPM; time – 40 seconds

Soft bake – Hot plate; T=155^oC for 60 seconds

Expose – Quintel Mask aligner; 17 seconds exposure to UV

Appendix A (Continued)

Hard bake – Hot plate; T=110^{o}C for 60 sec

Develop – RD 6 developer; Immersion developing at room temperature for 25 seconds

Rinse in DI water and N_2 dry

Pattern check*:* Optical Microscope

Step 4: Metal Deposition

Sputtering - Ni

Base pressure- 3 μTorr Power- 100 W; Working pressure – 15 mTorr,

Reactive Sputtering – NiO

Power – 25 W; working pressure – 30 mTorr; Deposition time – 15 minutes.

Step 5: Lift-Off and Ultrasonic clean

Immerse the substrate in Acetone till all the unwanted metals peels off from the substrate. Lift-off aided with ultrasonic bath

Check thickness using the Profilometer

Step 6: Photolithography

Layer 2- Top Electrode

Spin coat – Futurrex 3000 PY negative resist; spin speed – 3000 RPM; time – 40 seconds

Appendix A (Continued)

Soft bake – Hot plate; T=155^{o}C for 60 seconds

Expose – Quintel Mask aligner; 17 sec exposure to UV

Hard bake – Hot plate; T=110^{o}C for 60 seconds

Develop – RD 6 developer; Immersion developing at room temp for 25 seconds

Rinse in DI water and N_2 dry

Pattern check*:* Optical Microscope

Step 7: Metal Deposition

Thermal Evaporation - Cr and Au

Pressure – 4 μTorr, Current- 80 and 200 A for Cr and Au, respectively; Deposition rate - 1Å/sec for Cr and 3Å/sec for Au.

Step 8: Lift-Off and Ultrasonic clean

Immerse the substrate in Acetone till all the unwanted metals peels off from the substrate. Lift-off aided with ultrasonic bath

Check thickness using the Profilometer

Appendix B: Process Flow for Fabrication of 1 μm^2 MIM diode

Step 1: Substrate Cleaning

RCA Clean 1: To remove organic contaminants

Immerse the substrate in 1:1:5 solution of $NH_4OH + H_2O_2+H_2O$ at 75°C for 15 minutes

Oxide removal: Short Immersion of 1:10 $HF+H_20$ to remove the native silicon dioxide formed on the surface of the substrate.

RCA clean 2: To remove Ionic contaminants

Immerse the substrates in 1:1:5 solution of $HCl+H_20_2+H20$ at 75°C for 15 minutes.

Rinse it with water and N_2 dry.

Step2: Thermal Oxidation

Load sample in oxidation tube furnace. Heat it up to 1100°C. Determine the oxidation time for achieving 1 μm thick oxide and grow oxide.

Step 3: Photolithography

Layer 1- contact pads, calibration standards and Antenna design:

Spin coat – Futurrex 3000 PY negative resist; spin speed – 3000 RPM; time – 40 seconds

Soft bake – Hot plate; T=155^oC for 60 seconds

Expose – EVG 620; 17 seconds exposure to UV

Appendix B (Continued)

Hard bake – Hot plate; T=110^{o}C for 60 seconds

Develop – RD 6 developer; Immersion developing @room temp for 25 seconds

Rinse in DI water and N_2 dry

Pattern check*:* Optical Microscope

Step 4: Metal Deposition

Thermal Evaporation - Cr and Au

Pressure – 4 μTorr, Current- 80 and 200 A for Cr and Au, respectively; Deposition rate - 1Å/sec for Cr and 3Å/sec for Au.

Step 5: Lift-Off and Ultrasonic clean

Immerse the substrate in Acetone till all the unwanted metals peels off from the substrate. Lift-off aided with ultrasonic bath

Check thickness using the Profilometer

Step 6: Photolithography

Layer 2- Bottom electrode

Spin coat – Futurrex 3000 PY negative resist; spin speed – 3000 RPM; time – 40 seconds

Soft bake – Hot plate; T=155^{o}C for 60 seconds

Appendix B (Continued)

Expose – EVG 620; 17 seconds exposure to UV

Hard bake – Hot plate; T=110^{o}C for 60 seconds

Develop – RD 6 developer; Immersion developing @room temp for 25 seconds

Rinse in DI water and N_2 dry

Pattern check*:* Optical Microscope

Step 7: Metal Deposition

Sputtering - Ni

Base pressure- 3 μTorr Power- 100 W; Working pressure – 15 mTorr,

Reactive Sputtering – NiO

Power – 25 W; working pressure – 30 mTorr; Deposition time – 15 minutes.

Step 8: Lift-Off

Immerse the substrate in Acetone till all the unwanted metals peels off from the substrate. Lift-off aided with ultrasonic bath

Check thickness using the Profilometer

Step 9: E-beam lithography

Layer 3- Top electrode

Appendix B (Continued)

Spin coat – Microchem ® PMMA A3 positive resist; spin speed – 3500 RPM; time – 25 seconds

Soft bake – Hot plate; T=180^{o}C for 120 seconds

Working Distance- 15 mm; Accelerating Voltage 30kV; Probe current – 60 pA

Expose – Using JEOL JSM840 SEM exposure to e-beam, controlled by NPGS

Develop – 3:1 IPA: MIBK developer; Immersion developing @room temp for 70 seconds,

Rinse in IPA and DI water and N_2 dry

Pattern check*:* Optical Microscope

Step 10: Metal Deposition

Thermal Evaporation - Cr and Au

Pressure – 4 μTorr, Current- 80 and 200 A for Cr and Au, respectively;

Deposition rate - 1Å/sec for Cr and 3Å/sec for Au.

Step 11: Lift-Off and Ultrasonic clean

Immerse the substrate in Acetone till all the unwanted metals peels off from the substrate. Lift-off aided with ultrasonic bath

Check thickness using the Profilometer

Step 12: Photolithography

Layer 4- Silicon membrane

Spin coat – back side of the wafer Shipley S1813 positive resist; spin speed – 2500 RPM; time – 25seconds

Soft bake – Hot plate; T=90^{o}C for 60 second

Expose – EVG 620; back side alignment and 9 second exposure to UV

Develop – MF319 developer; Immersion developing @room temp for 45 seconds

Hard bake – Hot plate; T=110^{o}C for 60 seconds

Rinse in DI water and N_2 dry

Pattern check*:* Optical Microscope

Step 13: Front side protection from HF

Spin coat – Futurrex 3000 PY negative resist; spin speed – 3000 RPM; time – 40seconds

Hard bake – Hot plate; T=110^{o}C for 60 seconds

Rinse in DI water and N_2 dry

Step 14: Etch Oxide layers from the silicon window

Immerse the substrate in 10:1 HF: H_20 for 15 minutes to etch the oxides.

Check for complete oxide removal

Step 15: Resist Removal

Immerse the substrate in acetone to remove the photoresists from both sides

Step 16: Si Etch protection layer – Front side

Spin Coat – Brewer Science ProTek Primer; Spin speed 1500 RPM; Time- 60 seconds

Bake – Hotplate, Temp - 120^{o}C for 60 seconds

Spin coat - Brewer Science ProTek B2-18; Spin speed – 2000 RPM; spin time -90 seconds

First hard bake – Hotplate Temp 120^{o}C for 2 minutes

Second hard bake – Hotplate Temp 155^{o}C for 2 minutes

Third hard bake – 205^{o}C for 1 minute

Appendix C: Current-Voltage Characteristics of MIM Junctions

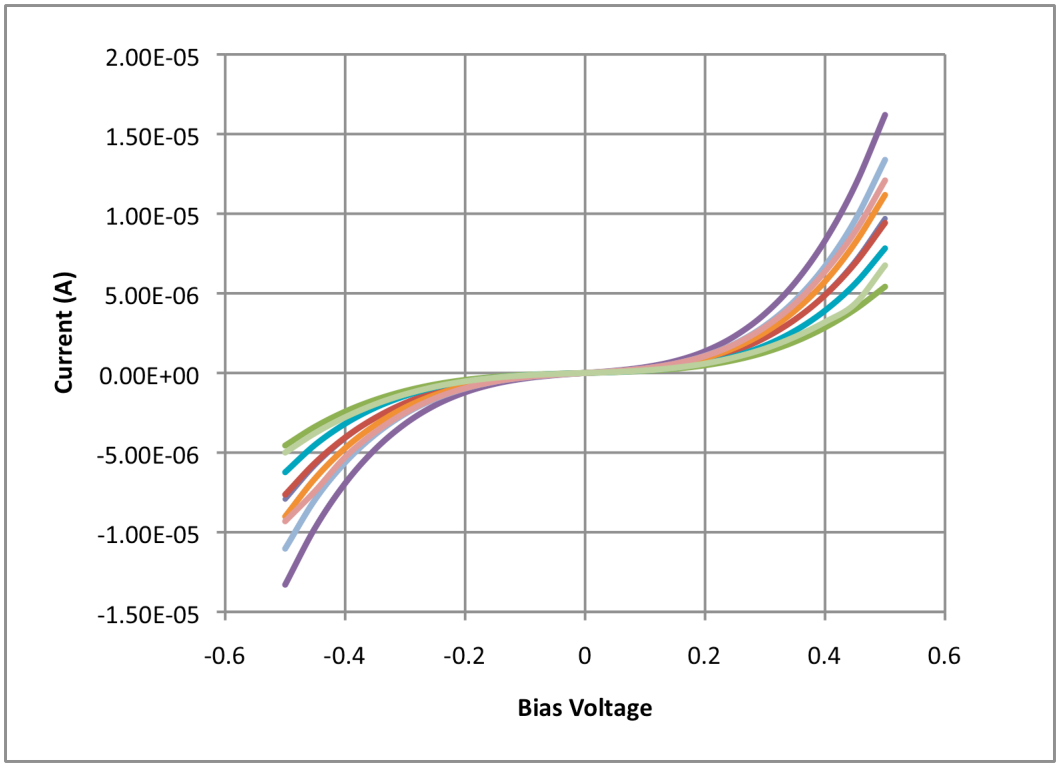

Figure C.1: I-V Characteristics of Ni-NiO-Cr MIM Junctions with 100 µm^2 Contact Area

Appendix C (Continued)

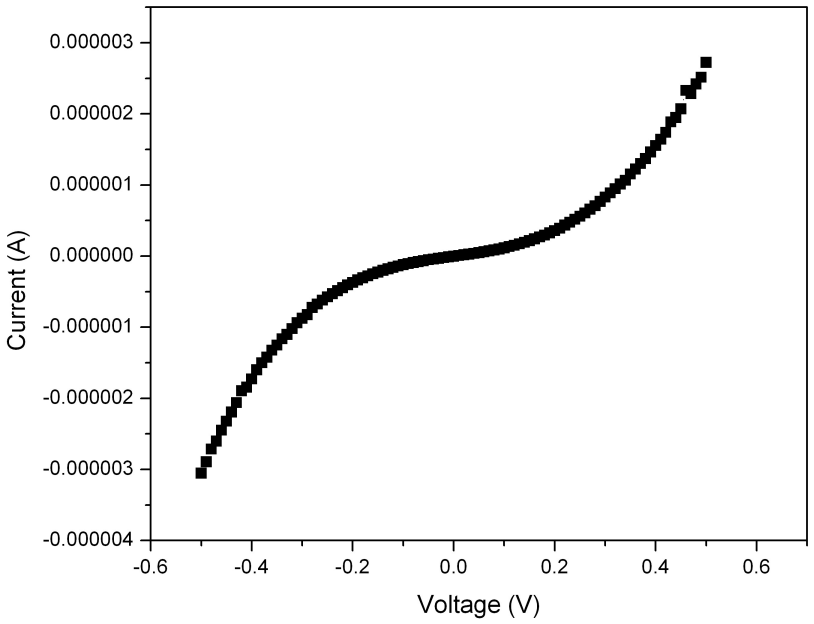

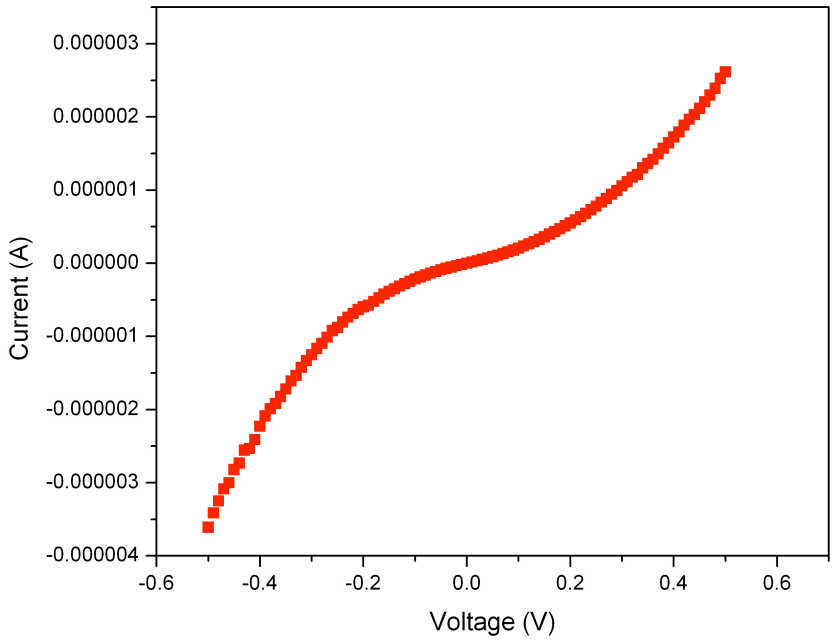

Appendix C (Continued)

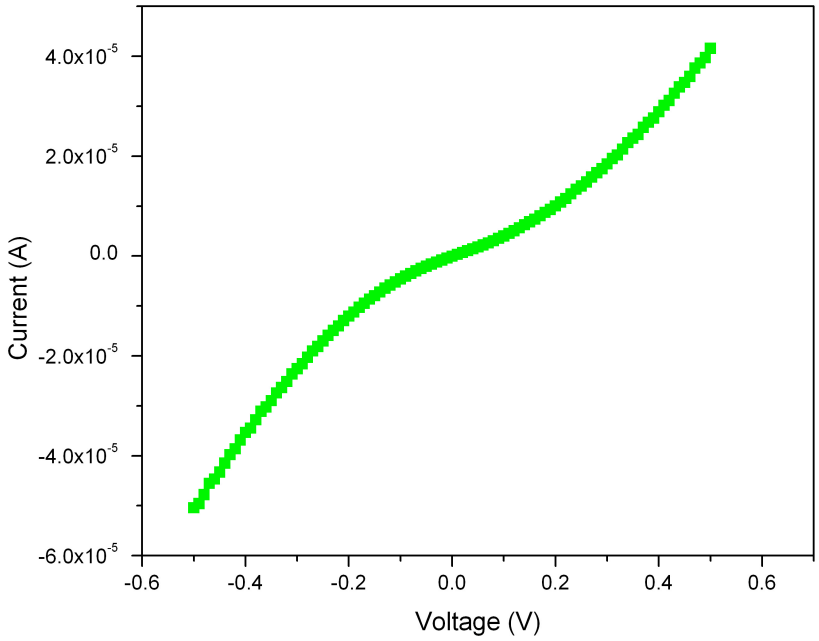

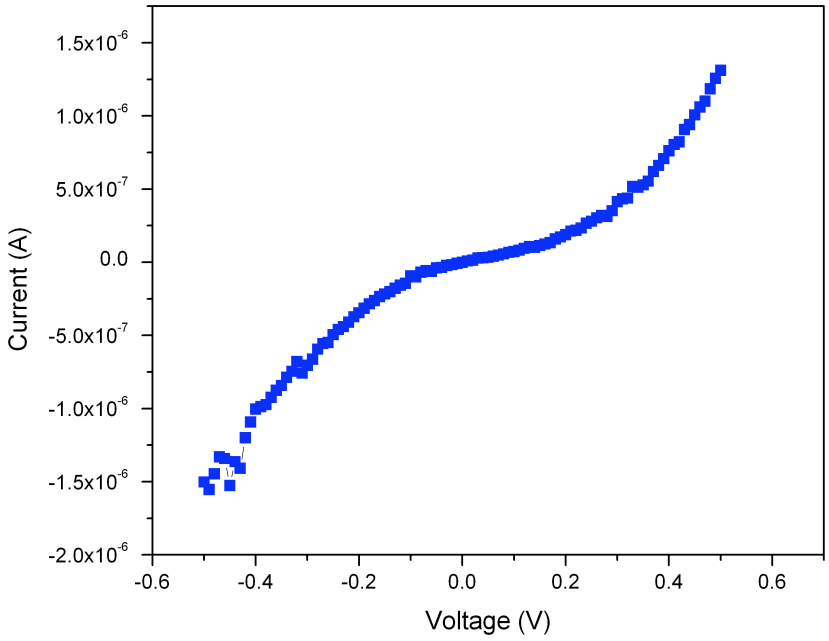

Appendix C (Continued)

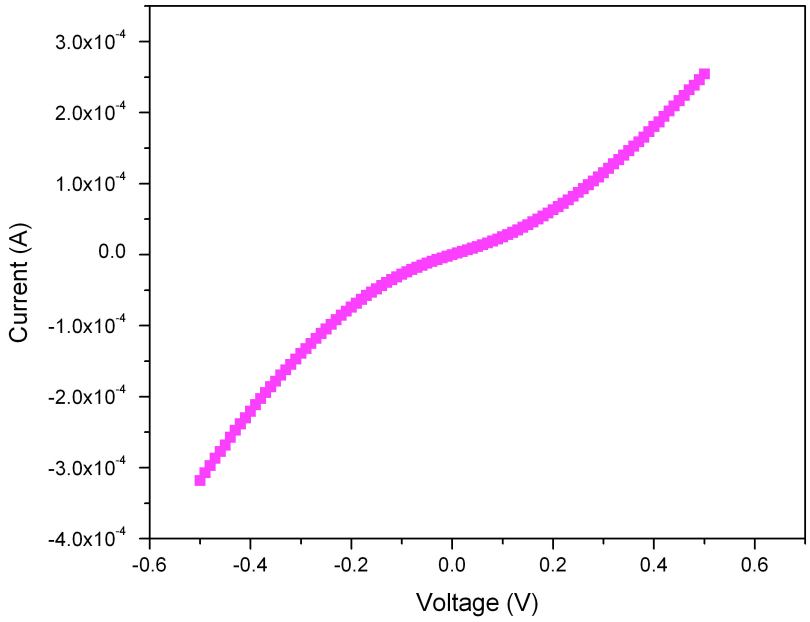

Figure C.2: I-V Characteristics of Ni-NiO-Cr MIM Junctions with 1 µm^2 Contact Area

Appendix C (Continued)

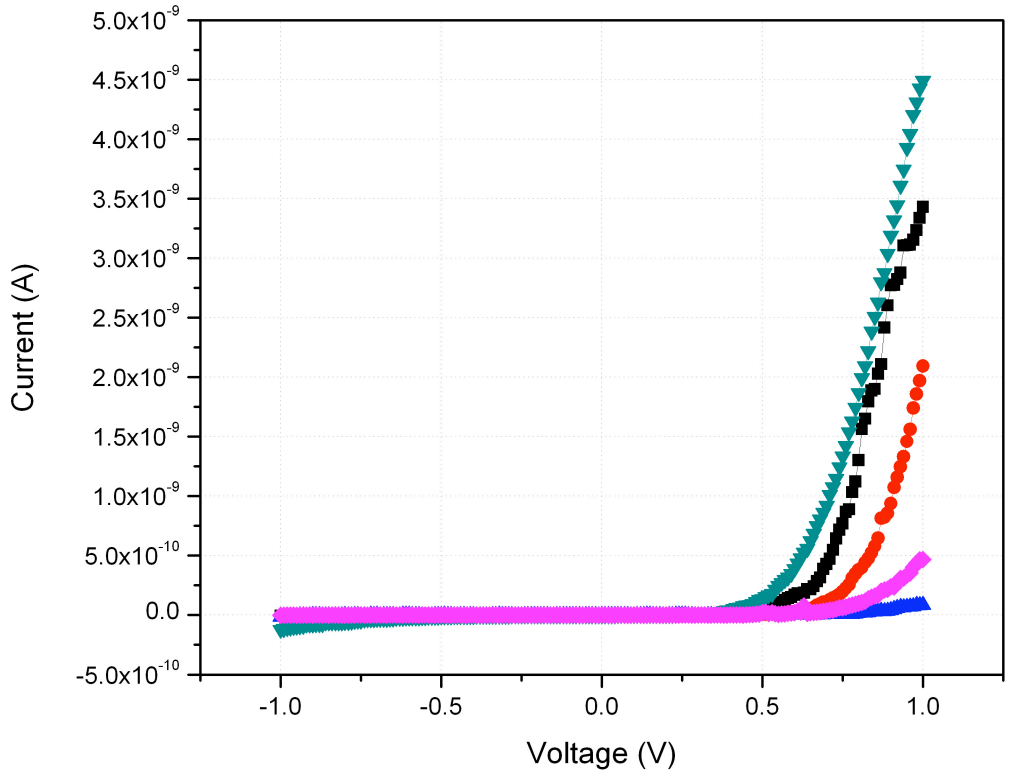

Figure C.3: I-V Characteristics of Ni-PANI-Cr MIM Junctions with 100 µm^2 Contact Area

ABOUT THE AUTHOR

The author received his Bachelors degree in Electronics and Communications Engineering from the University of Madras, India in 2000. Following this, he received his Masters degree in Electrical Engineering with specialization in Microelectronics from the University of South Florida, Tampa in 2004. He worked with Dr. Elias Stefanakos and Dr. Shekhar Bhansali at the Clean Energy Research Center to study the feasibility of developing thin film diodes for alternate energy conversion for his Masters thesis. He continued with the same group for a PhD degree in Electrical Engineering. In his doctoral work, he was involved in the development of thin film tunnel junctions for thermal detection at millimeter wave range. His research focus is in development of next generation energy conversion device based on thin films. His research interests are in the areas of micro/nanofabrication, materials science and thin film sensors.